

Titre: Multiscale Numerical Simulation of Biaxial Braids with Discrete
Fibers for Manufacturing Thermoplastic Composite Rods Using
Braid-trusion
Title:

Auteur: Mohammad Ghaedsharaf
Author:

Date: 2021

Type: Mémoire ou thèse / Dissertation or Thesis

Référence: Ghaedsharaf, M. (2021). Multiscale Numerical Simulation of Biaxial Braids with
Discrete Fibers for Manufacturing Thermoplastic Composite Rods Using Braid-
trusion [Thèse de doctorat, Polytechnique Montréal]. PolyPublie.
Citation: <https://publications.polymtl.ca/9187/>

 **Document en libre accès dans PolyPublie**
Open Access document in PolyPublie

URL de PolyPublie: <https://publications.polymtl.ca/9187/>
PolyPublie URL:

Directeurs de recherche: Louis Laberge Lebel, & Jean-Évrard Brunel
Advisors:

Programme: Génie mécanique
Program:

POLYTECHNIQUE MONTRÉAL

affiliée à l'Université de Montréal

**Multiscale numerical simulation of biaxial braids with discrete fibers for
manufacturing thermoplastic composite rods using braid-trusion**

MOHAMMAD GHAEDSHARAF

Département de génie mécanique

Thèse présentée en vue de l'obtention du diplôme de *Philosophiæ Doctor*

Génie mécanique

Août 2021

POLYTECHNIQUE MONTRÉAL

affiliée à l'Université de Montréal

Cette thèse intitulée:

Multiscale numerical simulation of biaxial braids with discrete fibers for manufacturing thermoplastic composite rods using braid-trusion

présentée par **Mohammad GHAEDSHARAF**

en vue de l'obtention du diplôme de *Philosophiæ Doctor*

a été dûment acceptée par le jury d'examen constitué de :

Eduardo-Antonio-Julian RUIZ, président

Louis LABERGE LEBEL, membre et directeur de recherche

Jean-Evrard BRUNEL, membre et codirecteur de recherche

Frederick GOSSELIN, membre

François ROBITAILLE, membre externe

DEDICATION

To my beloved family

ACKNOWLEDGEMENTS

I wholeheartedly appreciate my supervisor, Professor Louis Laberge Lebel, for his excellent guidance and vast knowledge shared through weekly meetings and discussions during my thesis course. His continuous support and encouragement made it possible to achieve my goals. He also gave me the opportunity to broaden my expertise not only in the fields of my research but also in other areas such as project management, which will have a great impact on my life.

I would like to thank my co-director, Dr. Jean-Evrard Brunel, from Bombardier aviation for his advice and collaboration, whose boundless knowledge was a great support in conducting this thesis. Here I have to thank other project team members from Bombardier aviation, Mr. Hasan Salek and Mr. Mario Simard, who shared their knowledge to progress this work.

In addition, I really appreciate Professor Eduardo-Antonio-Julian Ruiz, Professor Frederick Gosselin, Professor François Robitaille, and Professor Jason Robert Tavares for accepting to serve on my thesis committee.

Moreover, I would like to express my gratitude to members of the Shape Memory Alloys and Intelligent Systems Laboratory (LAMSI) at the École de Technologie Supérieure (ÉTS), and Mrs. Marie-Hélène Bernier from Polytechnique Montreal for CT scans.

I also would like to extend my gratitude to all my friends and colleague in ACFSlab for their limitless help.

Furthermore, I acknowledge the Bombardier Aviation, the Natural Science and Engineering Research Council of Canada (NSERC), the Advanced Materials Research and Innovation Hub PRIMA Québec, and the Pultrusion Technique Inc. for their support.

RÉSUMÉ

Peu de techniques entièrement automatisées sont disponibles pour fabriquer des polymères renforcés de fibres. L'une de ces techniques est la *braid-trusion* thermoplastique, qui combine deux techniques hautement automatisées : le tressage et la pultrusion. Dans le procédé de *braid-trusion* thermoplastique, un mélange tressé de fibres thermoplastiques et de renfort est tiré dans un moule chauffé pour faire fondre les fibres thermoplastiques. Ce mélange est par la suite solidifié par un moule de refroidissement. Le procédé de *braid-trusion* thermoplastique est encore en cours de développement et n'est pas largement employé sur le marché. Un obstacle majeur est le manque de simulation permettant de prédire la déformation de la tresse pendant le procédé ainsi que de prédire l'architecture finale du textile. La simulation du procédé *braid-trusion* est une tâche difficile en raison du processus de formation complexe, de l'architecture complexe de la tresse, de la nature discrète inhérente à plusieurs échelles des fils et des interactions de friction entre les fibres. Ici, nous introduisons une méthodologie de simulation numérique pour le processus de *braid-trusion* thermoplastique en utilisant un modèle multiéchelle par éléments finis validé expérimentalement. Trois objectifs sont définis pour mener à bien cette recherche.

Le premier objectif est de développer une méthodologie de conception simple basée sur la géométrie des tresses biaxiales pour fabriquer une tige thermoplastique tressée en utilisant une ligne de pultrusion à plusieurs moules chauffants. Pour concevoir le procédé, trois paramètres du taux de sur remplissage (taux de reflux excessif de la résine), l'angle nominal de la tresse et la fraction volumique des fibres sont calculés à chaque sortie de moule. Le diamètre de la tresse et la longueur du pas à l'intérieur des moules sont estimés grâce à une relation géométrique de tresse simplifiée. La conception proposée est utilisée avec succès pour fabriquer une tige tressée biaxiale en utilisant des fibres de carbone mélangées à du PEI. La caractérisation microscopique des sections transversales de la tige montre un lit de fibres tressées entièrement imprégné, une zone sans vide et une bonne répartition des fibres. Pour explorer les impacts de la tension de la bobine de fibres, trois expériences avec différente tension de bobine, soit une faible (2.5 N), une modérément élevée (40 N) et une élevée (80 N) sont examinées. La vitesse de procédé est évaluée en réalisant deux expériences avec des vitesses de traitement modérément faibles (50 mm/min) et modérément élevées (150 mm/min). La température du moule de refroidissement est également scrutée en faisant varier trois températures : T_g (température de transition vitreuse du PEI), $T_g/2$ et

$T_g/4$. Une imprégnation parfaite, une teneur sans vide et un excellent fini de surface sont obtenues avec une tension de bobine de 2.5 N, une vitesse de procédé de 50 mm/min et des températures de refroidissement de $T_g/2$ et $T_g/4$.

Le modèle proposé dans le premier objectif est incapable de prédire la géométrie interne et la morphologie mésoscopique des tresses. De plus, des simplifications et des incertitudes ont été introduites, car les interactions mécaniques fibre-fibre ont été négligées. Pour résoudre ces problèmes, nous introduisons un modèle, au niveau de la fibre, pour les tresses biaxiales. Ce modèle constitue le deuxième objectif de cette recherche. Cet objectif propose une méthodologie de modélisation permettant de prédire la géométrie 3D et la morphologie mésoscopique interne des tresses biaxiales. Les fils tressés sont modélisés comme un faisceau de fibres virtuelles à l'aide de chaînes d'éléments *truss*. Les simulations de deux modèles de tresse communs : diamant (1/1) et régulier (2/2), sont validées par une comparaison quantitative grâce à des numérisations de tomodensitométrie (CT) à rayons X. Nous constatons que la friction au niveau de la fibre explique l'état coincé des tresses, dans lequel l'énergie de dissipation de friction augmente rapidement une fois que la tresse a un allongement, un diamètre et un angle de tresse stable. Des études paramétriques illustrent la façon dont la diminution du coefficient de frottement impacte la forme de la section transversale du fil, alors qu'elle a un effet non significatif sur l'état de coincement. Les modèles révèlent également que la modification d'une large plage du module d'élasticité des fibres n'a guère d'impact sur la configuration de la géométrie mésoscopique des tresses.

Le troisième objectif consiste à utiliser le modèle présenté au deuxième objectif pour simuler le processus de formation de tresse thermoplastique. Une nouvelle méthodologie de modélisation est développée. Elle commence par la simulation d'une tresse biaxiale au niveau de la fibre sèche, constituée de fils mélangés, avant de modéliser le processus de *braid-trusion*. Une tige en composite thermoplastique est pultrudée avec succès selon la simulation. La pultrusion modifie l'architecture de la tresse de façon significative. Cette modification est prédite avec précision par le modèle grâce à des mesures macroscopiques de l'allongement du pas (7.6 %), de la réduction du diamètre (44.0 %) et de la réorientation de l'angle nominal (45.0 %.) La pultrusion compacte également les fils tressés ensemble, résultant en une fraction volumique de fibres locales de plus de 60%. La fraction volumique est quantifiée à l'aide de tomodensitométries à rayons X. La fraction volumique locale et la géométrie interne de la tige tressée sont prédites par le modèle. Le modèle

prédit également l'orientation locale des fibres. L'analyse au niveau de la fibre (microéchelle) démontre trois distributions de l'orientation locale de la fibre soit, dans le plan, hors du plan et l'angle par rapport à l'axe longitudinal de la tresse. Notamment, les distributions de l'orientation locale des fibres varient le long du rayon de la tresse. Les fibres sont orientées dans une certaine plage de rayon d'environ 30 à 70 % et 60 à 100 % du rayon extérieur avant et après la pultrusion, respectivement. À l'inverse, les distributions d'orientation des fibres sont uniformes le long de l'axe longitudinal de la tresse. L'étude paramétrique démontre que l'augmentation du coefficient de frottement entre les fibres et la paroi du moule allant de 0.1 à 0.6 a un effet non significatif sur l'orientation locale des fibres. L'énergie de friction dissipée reste presque constante pour les coefficients de friction faible (0.1) et moyen (0.4) entre les fibres et la paroi du moule, alors qu'elle augmente linéairement pour le procédé avec un coefficient de friction élevé (0.6).

Cette étude ouvre la porte de future conception basée sur la simulation de procédés complexes. Plus précisément, la méthode numérique proposée peut servir de plate-forme pour accélérer la conception et la fabrication de composites dans de nombreux domaines tels que le procédé de tressage sur mandrins aux formes complexes et le procédé de moulage par compression thermoplastique utilisant des moules complexes. De plus, l'outil numérique proposé peut réduire l'utilisation de méthodes expérimentales nécessitant des outils dispendieux, tels que la tomodensitométrie, pour étudier la géométrie, la morphologie mésoscopique et l'orientation locale des fibres des matériaux composites.

ABSTRACT

Few fully automated and continuous techniques are available to manufacture fiber-reinforced polymers. One of these techniques is thermoplastic braid-trusion, combining two high-automated techniques of braiding and pultrusion. In the thermoplastic braid-trusion forming process, a mixture of thermoplastic and reinforcement fibers is pulled into a heated die directly after braiding to melt the thermoplastic fibers and is consecutively solidified in a cooling die. The thermoplastic braid-trusion process is still under development and has not yet become a mass production process in the market. A major hurdle in the path toward that goal is that there is no simulation process readily available to understand the complex deformation of the braid during the braid-trusion process as well as to predict final textile architecture. Simulation of the braid-trusion process is a challenging task due to the complex forming process, intricate braid architecture, multiscale inherent, discrete nature of yarns and fibers, and complicated frictional interactions between discrete fibers. Here, we introduce a numerical simulation methodology for the thermoplastic braid-trusion process using a multiscale finite element model with experimental validations. Three objectives are outlined to accomplish this research.

The first objective is to propose a simple geometry-based design methodology for biaxial braids to manufacture a thermoplastic braid-truded rod using a multi-die pultrusion line. To design the process, three parameters of the overfilling ratio (the excessive resin backflow ratio), nominal braid angle, and fiber volume fraction are calculated at each die exit. The braid diameter and pitch length inside the dies are estimated through a simplified geometry relation of the braid. The proposed design is successfully used to manufacture a biaxial braid-truded rod using commingled carbon and PEI fibers. The microscopic characterization of the rod's cross-sections shows a fully impregnated braided fibers bed, void-free area, and proper fiber distribution. To explore the spool tension impacts, three experiments with low (2.5 N), moderately high (40 N), and high (80 N) spool tension are examined. The processing speed is evaluated by carrying out two experiments with moderately low (50 mm/min) and moderately high (150 mm/min) processing speeds. The cooling die temperature is also scrutinized by varying three temperatures of T_g (glass transition temperature of PEI), $T_g/2$, and $T_g/4$. Perfect impregnation, void-free content, and excellent surface finish are

achieved by the experiment with a spool tension of 2.5 N, a processing speed of 50 mm/min, and cooling die temperatures of $T_g/2$ and $T_g/4$.

The proposed geometry-based design in the first objective is unable to predict the internal geometry and mesoscopic morphology of the braids. Moreover, there are simplifications and uncertainties since fiber-to-fiber mechanical interactions have been neglected. To tackle those problems, we introduce a fiber-level model of biaxial braids as the second objective of this research. This objective proposes a modeling methodology to predict the 3D geometry and internal mesoscopic morphology of biaxial braids. Braided yarns are modeled as a bundle of virtual fibers using chains of truss elements. The simulations of two common braid patterns of the diamond (1/1) and regular (2/2) are validated by a comprehensive quantitative comparison with X-ray micro-computed tomography (CT) scans of braided carbon fibers. We find that the fiber-level frictional behavior is able to explain the jammed state of braids, wherein the frictional dissipation energy quickly grows once the braid has stable elongation, diameter, and braid angle. Parametric studies illustrate how the decrease in the coefficient of friction affects the yarn cross-sectional shape, whereas it has an insignificant effect on the jamming state. Models also reveal that changing a wide range of the fiber modulus of elasticity hardly impacts the mesoscopic geometry configuration of the braids.

The proposed methodology described in the second objective is used to simulate the thermoplastic braid-trusion forming process as the third objective. A new modeling methodology is developed that begins with the simulation of a dry fiber-level biaxial braid made of commingled yarns before modeling the braid-trusion process. A thermoplastic composite rod is successfully pultruded according to the simulation. Significantly, pultrusion changes the braid architecture, which is accurately predicted by the model through macroscopic measurements of 7.6% pitch elongation, 44.0% diameter reduction, and 45.0% nominal angle reorientation. Pultrusion also compacts braided yarns together, resulting in over 60% of the local fiber volume fraction, quantified using X-ray CT scans. The high local fiber volume fraction and the internal geometry of the braid-truded rod are predicted by the model. The fiber-level braid model provides access to the local fibers orientation distribution. The fiber-level (micro-scale) analysis visualizes three distributions of the local fiber orientation of in-plane, out-of-plane, and the angle with respect to the longitudinal braid axis. Notably, distributions of the local fiber orientation varied along the braid radius. Fibers are oriented within a certain range of radius around 30 – 70% and 60 – 100% of the outer radius before

and after pultrusion, respectively. Conversely, the fiber orientation distributions are uniform along the braid's longitudinal axis. The parametric study demonstrates that the increase of the coefficient of friction between the fibers and the die wall ranging from 0.1 to 0.6 has an insignificant effect on the local fiber orientation. The frictional dissipated energy remains almost constant for the low (0.1) and medium (0.4) coefficients of friction between the fibers and the die wall, while it linearly increases for the process with the high coefficient of friction (0.6).

This study opens the door to the future simulation-based design of composite manufacturing with complex processes. Specifically, the proposed numerical method can serve as a platform to accelerate the design of composites manufacturing in numerous fields such as the braiding process on mandrels with complex shapes and thermoplastic compression molding process using complicated molds. Moreover, the proposed numerical tool can lower the use of experimental methods such as CT scan to investigate the geometry, mesoscopic morphology, and local fiber orientation of composite materials, which may require overpriced tools.

TABLE OF CONTENTS

DEDICATION	III
ACKNOWLEDGEMENTS	IV
RÉSUMÉ.....	V
ABSTRACT	VIII
TABLE OF CONTENTS	XI
LIST OF TABLES	XV
LIST OF FIGURES.....	XVI
LIST OF SYMBOLS AND ABBREVIATIONS.....	XXII
ENDICES	XXIV
CHAPTER 1 INTRODUCTION.....	1
1.1 Dissertation structure.....	2
CHAPTER 2 LITERATURE REVIEW	3
2.1 Thermoplastic braid-trusion	3
2.1.1 Manufacturing process	3
2.1.2 Thermoplastic braid-trusion modeling	5
2.2 2D Braids.....	6
2.2.1 Braid types and patterns	6
2.2.2 Biaxial and triaxial braid deformation mechanism	7
2.3 Simulation of textile reinforcements of composites.....	8
2.3.1 Geometrical approaches	9
2.3.2 Continuum models (macroscale).....	10
2.3.3 Discrete models	11
2.3.4 Yarn-level simulation (mesoscale).....	11

2.3.5 Fiber-level simulation (microscale)	12
CHAPTER 3 PROBLEMS IDENTIFICATION, RESEARCH OBJECTIVES AND COHERENCE OF ARTICLES	18
3.1 Problems' identification	18
3.2 Research objectives	19
3.3 Coherence of articles	20
CHAPTER 4 THERMOPLASTIC COMPOSITE ROD MANUFACTURING USING BIAxIAL BRAID-TRUSION	22
4.1 Introduction	22
4.2 Methodology	23
4.2.1 Material	23
4.2.2 Pultrusion apparatus and process	23
4.2.3 Braid and braid-trusion design	25
4.3 Results	28
4.3.1 Braid geometry measurements	28
4.3.2 Parametric studies	29
4.4 Conclusion.....	32
CHAPTER 5 ARTICLE 1: FIBER-LEVEL NUMERICAL SIMULATION OF BIAxIAL BRAIDS FOR MESOSCOPIC MORPHOLOGY PREDICTION VALIDATED BY X-RAY COMPUTED TOMOGRAPHY SCAN	34
Highlights	34
Abstract	35
5.1 Introduction	37
5.2 Modeling methodology	40
5.2.1 Yarn discretization and mesh generation	41

5.2.2	Contact detection.....	42
5.2.3	Periodic boundary conditions (PBCs).....	43
5.2.4	Loading strategy.....	43
5.3	Experimental methods.....	44
5.3.1	Braid fabrication.....	44
5.3.2	X-ray micro-computed tomography (micro-CT)	45
5.3.3	Quantitative analysis method	45
5.4	Results and discussion.....	47
5.4.1	Numerical convergence study	47
5.4.2	Geometrical convergence study	47
5.4.3	Validation.....	48
5.4.4	Parametric studies	52
5.5	Conclusions	57
	Acknowledgments.....	58
CHAPTER 6 ARTICLE 2: MULTISCALE NUMERICAL SIMULATION OF THE FORMING PROCESS OF BIAXIAL BRAIDS DURING THERMOPLASTIC BRAID-TRUSION: PREDICTING 3D AND INTERNAL GEOMETRY AND FIBER ORIENTATION DISTRIBUTION.....		59
	Highlights	59
	Abstract	60
6.1	Introduction	62
6.2	Workflow	67
6.3	Modeling methodology	70
6.4	Experiments.....	73

6.4.1	Materials.....	73
6.4.2	Braiding.....	73
6.4.3	Pultrusion	73
6.5	Characterization	75
6.5.1	X-ray micro computed tomography scan (CT scan)	75
6.5.2	Quantitative analyses.....	76
6.6	Results and Discussion.....	80
6.6.1	Macroscopic analysis	80
6.6.2	Mesoscopic analysis	82
6.6.3	Microscopic analysis	86
6.7	Conclusion.....	93
	Acknowledgments	94
CHAPTER 7	GENERAL DISCUSSION.....	95
7.1	General discussion on published achievements	95
7.2	General discussion on unpublished achievements	95
7.2.1	Inter-fibers frictions effects	95
7.2.2	Friction effects between fibers and the die wall.....	99
CHAPTER 8	CONCLUSION AND RECOMMENDATION	103
8.1	Contribution	103
8.2	Limitation and future research direction	105
	REFERENCES.....	107
	APPENDICES.....	116

LIST OF TABLES

Table 4.1 PEI material properties [86, 87].	23
Table 4.2 The manufacturing parameters during experiments.	25
Table 4.3 Designed braid pitch, braid angle, fiber volume fraction, and the overfilling ratio at dies' exit.	27
Table 4.4 Measurement on the braid preform before pultrusion and braid-truded rod after pultrusion.	28
Table 5.1 Material properties of carbon yarn [99, 100].	44
Table 5.2 Yarn cross-section area comparison.	51
Table 5.3 Yarn's aspect ratio comparison.	52
Table 6.1 Validation of the prediction of the in-plane fiber orientation.	88
Table 6.2. Comparison of the mean of local fiber orientations with the nominal braid angle.	91
Table 7.1 Effect of the inter-fibers coefficient of friction on the local fiber orientation.	98
Table 7.2 Effect of the coefficient of friction between braided fibers and the die wall on the local fiber orientations.	101

LIST OF FIGURES

Figure 1.1 Thermoplastic braid-trusion system. The braiding machine feeds the braided commingled yarns into the system. Puller draws the braid into the pre-heater. The polymer fibers melt in heated dies, impregnate the reinforcement fibers, and solidify upon cooling. ..2	
Figure 2.1 Pullbraiding line with contact preheating [2]	3
Figure 2.2 Typical hybrid yarns for manufacturing of thermoplastic composites. a) Parallel yarn, b) commingled yarn, c) pre-consolidated tape.	5
Figure 2.3 (a) Model of circumferential deformation of triaxial braids during braid-trusion. (b) Cross-section image of the braid-truded L-shaped beam [5].	6
Figure 2.4 Types of braid structures.....	7
Figure 2.5 Deformation of biaxial braids under tensile (F_t) and compressive (F_c) loads ($\alpha_t < \alpha < \alpha_c$).	8
Figure 2.6 Categories of the fabric modelling.....	9
Figure 2.7 Peirce's unit cell model [39]. (a) The circular yarn cross-section. (b) The elliptic arm-cross section.....	9
Figure 2.8 (a) The racetrack yarn cross-section [39]. (b) The lenticular yarn cross-section [40]..	10
Figure 2.9 2D woven TexGen model [35].	10
Figure 2.10 Hemispherical forming of a continuum model of an interlock reinforcement [50]....	11
Figure 2.11 Digital element concept [63]. (a) 3D braid. (b) Discretization of the yarn. (c) 3D contact element.	12
Figure 2.12 Multi-chain digital element models [64]. (a) 2D woven; (b) 3D braid.....	13
Figure 2.13 Static relaxation procedure for 3D braid fabric [62].....	13
Figure 2.14 Multi-step and multi-level digital element dynamic relaxation [61].	14
Figure 2.15 Durville's models. (a) 2D Woven [65]; (b) Cable [78]; (c) Knot [66]; and (d) Ligament.	15

Figure 2.16 Gradual separation of the braided rope yarns in Durville's model [81].	16
Figure 2.17 3D woven fabric model [69]. (a) Cross-section view; (b) Top view.	16
Figure 2.18 2D woven before and after compaction [70].	17
Figure 4.1 Schematic view of the pultrusion apparatus.	24
Figure 4.2 Schematic of a cylindrical braid (a) and a flattened braid yarn along a pitch before (b) and after (c) passing through die i ($P_i > P_{i-1}$ and $D_i < D_{i-1}$).	26
Figure 4.3 Microscopy image at 200 \times .	29
Figure 4.4 The effect of spool tension on the composite rod. The cross-section of the manufactured rod with the spool tension of 2.5 N (a), 40 N (b) and 80 N (c).	30
Figure 4.5 The effect of speed on the composite rod. The cross-section of the braid-truded rod with 50 mm/min (a) and 150 mm/min (b).	31
Figure 4.6 The cross-section of the braid-truded rod with the cooling temperature of (a) T_g , (b) $T_g/2$ and (c) $T_g/4$.	32
Figure 5.1 Graphical abstract	36
Figure 5.2 Multiscale modeling framework for a biaxial braid. (a) Macro-scale braid with multifilament yarns. (b) Individual meso-scale multifilament yarn. (c) Individual micro-scale fibers modeled using chains of truss elements (one chain by fiber).	37
Figure 5.3 General overview of the modeling workflow. (a) A Python script generated the initial braid geometry in Abaqus FEA software. (b) Realistic braid geometry after the application of small loading on the initial braid geometry's end. (c) Validation of the methodology using micro-CT scan data (P_i : braid pitch, D_i : braid diameter, α_i : braid angle ($i=0, 1$), $P_0 < P_1$, $D_0 > D_1$, $\alpha_0 > \alpha_1$).	40
Figure 5.4 Yarn discretization by fibers. (b) Yarn cross-section showing fibers located in concentric layers with an initial gap between fibers ($\text{Gap}_{\text{fibres}}$). L_n is the n th layer. The core (L_0) has one fiber. Number of fibers in each layer: $N_f L = 6n$ ($n=1, 2, \dots, L_n$). Number of total fibers: $N_f = (n = 1n = L_n 6n) + 1$. The (c) Constitutive components of a fiber: truss elements connected with three degrees of freedom node (translational motions).	42

Figure 5.5 (a) Convergence of the elongation of the braid pitch under 1N tensile load. (b-g) Geometrical convergence of the braid cross-section against the number of fibers per yarn. (b) 7 fibers/yarn. (c) 19 fibers/yarn. (d) 37 fibers/yarn. (e) 61 fibers/yarn. (f) 91 fibers/yarn. (g) Comparison of the superimposed cross-sections.	48
Figure 5.6 Validation of the diamond (1/1) braid model by comparing with the CT images. (a-b) Two different cross-sections comparison. The red closed areas specify the similar yarn cross-section shape between models and CT images. (c) The 3D isometric view comparison between the model and CT scan.	49
Figure 5.7 Validation of the regular (2/2) braid model by comparing with the CT images. (a-b) Two different cross-sections comparison. The red closed areas specify the similar yarn cross-section shape between models and CT images. (c) The 3D isometric view comparison between the model and CT scan.	50
Figure 5.8 Effect of the fiber-level friction on the jammed state and mesoscopic morphology of braids. Diagrams of the frictional dissipation energy against (a) elongation, (b) dimensionless diameter, and (c) braid angle. (d-f) Comparison of braid cross-sections in the middle of braid pitch. (e-g) Quantitative analysis of one of the yarns' cross-sections in the middle of braid pitch (j) Comparison of the yarn aspect ratio. (k) Comparison of the jammed angle. All comparisons were performed for $\mu=0.1, 0.3, \text{ and } 0.6$	55
Figure 5.9 Effect of the fiber-level elastic modulus on the jammed state and mesoscopic morphology of braids. Diagrams of the force against (a) elongation, (b) dimensionless diameter, and (c) braid angle. (d-f) Comparison of braid cross-sections in the middle of braid pitch. (e-g) Quantitative analysis of one of the yarns' cross-sections in the middle of braid pitch (j) Comparison of the yarn aspect ratio. (k) Comparison of the jammed angle. All comparisons were performed for $E=60, 150, \text{ and } 300 \text{ MPa}$	56
Figure 5.10 Comparison of the crimp percentage between diamond and regular braided patterns at the jammed state for coefficients of friction of $\mu = 0.1, 0.3, \text{ and } 0.6$ (a) and moduli of elasticity of $E=60, 150, \text{ and } 300 \text{ GPa}$ (b).	57
Figure 6.1 Graphical abstract	61

- Figure 6.2 (a) Triaxial and (b) biaxial braid structures. (c) Deformation of the biaxial braid under tensile (F_t) and compressive (F_c) loads. α is the braid angle with respect to the longitudinal braid axis ($\alpha_t < \alpha < \alpha_c$).63
- Figure 6.3 Thermoplastic braid-trusion system. The braiding machine feeds braided commingled yarns into the system. After preheating, the polymer fibers melt in heated dies, impregnate the reinforcement fibers, and solidify upon cooling.64
- Figure 6.4 Workflow of the modeling procedure. (a,b) Step I: model of braided preform. (a) Initial braided preform geometry. The fibers cross-section area was considered the sum of reinforcement and matrix fibers area as commingled fibers. (b) Relaxed unconsolidated braided preform geometry. (c-h) Step II: braid-trusion simulation. (c) Braided reinforcement geometry in which fibers cross-section area is considered as the reinforcement fibers' area only. P_0 , D_0 , and loading conditions are the same as the braided preform. (d-g) Braid-trusion simulation in which the pultrusion die moved over the braid. (d) Braid before pultrusion. (e) Magnification of the braid before entering the die. (f) During pultrusion. (g) The braid is inside the strait section of the pultrusion die. (h) Magnification of the braid-truded rod.....69
- Figure 6.5 (a) Commingled yarn cross-section area. The total cross-section area of fibers (A_t) was determined as the sum of reinforcement (A_f) and matrix (A_m) filament area in the commingled fibers before pultrusion. (b) Reinforcement yarn cross-section area. As the matrix fibers were melted during pultrusion, the total cross-section area of fibers was lowered to only reinforcement fibers area (A_f).71
- Figure 6.6 Rigid die meshed using 3D four-node quadrilateral discrete rigid elements.....72
- Figure 6.7 Schematic of cross-section view of the multi-die pultrusion system. The apparatus consisted of a tension-controlled creel, preheater, four heated dies, cooling die, puller, and control unit.75
- Figure 6.8 Global and local systems and definition of α_{iz} , θ_{itz} and ϕ_{itz} for an element with two nodes of i and $i+1$. (a) A cylindrical surface with the same longitudinal axis with the braid is fitted to node i . The n -coordinate is normal to the cylindrical surface in the radial direction, the z -coordinate is parallel to the longitudinal braid axis, and the tz -plane is the plane tangent to the cylindrical surface. α_{iz} is the angle between the element and the z -coordinates. (b) The

angle of θ_{itz} is the in-plane angle between the element's projection in the tz -plane and z -coordinate. The angle of φ_{itz} is the out-of-plane angle between the element and its projection in the tz -plane. r_i and ω_i determine the position of the origin of the local coordinates related to the global coordinates.78

Figure 6.9 Quantitative macroscopic validation of the model before and after pultrusion. Comparison of the pitch length (a), the braid diameter (b), and the nominal braid angle (c). (d) Variations of the braid architecture after pultrusion.82

Figure 6.10 Cross-section image of the carbon fiber/PEI braid-truded rod.83

Figure 6.11 (a,b) 3D segmented clockwise (green) and counterclockwise (orange) braided yarns. (c) Comparison of the braid-truded yarns cross-sections morphology between the model and CT images along the yarn path. (d) 3D portion of the model to extract five cross-sections to compare with the equivalent CT images.85

Figure 6.12 Comparison of the yarn cross-section area of the braid-truded rod along the yarn path between the CT data and predicted values for five slices of the clockwise (a) and counterclockwise (b) yarns. Local fiber volume fraction corresponding to the clockwise (c) and counterclockwise (d) yarns along the yarns path.86

Figure 6.13 Validation of the prediction of the fibers orientation. (a,b) Extracted model's slice from middle of the braid in the yz -plane. (c) Zoomed section of the model's slice showed the fiber distribution. (d) Equivalent CT slice divided 60 portions to measure the fibers orientation. (e-g) Zoomed portions of the CT slice illustrated fiber orientation measurements.87

Figure 6.14 Distribution of the in-plane fiber orientation along the radius for the braided preform (a) and pultruded braid (b). Distribution of the out-of-plane fibers orientation along the radius for the braided preform (c) and pultruded braid (d). Distribution of the fibers orientation with respect to the z -axis along the radius for the braided preform (e) and pultruded braid (f). ...89

Figure 6.15 Distribution of the in-plane fiber orientation along the pitch length for the braided preform (a) and pultruded braid (b). Distribution of the out-of-plane fibers orientation along the pitch length for the braided preform (c) and pultruded braid (d). Distribution of the fibers

orientation with respect to the z-axis along the pitch length for the braided preform (e) and pultruded braid (f).	92
Figure 7.1 Effect of coefficients of friction on the in-plane fiber orientation distribution. Distribution of θ_{tz} along the braid radius for $\mu = 0.1$ (a), $\mu = 0.4$ (b), and $\mu = 0.6$ (c).	96
Figure 7.2 Effect of inter-fibers friction on the out-of-plane fiber orientation distribution. Distribution of φ_{tz} along the braid radius for $\mu = 0.1$ (a), $\mu = 0.4$ (b), and $\mu = 0.6$ (c).	97
Figure 7.3 Effect of coefficients of friction on the local fiber orientation distribution with respect to the braid's longitudinal axis. Distribution of α_z along the braid radius for $\mu = 0.1$ (a), $\mu = 0.4$ (b), and $\mu = 0.6$ (c).	97
Figure 7.4 Effect of the inter-fibers coefficient of friction on the local fiber orientation.	98
Figure 7.5 Effect of friction between fibers and the die wall on the in-plane local fiber orientation distribution. Distribution of θ_{tz} along the braid radius for $\mu = 0.1$ (a), $\mu = 0.4$ (b), and $\mu = 0.6$ (c).	99
Figure 7.6 Effect of friction between fibers and the die wall on the out-of-plane local fiber orientation distribution. Distribution of φ_{tz} along the braid radius for $\mu = 0.1$ (a), $\mu = 0.4$ (b), and $\mu = 0.6$ (c).	100
Figure 7.7 Effect of friction between fibers and the die wall on the local fiber orientation distribution with respect to the braid's longitudinal axis. Distribution of α_z along the braid radius for $\mu = 0.1$ (a), $\mu = 0.4$ (b), and $\mu = 0.6$ (c).	100
Figure 7.8 Effect of the coefficient of friction between braided fibers and the die wall on the local fiber orientations.	101
Figure 7.9 Effect of coefficient of friction between fibers and the die wall on the frictional dissipated energy.	102
Figure A.1 Smooth step amplitude curve.	116
Figure B.1 (a) Diamond braided carbon fiber with 12 yarns. (b) Regular braided carbon fiber with 8 yarns. (c) Fixture mechanism for holding the braid during CT scanning.	117

LIST OF SYMBOLS AND ABBREVIATIONS

2D	Two-dimensional
3D	Three-dimensional
α	Nominal Braid angle
α_i^z	Local fiber angle with respect to the z coordinates
δ	Yarn aspect ratio
ε	Elongation
θ_i^{tz}	Local in-plane fiber angle
μ	Coefficient of friction
ρ	Density
ρ_m	Melt specific gravity
ρ_s	Solid specific gravity
φ_i^{tz}	Local out-of-plane fiber angle
ω_i	Rotation mapping
CF	Carbon fiber
CT	Computed tomography
D	Braid diameter
DEA	Digital Element Approach
E	Modulus of elasticity
FEM	Finite element method
G	Modulus of rigidity
K_b	Bending stiffness

K_t	Torsional stiffness
l	Yarn major diameter
L	Fiber length
L_i^e	Element length
N_f	Number of fibers
N_y	Number of yarns
P	Braid pitch
PBC	Periodic boundary condition
PEEK	Poly ether ether ketone
PEI	Polyethylenimine
r_i	Node's radius
T_g	Glass transition temperature
T_m	Melting point temperature
u	Deformation
V_i^x	Nodal vector in the x direction
V_i^y	Nodal vector in the y direction
V_i^z	Nodal vector in the z direction
\vec{V}_i^{xyz}	Nodal vector in global coordinates
V_i^n	Nodal vector in the n direction
V_i^t	Nodal vector in the t direction
\vec{V}_i^{ntz}	Nodal vector in local coordinates
w	Yarn minor diameter

ENDICES

Appendix A Smooth step amplitude curve	116
Appendix B Micro-CT scanning procedure of dry carbon fiber braids	117
Appendix C The list of publications and presentations extracted from the thesis	118

CHAPTER 1 INTRODUCTION

Advanced composites materials have been increasingly used in new engineering applications already made of conventional materials such as metal alloys. This is due to composites' superior features such as the ability to tolerate high temperature, extreme lightweight, high stiffness, excellent strength, proper fatigue resistance, and high corrosion resistance. Two fundamentals constituents of composite materials are fibers and matrix. Fibers reinforce the composites and supply their strength and stiffness, while the matrix binds the fibers together and transfers loads between them. The most common reinforcements are carbon, glass, Kevlar, and natural fibers. Thousands of micron-sized fibers are grouped together to make a yarn. Yarns are used as composite reinforcements in the form of unidirectional fibers and textiles fabricated by weaving, knitting, and braiding. Typical matrix materials are polymers, ceramics, and metals. There are two polymer matrix systems of thermosets and thermoplastics. Thermoset resins have reasonably low viscosities at room temperature, for instance, Polyesters have about 1 Pa.s at room temperature. Conversely, viscosities of thermoplastic resins are extremely high even at a high temperature, for example, PEEK has approximately 10^3 Pa.s at 400 °C. Consequently, there are more obstacles in the way of thermoplastic composites manufacturing. While the thermoplastic matrix can provide higher mechanical properties and more appropriate environment resistance. Moreover, recycling of the thermoplastic composites is easier due to inherent properties of thermoplastic materials.

A wide range of manufacturing techniques is available, from manual operations to complex automated solutions equipped with costly tools such as advanced robots. Few fully automated techniques are applicable to produce composites continuously with relatively affordable manufacturing tooling. One of these techniques is braid-trusion, which is a combination of high-automated techniques of braiding and pultrusion. Braiding is a traditional textile fabrication technique that is highly attractive to manufacture composite reinforcements due to their multi-directional fiber arrangement. Pultrusion is a continuous composite manufacturing process to produce constant cross-section profiles using both thermoset and thermoplastic matrix systems. Figure 1.1 shows the thermoplastic braid-trusion system. The hybrid yarns are used for the thermoplastic braid-trusion process. The pulling device pulls the braided fibers into the preheated chamber. The braid is then pulled into heated die to melt the thermoplastic fibers for impregnation of reinforcement fibers. The braid finally solidifies in a consecutive cooling die.

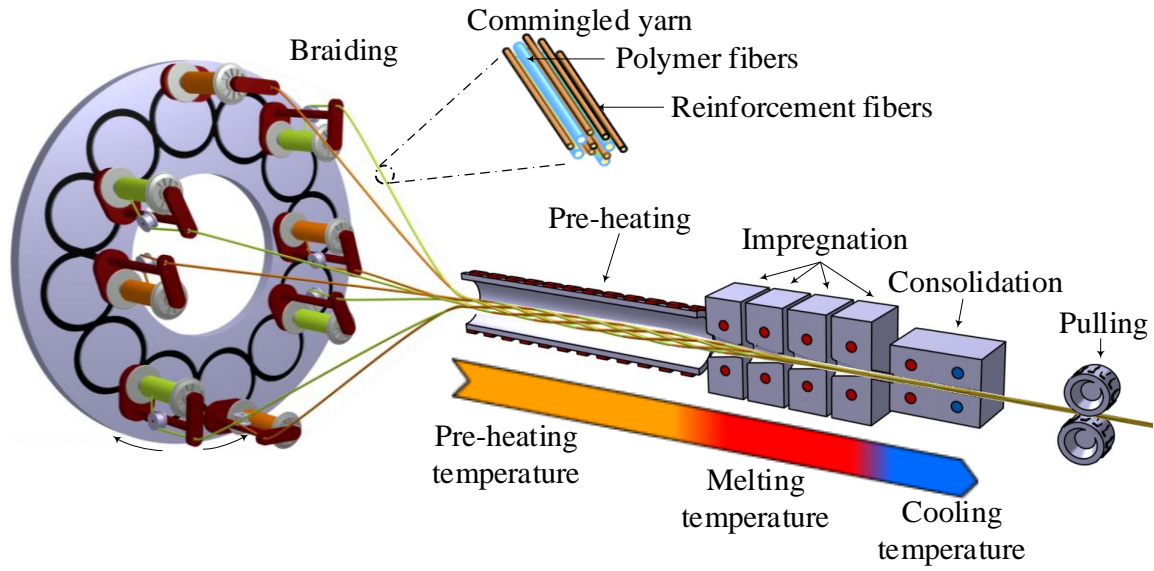


Figure 1.1 Thermoplastic braid-trusion system. The braiding machine feeds the braided commingled yarns into the system. Puller draws the braid into the pre-heater. The polymer fibers melt in heated dies, impregnate the reinforcement fibers, and solidify upon cooling.

In this dissertation, we investigate the manufacturing of thermoplastic composite rods using braid-trusion. We introduce a modeling methodology to simulate the forming process of biaxial braids during thermoplastic braid-trusion. The proposed multiscale model can predict the 3D and internal geometry of biaxial braids as well as their fiber orientation distribution.

1.1 Dissertation structure

The dissertation consists of seven chapters. Chapter 1 introduced the scope of this thesis. After a literature review in Chapter 2, the problem will be identified in Chapter 3 with descriptions of research objectives. The main achievements of the research are explained in detail in Chapters 4, 5, and 6. Chapter 4 contains the evaluation of the manufacturing of thermoplastic composite rods using biaxial braid-trusion. Chapter 5 presents a fiber-level finite element model of biaxial braids validated by experimental quantification using CT scans. Chapter 6 develops a modeling methodology to simulate the forming process of biaxial braids during thermoplastic braid-trusion. Chapter 7 provides a general discussion of the results. Chapter 8 presents a conclusion of the research, discusses the limitations, and outlines recommendations for future work.

CHAPTER 2 LITERATURE REVIEW

In this chapter, the studies related to the field of this thesis will be briefly reviewed. The literature on the manufacturing process of thermoplastic braid-trusion and its models are concisely surveyed in Sections 2.1. Moreover, we specifically survey the literature on 2D braids in Section 2.3. Simulations of textile reinforcements of composites are also reviewed in Section 2.4.

2.1 Thermoplastic braid-trusion

2.1.1 Manufacturing process

Braid-trusion is a composite manufacturing technique using a braided textile preform that is pulled into a pultrusion die to produce constant cross-section profiles [1-10]. Figure 2.1 shows a common thermoplastic braid-trusion apparatus [2]. The braiding machine feeds the braided yarns into the pultrusion line. The braided yarns are composed of hybrid yarns combining reinforcement and thermoplastic fibers. Pulling device drags the braid into a pre-heater. The braid is preheated to a temperature close to the thermoplastic filaments melting point in the pre-impregnation die [1]. Preheating the braid decrease the required time to melt the thermoplastic polymer in the pultrusion die [2]. After preheating, the polymer fibers are melted in heated dies (pultrusion die) to impregnate the reinforcement fibers, and solidified in a successive cooling die. The pultrusion die usually consists of a conical zone allowing overfilling of the die. This overfilling creates a back-flow of polymer towards the conical zone entrance [4]. This back-flow helps create pressure to impregnate reinforcement fibers by the polymer.

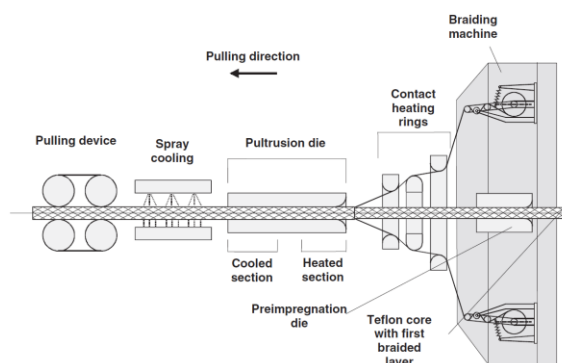


Figure 2.1 Pullbraiding line with contact preheating [2]

2.1.1.1 Thermoplastic materials

Both thermoplastic and thermosetting matrix systems can be used in pultrusion. There are more obstacles in the way of production of thermoplastic composites than thermosets due to the high viscosity of thermoplastic materials [11-14]. The thermoplastic matrix must be melted to impregnate reinforcement fibers and consecutively solidify upon cooling. The molecular structure of melted thermoplastic polymers composed of irregular and entangled structure. Some polymers preserve such a disordered structure upon cooling and are readily turned into amorphous solids (non-crystalline, glassy solids). In other polymers, irregular molecular structures are reconstructed into parallel alignments upon cooling, while some entangled structures prevent such alignments. Therefore, these polymers are neither crystalline nor amorphous and are categorized as semi-crystalline. Polyethylenimine (PEI) is an example of amorphous polymers and polyetheretherketone (PEEK) is a semi-crystalline polymer [11, 12].

2.1.1.2 Melting and glass transition temperatures

At a certain elevated temperature, the intermolecular forces weaken and thermoplastic materials melt, which is characterized as the melting temperature (T_m). The glass transition is the gradual and reversible transition in amorphous materials from a melt state into a relatively brittle glassy state during the cooling process. The range of temperature at which glass transition occurs is characterized by the glass transition temperature (T_g). In semi-crystalline polymers, the glass transition occurs only within the amorphous regions of the material [11]. The amorphous polymers can melt above T_g ; however, since their viscosity drops by increasing the temperature, their processing temperature is usually much higher than T_g and T_m .

2.1.1.3 Hybrid yarns

The high viscosities of thermoplastic materials and their solid-state at room temperature allow them to be produced in the form of fibers. The thermoplastic fibers can be mix with reinforcement fibers to create hybrid yarns [15]. Figure 2.2 illustrates the common hybrid yarns, which are the parallel hybrid (co-wound), commingled, and pre-consolidated tapes. The parallel hybrid yarn is composed of side by side reinforcement and thermoplastic fibers [15]. The commingled yarn is an intimate mixture of the reinforcement and thermoplastic fibers [15]. In the pre-consolidated tape, fibers are

pre-impregnated with a thermoplastic polymer [15]. The main advantages of hybrid yarns are low impregnation flow path length and ease of handling [15].

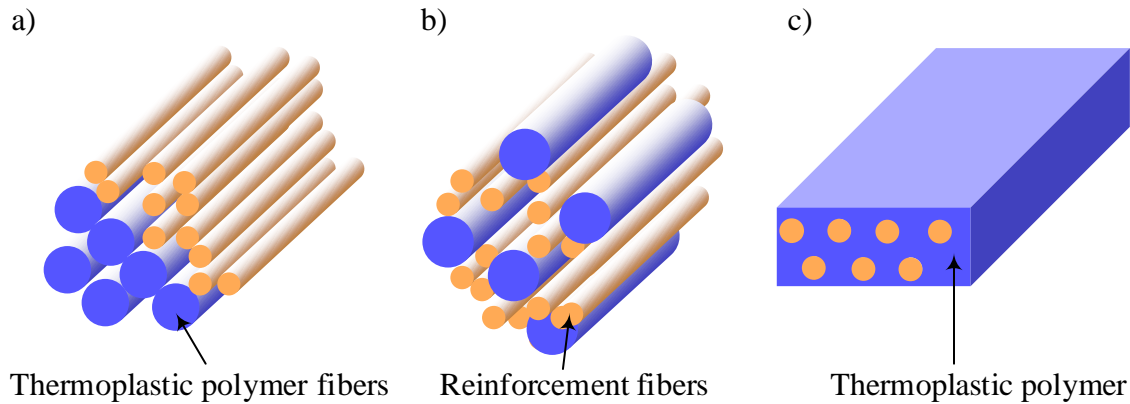


Figure 2.2 Typical hybrid yarns for manufacturing of thermoplastic composites. a) Parallel yarn, b) commingled yarn, c) pre-consolidated tape.

2.1.1.4 Thermoplastic braid-trusion limitations

The thermoplastic braid-trusion technique has not yet become a mass production process in the market. The main reason is the too low production rate as the high viscosity of thermoplastic materials [8]. Speeding up the process decreased the impregnation rate of the fibers, increased the void content, and increased the pulling force [1, 2, 6, 10]. The contact force between fibers and the die wall is one of the resistance forces that contributed to the high pulling force [16, 17].

2.1.2 Thermoplastic braid-trusion modeling

To overcome the challenges of the thermoplastic braid-trusion technique, it is necessary to simulate the process. Mathematical models to predict the pulling force and to describe the temperature and pressure distribution within a unidirectional thermoplastic composite were presented by Aström and Pipes [16, 17]. A model to estimate the degree of impregnation of the pultruded commingled yarns in two-scale of microscopic and macroscopic resin flow was presented by Kim et al. [18]. Bechtold et al. [2] also modeled the preheating process of the thermoplastic pultrusion.

A model of the forming process of braids during pultrusion has not been reported in reviewed studies. It is suspected that costly trial and error methods were used to carry out the process. Figure 2.3a shows a geometrical model for braided tube to simulate the braid-trusion process developed

by Laberge Lebel and Nakai [5]. They manufactured an L-shaped thermoplastic beam using this model, as illustrated in Figure 2.3b. Their model showed the circumferential deformation of a triaxial braid during compression in the die to achieve correct filling of the pultrusion die. They illustrated that only the circumferential (lateral) deformation of triaxial braids occurs during the process since the axial yarns in triaxial braids prevent the longitudinal deformation (Figure 2.3a). Moreover, no simulation procedure was found that could help the design of biaxial braids for braid-trusion since longitudinal deformation of the braid also occurs during pultrusion in addition to the lateral deformation.

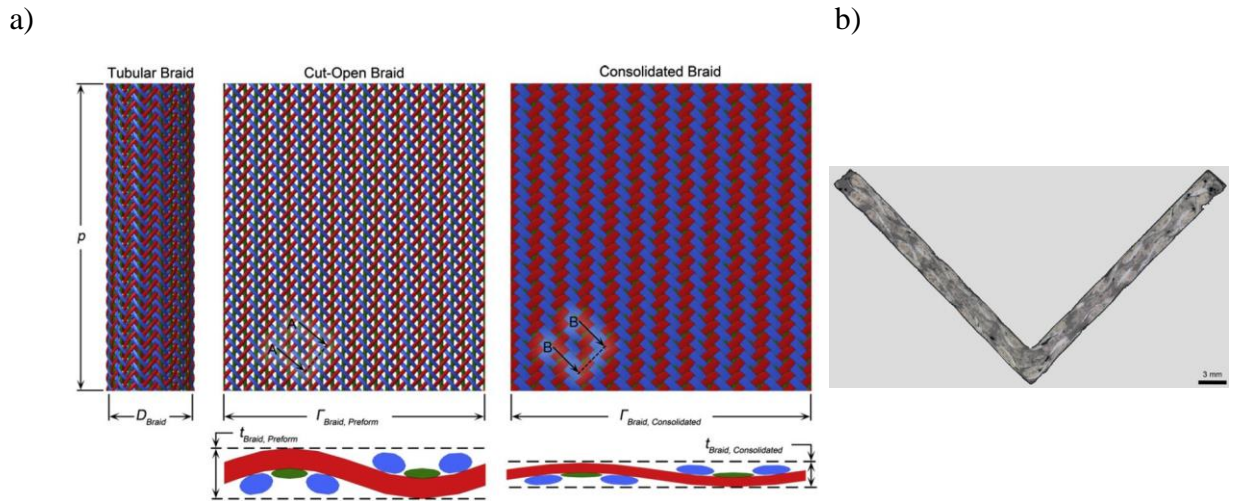


Figure 2.3 (a) Model of circumferential deformation of triaxial braids during braid-trusion. (b) Cross-section image of the braid-truded L-shaped beam [5].

2.2 2D Braids

Braids are ancient fabrics that have captured new applications today [19]. They offer remarkable mechanical properties due to their oriented fibers [13, 19, 20]. Braids have high formability into complex shapes [21]. Braiding also has a high-level of automation [13]. Because of these benefits, braids have received much attention in composites manufacturing [11, 13].

2.2.1 Braid types and patterns

Figure 2.4 shows the different types of 2D and 3D braids. The two more commonly used 2D braids are biaxial and triaxial braids [20]. The biaxial braid is described by two yarn systems that are

interlaced in a specified braiding angle. A third axial yarn system can be added along the braid's longitudinal axis to create a triaxial braid [20]. As seen in Figure 2.4, there are four typical biaxial braid patterns. In diamond, regular and hercules braids, yarns are intertwined every one, two, or three yarns respectively. Basket braids have a two-yarn over two-yarn pattern [20, 22].

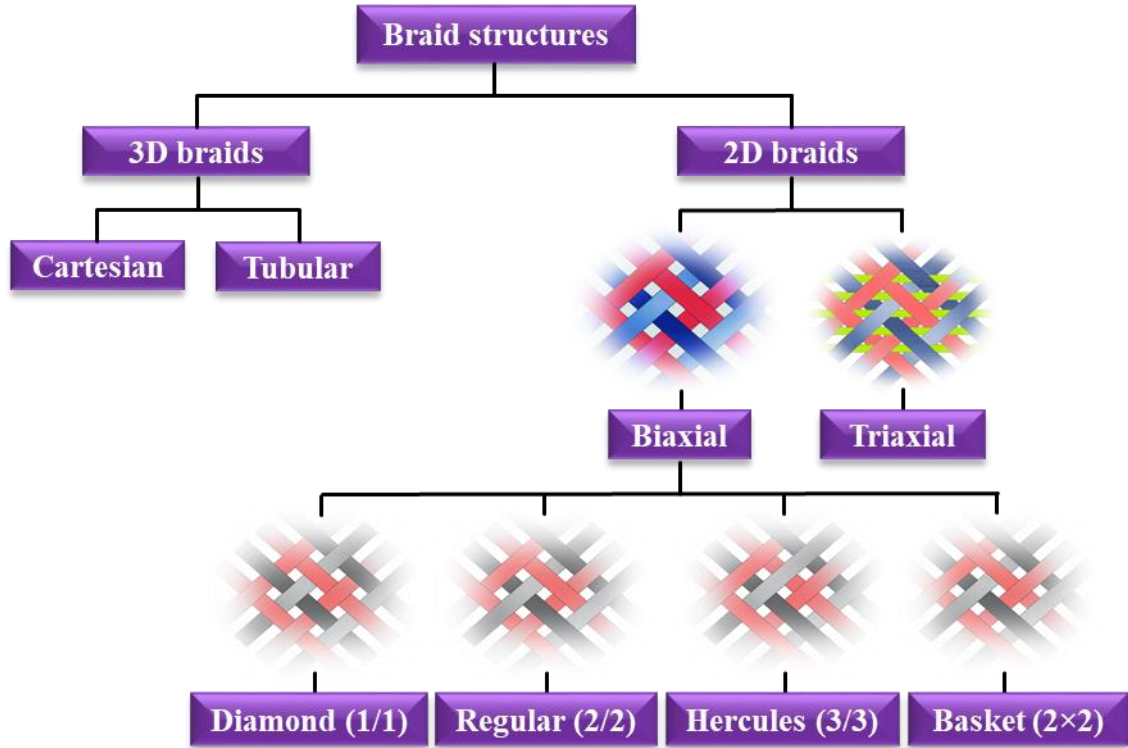


Figure 2.4 Types of braid structures.

2.2.2 Biaxial and triaxial braid deformation mechanism

Figure 2.5 shows the formability of the biaxial braid under axial loads. The biaxial braid structure easily deforms under axial tensile and compressive loads [20]. When tensile axial forces are applied to the biaxial braid structure, the braid stretches and its diameter considerably reduces, conversely, the compressive force leads to a reduction in pitch length and an expansion in diameter. These deformation mechanisms of biaxial braids also greatly change the braid angle [20, 23-25]. When biaxial braids are subjected to tensile loads, braids finally reach a state wherein the diameter no longer decreases. At this state, the braid is *jammed*. The braid angle reaches a stable state that called jammed angle or locked angle [20, 23]. There is evidence to suggest a hypothesis that the inter-

fibers friction significantly contributes to this phenomenon, although no research has been found in reviewed works.

In contrary of biaxial braids, the structure of triaxial braids is more stable and they do not easily deform under longitudinal loads [20, 23-25]. Axial yarns in triaxial braids secure the braid structure and prevent large longitudinal deformation of braids under tensile loads.

Most studies described in section 2.1 only used triaxial braids as the reinforcements to manufacture composites through the thermoplastic braid-trusion process. No report was found on using biaxial braids for thermoplastic braid-trusion. The deformation mechanism of triaxial braids can explain why most of the previously reviewed works used triaxial braids for thermoplastic braid-trusion.

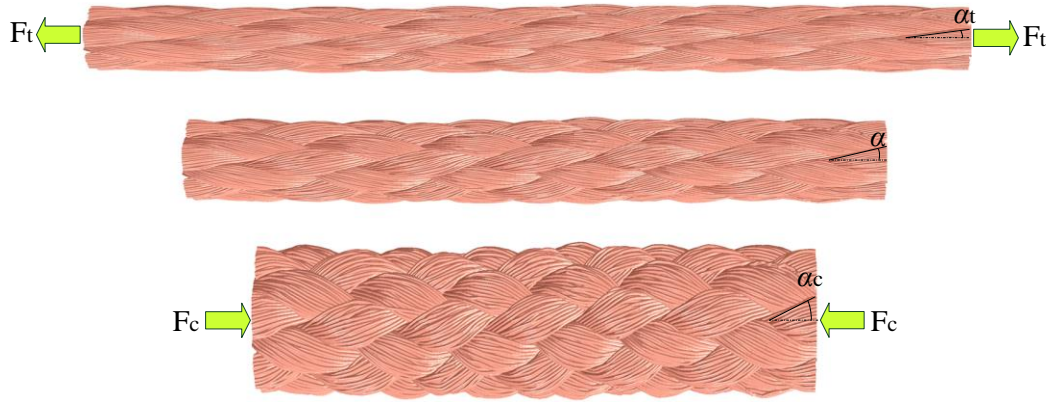


Figure 2.5 Deformation of biaxial braids under tensile (F_t) and compressive (F_c) loads ($\alpha_t < \alpha < \alpha_c$).

2.3 Simulation of textile reinforcements of composites

Figure 2.6 describes two main approaches for modelling textile architectures: the geometrical and the mechanical approaches. The mechanical approach is divided into two categories: the continuum and discrete category. The discrete category is subdivided into the yarn-level at mesoscale and the fiber-level at microscale. These fabric simulation methods will be reviewed in the following sections.

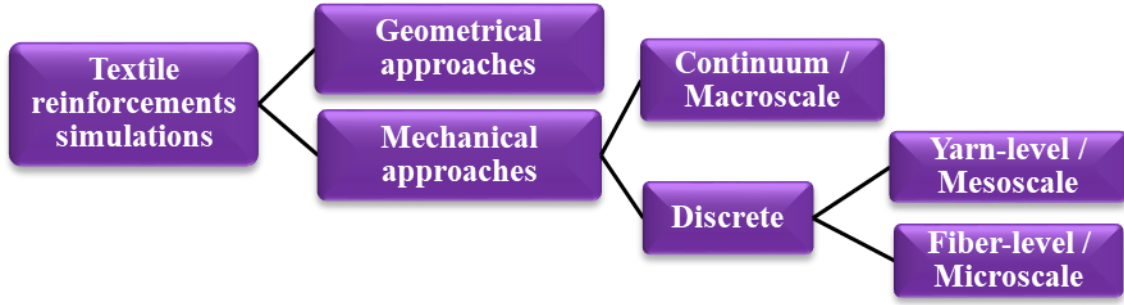


Figure 2.6 Categories of the fabric modelling.

2.3.1 Geometrical approaches

The geometrical approaches are built on the kinematic relations of the fabric [26-38]. The primary study of woven fabric structure was performed in 1937 by Peirce [26]. In his model, the smallest periodical repeating pattern, i.e., the unit cell, was made by assuming a circular yarn cross-section, uniform yarn cross-section along their length, incompressibility, and complete flexibility as shown in Figure 2.7a. These assumptions restricted the usage of this model to loose fabrics. Peirce modified its own model by using an elliptic yarn elliptic cross-section, as shown in Figure 2.7b. This improvement was sufficient to represent moderately loose fabric structures, but could not represent accurately tight fabric structures.

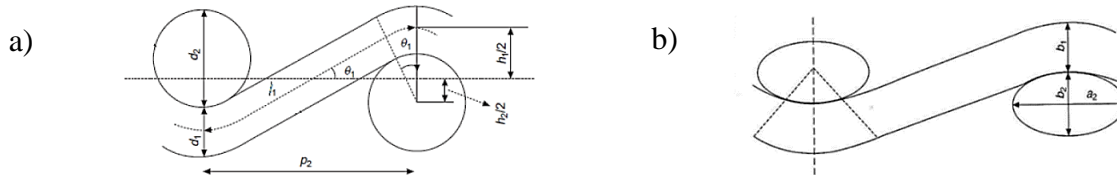


Figure 2.7 Peirce's unit cell model [39]. (a) The circular yarn cross-section. (b) The elliptic yarn cross-section.

In 1953, Brunnschweiller [27] reported an investigation of the geometry of the braid structure based on assumptions similar to those of Peirce. In order to analyze braiding angle and fiber coverage, he developed a single equation combining the braiding angle, pitch parameter, number of carriers, widths of braiding and axial tows. To overcome limitations of Peirce's model, Kemp [28] suggested a rectangle enclosed by two semicircular ends (i.e. racetrack shape) yarn cross-section and proposed a more accurately unit cell as shown in Figure 2.8a. However, the racetrack yarn cross-section shape could still not represent an accurate fabric unit cell. Hearle and Shanahan [40]

proposed an energy method to mechanically model the fabric. In their work, bending energy depends on the bending moment and yarn curvature. To decrease the bending energy, they used lenticular yarn cross section (Figure 2.8b). They showed in flattening, lenticular yarn cross section shape has lower curvature and so it has lower bending energy than race-track yarn cross-section shape. They assumed the constant yarn cross-section.

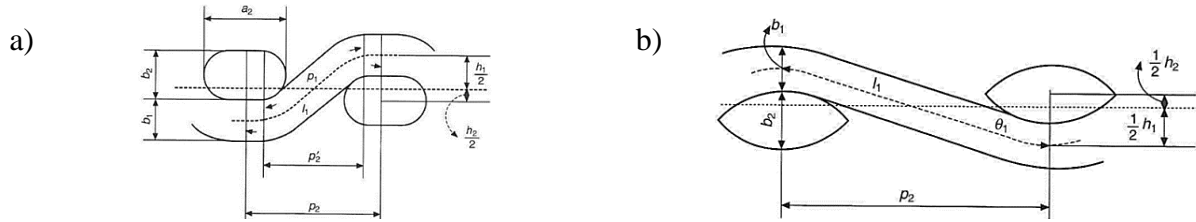


Figure 2.8 (a) The racetrack yarn cross-section [39]. (b) The lenticular yarn cross-section [40].

TexGen software was developed for modelling the textile geometry at the University of Nottingham [33-38]. A set of control points is specified for yarn path definition in TexGen. To determine a smooth yarn path, spline interpolations are used between those control points. The yarn cross-section shape is swept along the yarn path to generate the yarn. A woven TexGen model is shown in Figure 2.9.

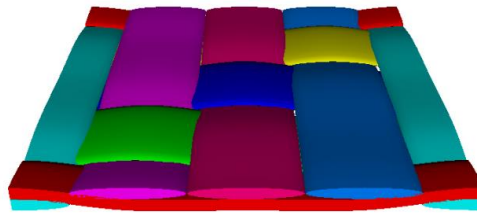


Figure 2.9 2D woven TexGen model [35].

In geometrical approaches, the effects of material and mechanical properties are not considered. Therefore, the geometrical approach suffers from imprecise representation of textile architectures. On the other hand, the mechanical approach considers the textile mechanical properties [41-70]. Thus, mechanical approaches can simulate the fabric behavior and architecture more accurately.

2.3.2 Continuum models (macroscale)

There are many continuum models which describe the draping and mechanical behavior of textile composite materials [41-50]. Figure 2.10 shows an example of a continuum model. The continuum

models define the textile as a solid continuum meshed with finite elements having anisotropic elastic properties. The hypothesis that considers the fabric as a continuum model is the lack of macroscopic slippages between yarns [50]. This hypothesis has been disproved for some cases that had macroscopic slippages between yarns [71]. Moreover, given the nature of such discrete structures of fiber reinforcements, the continuum models failed to care for the local fiber slippage [50]. Therefore, the continuum models are not able to represent the internal structure of the fabric during analysis. Discrete models can compensate this weakness.

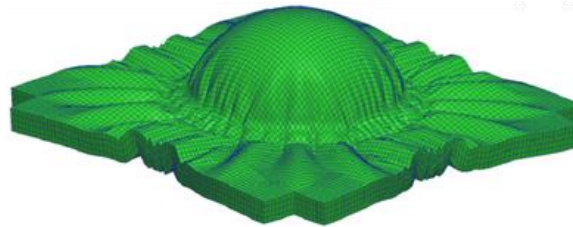


Figure 2.10 Hemispherical forming of a continuum model of an interlock reinforcement [50].

2.3.3 Discrete models

The fabric structure is inherently discrete. Fabrics are composed of discrete yarns intertwined together, and yarns, themselves, are composed of discrete fibers grouped together. Therefore, yarn and fiber interactions must be considered in the discrete models. The discrete approaches are categorized into two levels, the yarn-level [40, 51-60] and fiber-level simulation [61-70].

2.3.4 Yarn-level simulation (mesoscale)

The mesoscale approaches took into account the yarn as a solid continuum model [51, 56-60]. The yarn consists of discrete fibers, so the mesoscale approaches required a specific mechanical behavior to model the fibrous nature of the yarn. Albeit the mesoscopic approaches offered reliable models, they needed the complex constitutive laws of continuum mechanics [57].

Lomov and his team [56, 72-74] developed the WisTex software at the Katholieke Universiteit Leuven. WisTex is a commercial software that model the fabric meso-geometry, permeability of textile composites, and textile virtual reality. Yarn properties are defined by assigning the density, yarn dimension, yarn bending rigidity, and yarn transverse compressive stiffness. A constant lenticular or elliptical yarn cross-section shape can be considered by WisTex. A polynomial

function is used to determine the yarn path. The fabric final configuration is obtained by minimizing the yarns' bending energy. However, assuming a constant yarn cross-section shapes gives inaccurate results.

2.3.5 Fiber-level simulation (microscale)

Fiber-level simulations provide more realistic models that can describe the reality of the fabric physique. They allow to simulate the fiber-to-fiber movements and interactions inside the yarn as well as between yarns.

Figure 2.11 shows the Digital Element Approach (DEA) developed by Wang et al. [61-64] to determine the meso- and micro-geometry of textile fabrics and simulate the textile processes. They developed Digital Element Approach Fabric and Composite Analyzer (DFCA) software based on this approach at Kansas State University [75]. At the first attempt, Wang and Sun [63] modeled a 3D braid at the yarn level (Figure 2.11a). Each yarn was modeled as a rod element chain connected with frictionless pins (Figure 2.11b). A contact element was inserted between two contact nodes to model the yarn-to-yarn contact (Figure 2.11c). Simulation was performed using a quasi-static numerical procedure. Since each yarn contained a single digital chain, yarn cross-section was circular. Therefore, the numerical simulation did not provide a detailed fabric micro-geometry such as yarn cross-section deformation.

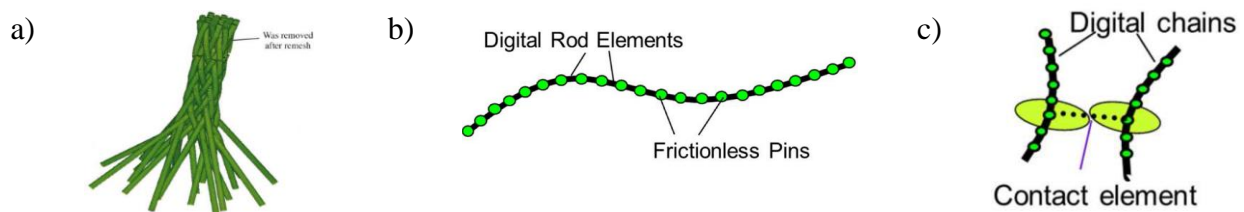


Figure 2.11 Digital element concept [63]. (a) 3D braid. (b) Discretization of the yarn. (c) 3D contact element.

Thereafter, Zhou et al. [64] upgraded the DEA textile modeling from the yarn level to the fiber level. In their new concept, named the multi-chain digital element analysis, each yarn was composed of a bundle of fibers. This concept is shown at Figure 2.12 for a 2D weaving and 3D braiding simulations. It allowed to simulate a much more realistic fabric deformation due to the motion of fibers inside the yarns. Hence, both yarn cross section deformation and yarn movement

could be extracted during the textile deformation simulation. Nevertheless, this method was inefficient owing to great computer resources needed and lengthy simulations.

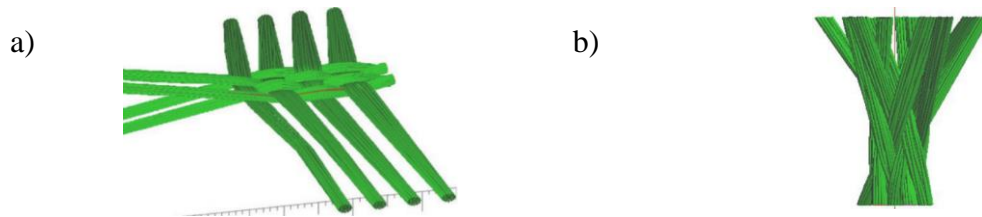


Figure 2.12 Multi-chain digital element models [64]. (a) 2D woven; (b) 3D braid.

In order to reduce simulation time, Miao et al. [62] introduced a static relaxation procedure with a modified contact element formulation. Only 1-2% of the original process' computing time was required using this formulation. The numerical procedure of the static relaxation approach is divided into three steps for a 3D braid (Figure 2.13). In the first step, the guessed fabric structure was produced based on fabric topology using a single digital-chain yarn model. In the second step, each yarn discretized into many digital chains. In the last step, static relaxation, a pre-tensile-strain/stress was incrementally applied on each digital chain of the initial structure to simulate the actual tension effect. Non-equilibrium pre-nodal forces were derived. A global stiffness matrix was assembled to calculate the nodal displacements. The numerical simulation continued until the applied tension is equilibrated and distributed into all yarns and fibers. In each simulation step of the static relaxation approach, the global stiffness matrix had to be solved while it was either singular or ill-conditioned. The processes required to improve the stiffness matrix was detrimental on the convergence rates.

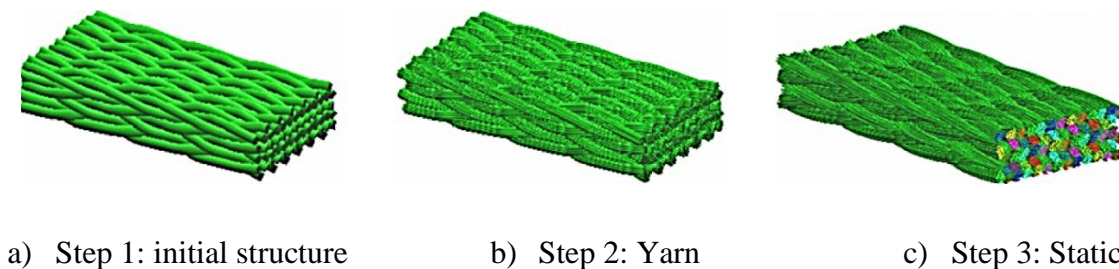


Figure 2.13 Static relaxation procedure for 3D braid fabric [62].

Lejian et al. [61] developed a dynamic digital element approach using a dynamic relaxation procedure. An explicit algorithm with a periodic boundary condition is utilized to compute nodal forces, accelerations, velocities, and displacements. To reduce the computing time, they proposed

an efficient contact search algorithm to recognize the fiber contacts. Moreover, a multi-level dynamic relaxation process requires much less computing time compared to a single level relaxation process was developed. The process is presented at Figure 2.14. In the first step of the numerical procedure, yarn properties and unit-cell topology are defined. In the second step, the digital element mesh is generated by yarn discretization and fiber discretization. In yarn discretization, each yarn is split into multiple digital fibers, and each digital fiber is divided into many rod elements in fiber discretization. Afterwards, the dynamic relaxation loop is ran which itself consists of four sub-steps: applying a predetermined tension to yarns, establishing the periodic boundary zone through a mapping process, searching contacts between fibers/nodes, and calculating nodal forces, accelerations, velocities, displacements and new nodal locations within the unit cell. During the dynamic relaxation process, the calculation is iterated until the nodal velocities vanish. Thus, the potential energy reach a minimum state and the kinetic energy disappears. It should be noted that the kinetic energy is removed by employing damping forces on each node during the simulation. The DFCA software package [75] has been released based on the dynamic relaxation digital element approach.

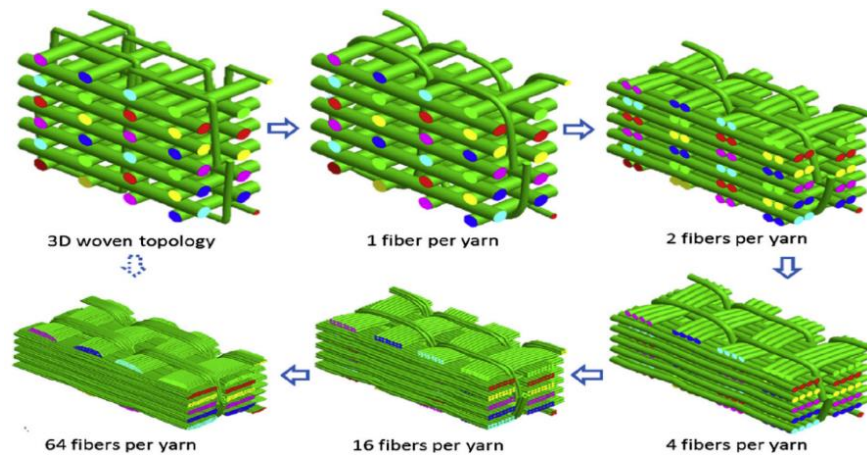


Figure 2.14 Multi-step and multi-level digital element dynamic relaxation [61].

Durville [65-67, 76-80] proposed a finite element approach to simulate fibrous material in which yarns assembled as a bundle of 3D strain beam elements. Durville's works have been focused on the beams/fibers interaction simulation. Contact between fibers are detected using an intermediate geometry defined between two beams' proximity zone. When the intermediate geometry is identified, the contact element is applied on this zone. Solving is made using an implicit algorithm

with the quasi-static procedure. This method has been used to model the mechanical behavior of the entangled fibrous materials [76], 2D woven [65], superconducting cables [78], knot tightening [66], anterior cruciate ligament [79] as well as the fibrous scaffold for ligament tissue [80]. Some of these applications are shown in Figure 2.15.

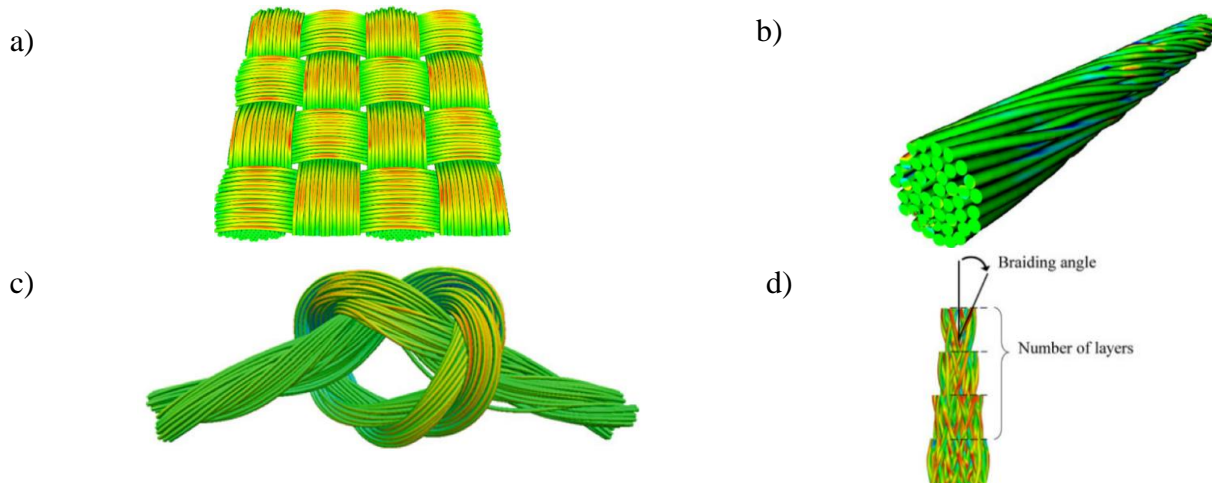


Figure 2.15 Durville's models. (a) 2D Woven [65]; (b) Cable [78]; (c) Knot [66]; and (d) Ligament.

Recently, Vu et al. [81] utilized this method to simulate synthetic braided ropes under tension. In another work [67] they assessed the torsion effect on the braided rope. The method was used to determine the unknown initial configuration of a braided rope. An arbitrary configuration was considered in which yarns inter-penetrated each other and allowed contact–friction interactions to gradually separate these yarns, as shown in Figure 2.16. The treatment of very large initial penetrations and the application of periodic boundary conditions have been adapted with Durville's general approach. The method required considerable computing resources. For example, the computing time to deform a weave structure similar to the one shown at Figure 2.15a was about 45 hours for the bending test and 60 hours for the shear test using a cluster of six processors [77].

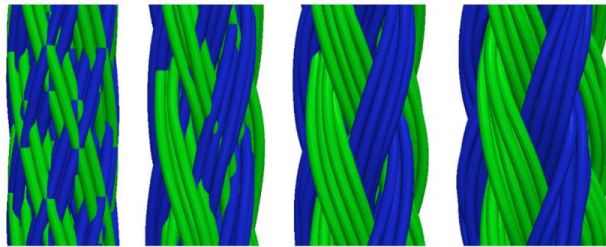


Figure 2.16 Gradual separation of the braided rope yarns in Durville's model [81].

Mahadik and Hallett [68] presented a model of a 3D woven with a layer-to-layer angle interlock structure. Based on the digital element approach, they simulated the yarn as an assembly of 19 fibers in which each fiber was modeled by a chain of beam elements. To reduce the fabric thickness, a thermal load was applied to the fabric yarns followed by compaction between two rigid plates. The model was meshed by the commercial FE software MSC Patran and then solved using LS-Dyna software. In another work, Green et al. [69] modeled a 3D woven built on the method initially introduced by Mahadik and Hallett [68]. To improve the representation of unit cell fabric deformation, they employed a periodic boundary condition. In this work, a Python script read an idealized TexGen unit-cell model to generate the loosely 3D woven with the chains of beam elements mesh as well as the fibers inside the yarns. A thermal load in the form of a temperature drop was applied on the binder yarns to simulate the loosely woven fabric compaction. This model is shown in Figure 2.17. For the sake of reducing the run time of the simulation, the young modulus and yield strength were decreased while increasing the density. However, the computing duration was still high. It was about 9 hours on a high-performance system using eight 2.8 GHz cores.

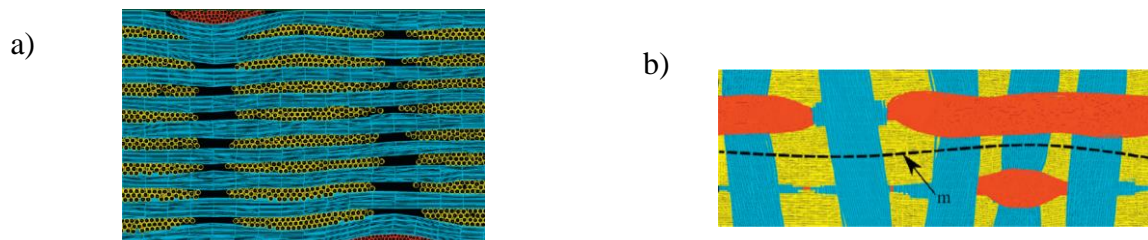


Figure 2.17 3D woven fabric model [69]. (a) Cross-section view; (b) Top view.

Samadi and Robitaille [70] developed a discrete particle-based textiles modeling method. Fibers were modeled as a series of conjoined points. The fibers configurations were determined by a modified Metropolis algorithm [82] with Boolean function [83] and inter-particle strain energy terms. In order to define the textile geometry, the Metropolis algorithm iterated to obtain particle

positions that minimized the strain energy. The strain energy contained the intra-fiber and inter-fiber strain energy. Intra-fiber strain energy included the tension/compression and bending strain energy within a single fiber. Inter-fiber strain energy is associated with the contact between fibers. Figure 2.18 shows a 2D woven fabric under compaction modeled by this method.

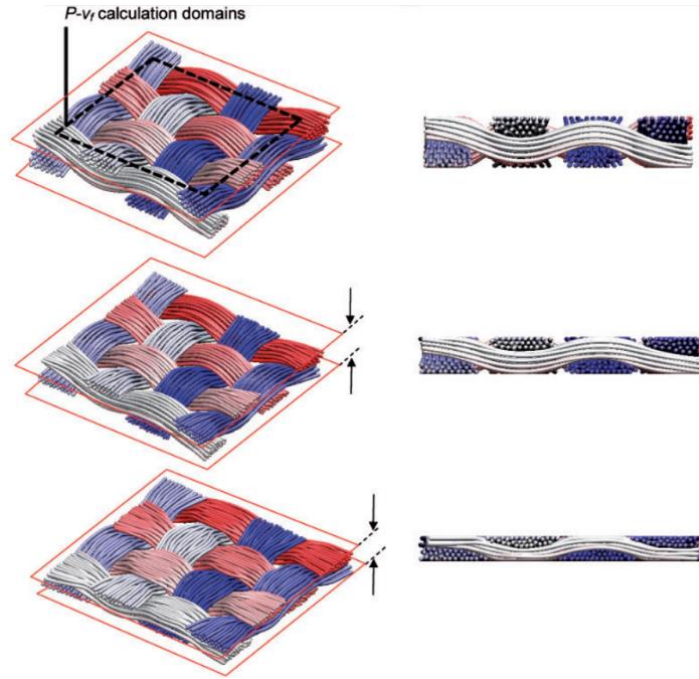


Figure 2.18 2D woven before and after compaction [70].

CHAPTER 3 PROBLEMS IDENTIFICATION, RESEARCH OBJECTIVES AND COHERENCE OF ARTICLES

3.1 Problems' identification

The literature review in Section 2.1 shows that in most studies only triaxial braids have been used as reinforcements in thermoplastic braid-trusion because axial yarns in triaxial braids secure the braid structure subjected to pulling force. The absence of axial yarns in biaxial braids offers an advantage of the high formability of thermoplastic biaxial braid-truded composites after manufacturing through a thermoforming process. However, no research has been found on the use of biaxial braids for thermoplastic braid trusion.

The literature review on 2D braids and simulation of textile reinforcements of composites in Sections 2.2 and 2.3 reveals that few researchers have addressed the problem of braids modeling at fiber-level. We hypothesized that inter-fibers friction plays a significant role in the jamming state phenomenon of braids, while in the literature review, it has not yet been clarified how frictional behavior between fibers affects this phenomenon. Moreover, in the light of surveyed works, it has not yet been established whether the inter-fibers friction impacts the braids' internal geometry, mesoscopic morphology, and crimp of braided yarns. In addition, most fiber-level models have only been qualitatively validated using a comparison with actual images of fabrics such as CT scans. A clear multiscale quantitative validation, including the investigation of the thickness, diameter, and cross-section area of the preform and the yarn has not been reported in reviewed studies.

In the light of reviewed works in Sections 2.1 and 2.2, thermoplastic braid-trusion is a challenging process due to the complex deformation phenomena of the braid inside the pultrusion die and the correct filling of the die by the braided fibers. Hence, a detailed model of the forming process of the braid is a key necessity to understand the complex mechanisms of biaxial braids deformation during braid-trusion. However, most studies in the field of thermoplastic braid-trusion have not proposed a design methodology for the pultrusion of braids, nor have they given specific details about the braid architecture used. Most reported designs of the braid architecture have been followed by the experimental trial-and-error method to achieve a successful braid-trusion.

3.2 Research objectives

Based on the identified problems, the main objective of this research is to develop the manufacturing of thermoplastic biaxial braid-truded composites and simulation the braid-trusion process. The main objective is divided into three specific objectives, which are described in the following sections.

1- To manufacture thermoplastic composite rods using biaxial braid-trusion

To bridge the knowledge gap in the use of biaxial braids in thermoplastic braid-trusion, we evaluated the manufacturing of thermoplastic composite rods using biaxial braids through the braid-trusion process in Chapter 4. A simple geometry-based design is proposed for the thermoplastic biaxial braid-trusion process. This objective assesses the limitations of the proposed design to manufacture thermoplastic braid-truded rods using biaxial braids. Moreover, this research investigates how the manufacturing parameters of spool tension, processing speed, and cooling temperature affect the impregnation, void content, and surface finish of thermoplastic braid-truded composites.

2- To Model fiber-level biaxial braids

To tackle the described shortcomings in the modeling of biaxial braids, we proposed a fiber-level modeling methodology to predict the 3D and internal geometry of biaxial braids in Chapter 5. This objective models diamond (1/1) and regular (2/2) biaxial braids at fiber-level (micron scale) using a quasi-static explicit finite element framework. The model predicts the 3D and internal geometry of biaxial braids during the non-linear large deformation. The model is quantitatively validated using CT scans of dry braided carbon fibers. This objective also explores how the inter-fiber frictional contact and fibers' Young modulus impact the jamming state of braids and the shape of yarns.

3- To Model the forming process of biaxial braids during thermoplastic braid-trusion

To understand the sophisticated braid deformation during thermoplastic braid-trusion, we developed a multiscale modeling methodology to simulate the process in Chapter 6. This objective simulates the forming process of biaxial braids during thermoplastic braid-trusion in an explicit fiber-level finite element framework. This multiscale model considers the

fibers slippages as well as contact between fibers and the die wall. A thermoplastic composite rod is pultruded according to the model. The model thoroughly predicts the macroscopic braid architecture, the mesoscopic internal geometry of the braid, and the microscopic fiber orientation distribution before and after pultrusion. The model also investigates the effect of the contact friction between fibers and the die wall on the braid-trusion process, which discussed in Chapter 7.

3.3 Coherence of articles

Chapters 4, 5, and 6 organize the backbone of this thesis presented here in the form of regular chapter (Chapter 4), published (Chapter 5 and Chapter 6) peer-reviewed journal articles. These chapters cover the main research objective stated in section 3.2.

Chapter 4 is a revised version of a published article [10] in proceedings of ECCM18 - the 18th European conference on composite materials entitled “Thermoplastic composite rod manufacturing using biaxial braid-trusion”. This chapter fulfills the first specific objective, which provides a simple geometry-based design method for manufacturing of carbon fiber/PEI biaxial braid-truded rods. The manufacturing parameters of spool tension, processing speed, and cooling temperature are also scrutinized in this chapter. The limitations of this geometry-based design indicated a requirement for a mechanical-based design that will be developed in the following chapters.

Chapter 5 presents the second article [84] entitled “Fiber-level numerical simulation of biaxial braids for mesoscopic morphology prediction validated by X-ray computed tomography scan” (DOI: [10.1016/j.compositesb.2021.108938](https://doi.org/10.1016/j.compositesb.2021.108938)) published in *Composites Part B: Engineering* (2020 Impact Factor: 9.078). This article meets the second specific objective in section 3.2. The realistic biaxial 1/1 and 2/2 braid models were achieved in which each braided yarn consists of a bundle of discrete virtual fibers. CT scans of carbon fiber braids quantitatively validated the models. The inter-fiber frictional behavior described the jamming state phenomena of braids wherein the frictional dissipation energy quickly grows under tensile loading, while the braid had a stable elongation, diameter, and braid angle. Low fiber-to-fiber coefficient of friction produced lenticular-shaped yarn, while a high coefficient of friction generated an oval-shaped yarn. The increase in the fibers' Young modulus affects neither the jammed state nor the yarn shape. The

fiber-level model established in this article will be developed in the next chapter to simulate the braid deformation during the thermoplastic braid-trusion process.

Chapter 6 presents the third article [85] entitled “Multiscale numerical simulation of the forming process of biaxial braids during thermoplastic braid-trusion: Predicting 3D and internal geometry and fiber orientation distribution” (DOI: [10.1016/j.compositesa.2021.106637](https://doi.org/10.1016/j.compositesa.2021.106637)) published in *Composites Part A: Applied Science and Manufacturing* (2020 Impact Factor: 7.664). The third specific objective was achieved through this article. This article introduced a multiscale numerical simulation methodology to model the forming process of biaxial braids during thermoplastic braid-trusion. The model predicted macroscopic braid architecture, mesoscopic morphology, and microscopic local fiber orientation distribution of thermoplastic biaxial braids before and after pultrusion. It was observed that the local fiber orientations varied along the braid radius, while they were uniformly distributed along the braid pitch. There were also significant differences between the local fiber orientation and the nominal braid angle.

CHAPTER 4 THERMOPLASTIC COMPOSITE ROD MANUFACTURING USING BIAXIAL BRAID-TRUSION ¹

4.1 Introduction

Braid-trusion is a composite manufacturing process combining braiding and pultrusion. This process produces constant cross-sections thermoplastic composite beams having angle-oriented fibers. During pultrusion, the braid is drawn through a series of dies by a pulling device. The braid is therefore solicited under tension.

Braid-trusion is often performed using tri-axial braids containing bias yarns interlaced at a specified braiding angle with axial yarns in the longitudinal direction. Axial yarns secure the braid structure and prevent large longitudinal deformation of the braid under tensile load. However, using the biaxial braids is challengeable since the structure of biaxial braids are more unstable. The biaxial braid can easily elongate/compress under pulling force. In light of the literature survey, no report was found on using biaxial braids for thermoplastic braid-trusion.

This research aims to design and manufacture a thermoplastic composites rod using biaxial braid-trusion. Moreover, this work investigates the effect of the manufacturing parameters on the void content, impregnation, and surface finish of the braid-truded rod. Commingled carbon fibers/PEI yarns are used to make biaxial braids. During pultrusion, braid spool tension of 2.5, 40 and 80 N and puller speed of 50 and 150 mm/min are used to study their effects on the impregnation and void content of the pultruded rods. The experiments are performed for three different cooling die temperatures of PEI's T_g (The glass transition temperature), $T_g/2$ and $T_g/4$. The morphology of the pultruded rod is characterized using microscopy. It is observed that the impregnation, void content and surface finish of thermoplastic braided composite is influenced by the cooling die temperature, braid spool tension, and puller speed. The best results are achieved with a minimum of spool tension, speed, and cooling die temperature.

¹ This chapter is a revised version of the article published in proceedings of ECCM18 – the 18th European conference on composite materials, Athens, Greece, June 2018.

4.2 Methodology

4.2.1 Material

The commingled yarns (Concordia fibers) coated with 1 wt% proprietary sizing used to manufacture the biaxial braid. These yarns are an intimate mix of AS4 carbon fiber (HexTow®) and PEI (Ultem®) as the thermoplastic fibers. Commingled yarns of 30K carbon fibers were wound around the bobbins. Each 30K commingled yarns contained two 12K and two 3K commingled yarn. The carbon fiber in 12K and 3K commingled yarns have 53 and 52 vol.% ratio, respectively. PEI material properties are shown in Table 4.1.

Table 4.1 PEI material properties [86, 87].

Material properties	
Glass transition temperature (T_g)	217 °C
Process Temperature	370-400 °C
Solid specific gravity	1.27
Melt specific gravity	~1.17

4.2.2 Pultrusion apparatus and process

Figure 4.1 exhibits the pultrusion apparatus. The pultrusion apparatus involves a creel, a preheater, four pultrusion dies, a cooling die, and a puller system. The creel was equipped by a magnetic brake (Mitsubishi Powder Brake model ZX-YN) which was controlled using a microcontroller program. To apply a desired tension on the braid spool, the microcontroller varies the current in the magnetic brake and this allows to control the brake torque. Three different tension of ~2.5, 4 and 8 N were applied on the braid spool during the experiment. The braid preform was preheated to a temperature (300 °C) close to the PEI process temperature at the inlet of pultrusion line. The preheater was made of a heating tube that is wrapped by a controlled heater.

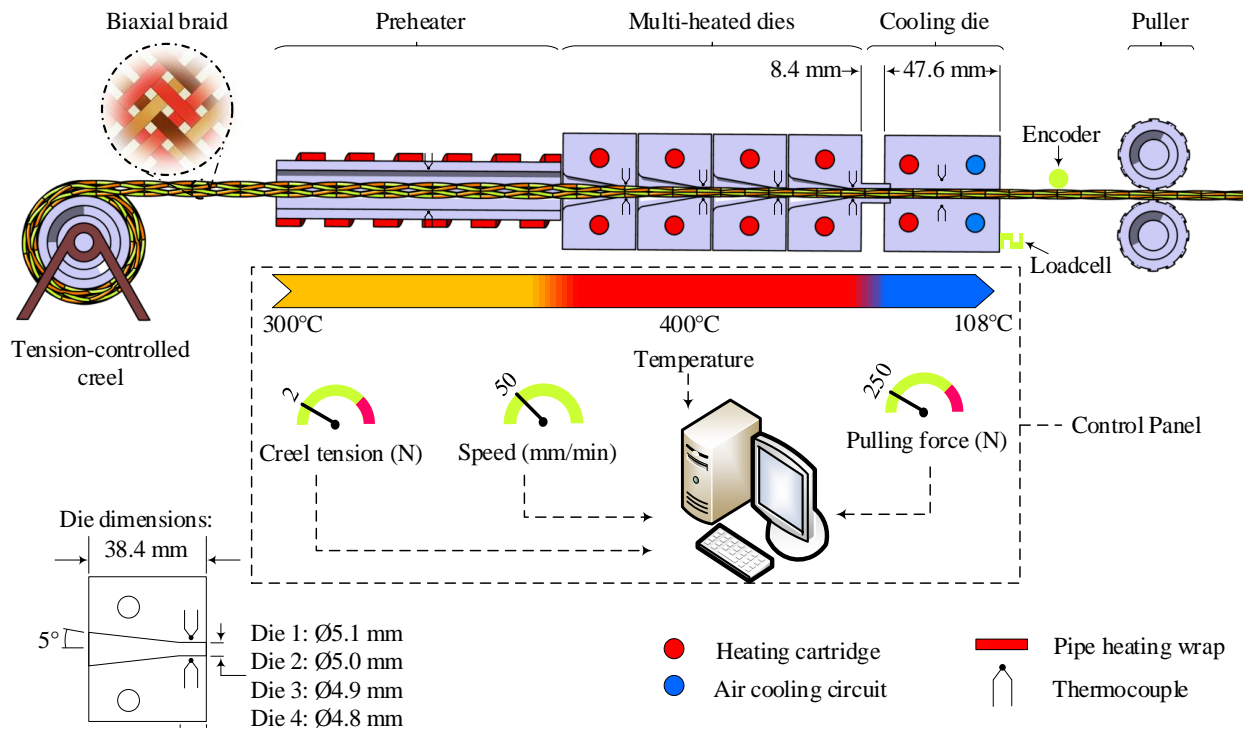


Figure 4.1 Schematic view of the pultrusion apparatus.

The pultrusion dies consisted of four dies which made of contiguous conical and cylindrical zones. The cone angle was 5°. The length of the conical zone was 31.75 mm and the cylindrical zone was 6.68 mm for each die. The diameters (D_i) of the cylindrical zones were 5.1, 5.0, 4.9 and 4.8 mm. The cooling die was placed very close to the last pultrusion die exit. The length of the cooling die was 47.6 mm and its diameter 4.8 mm. Cartridge heaters were embedded in pultrusion dies, heat chambers and cooling die. They were controlled using the feedback from thermocouples (type J). The cooling die was equipped by two air-cooling circuits. All pultrusion dies were set to the constant temperature of 400 °C. The cooling die temperature was set to 215 °C, 107 °C, and 54 °C during the experiment. Finally, the braided carbon/PEI pultruded rod was pulled by a pulling system. To study the effect of pultrusion speed, the braided preform was pultruded at two different speeds of 50 and 150 mm/min. Table 4.2 presents eight manufacturing parameters performed through experiments.

Table 4.2 The manufacturing parameters during experiments.

Parameter	Spool tension (N)	Preheating temperature (°C)	Pultrusion temperature (°C)	Cooling die temperature (°C)	Speed (mm/min)
A	2.5	300	400	215 (T_g)	50
B	40	300	400	215 (T_g)	50
C	80	300	400	215 (T_g)	50
D	80	300	400	215 (T_g)	150
E	40	300	400	215 (T_g)	150
F	2.5	300	400	215 (T_g)	150
G	2.5	300	400	107 ($T_g/2$)	50
H	2.5	300	400	54 ($T_g/4$)	50

4.2.3 Braid and braid-trusion design

Biaxial braid preform was manufactured by a 24-carrier maypole braiding machine. The braiding machine mounted with eight carriers formed a regular pattern (2/2) [20]. The braiding machine setting was adjusted to manufacture a 10 m braid with a 35° braid angle. The braid angle was selected according to unpublished preliminary work. As said in the introduction, overfilling is necessary to create impregnation flow during pultrusion. The overfilling ratio in the i th die ($R_{f,i}$) is expressed by the material area at die entrance over the exit area of the same die ($A_{Die,i}$). The overfilling of the dies can be calculated according to,

$$R_{f,i} = (A_{rb,i-1} + A_{p,i-1}) / A_{Die,i} \quad i = 1, 2, 3, 4 \quad 4-1$$

Where $A_{rb,i-1}$ and $A_{p,i-1}$ are the areas of braided reinforcement fibers and polymer, respectively, located before the i th die, and projected onto the i th die cross-section plane. Note that $i=0$ corresponds to the braided preform before entering the first die. The area of braided reinforcement fibers ($A_{rb,i-1}$) is calculated according to,

$$A_{rb,i-1} = N_Y N_f D_f^2 / 4 \cos \alpha_{i-1} \quad i = 1, 2, 3, 4 \quad 4-2$$

Where N_Y is the number of yarns, D_f is the carbon fiber diameter (7.1 μm for 12K and 6.9 μm for 3K [7]), N_f is the number of fibers in each yarn, and α_i is the braid angle of the braid-truded rod at the i th die exit. Note that N_Y , D_f , and N_f are constant throughout the braid's passage in the dies. The

polymer area at the first die entrance ($A_{p,0}$) can be calculated using the fiber volume content of the commingled yarns with,

$$A_{p,0} = \frac{\rho_s}{\rho_m} \left[A_{rb,0} \frac{(1 - V_{fY})}{V_{fY}} \right] \quad 4-3$$

In Eq. 4-3, V_{fY} is the volume ratio of carbon fiber of commingled yarns, ρ_s is the PEI specific gravity, ρ_m is the PEI melt specific gravity. The differences between the die entrance and exit areas allowed excess resin to overfill. Assuming that the braid is completely impregnated at each dies, the polymer area ($A_{p,i-1}$) entering second, third, and forth dies is the area unoccupied by reinforcing fibers at die $i-1$. It can be calculated according to

$$A_{p,i-1} = A_{Die,i-1} - A_{rb,i-1} \quad i = 2, 3, 4. \quad 4-4$$

Figure 4.2 shows a schematic of a braid opened along the axial direction and subsequently flattened. The two rectangles represent the same braid but with different braid pitches and diameters. The diagonal of the rectangles is the length of the braided yarn (L) for a complete revolution around the braid axis. The vertical dimension is the pitch (P) and the horizontal dimension is the braid outside circumference (πD). The angle between the pitch and diagonal direction is the braid angle (α).

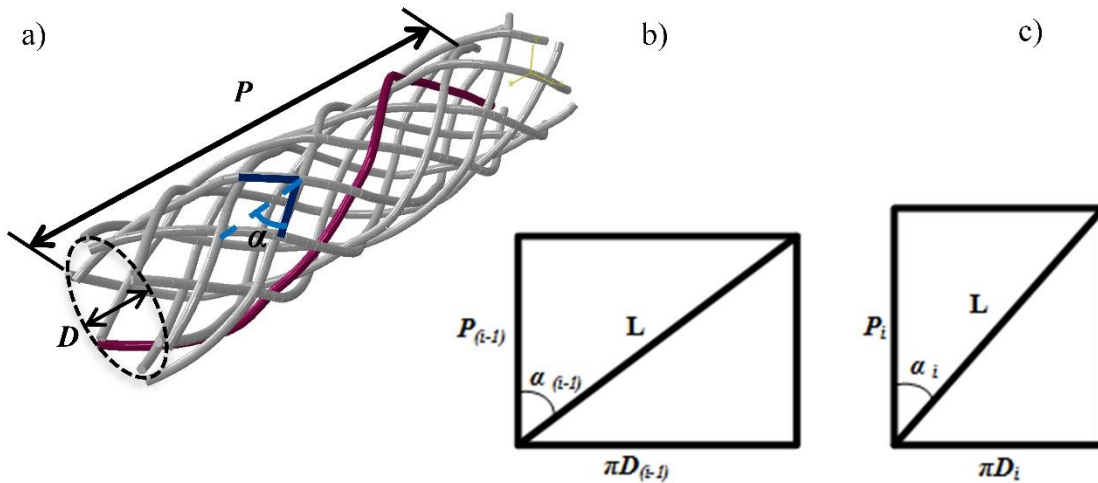


Figure 4.2 Schematic of a cylindrical braid (a) and a flattened braid yarn along a pitch before (b) and after (c) passing through die i ($P_i > P_{i-1}$ and $D_i < D_{i-1}$).

Since the diagonal (L) cannot change when the braid elongates during pultrusion, a reduction on the braid circumference will inevitably result in a reduction of the braid angle and an elongation of the pitch. The initial braid pitch (P_0), diameter (D_0), and braid-truded rod diameter (die diameter, D_i) are known. So the braid pitch (P_i) and braid angle (α_i) of braid-truded rod at i th die exit can be calculated with,

$$P_i = \sqrt{(P_0^2 + \pi D_0^2) - \pi D_i^2} \quad 4-5$$

$$\alpha_i = \tan^{-1} \frac{\pi D_i}{P_i} \quad i = 1, 2, 3, 4 \quad 4-6$$

The braid diameter can be difficult to predict due to its complex structure and unconsolidated state. However, if the yarn's fiber packing ratio (f_r) is considered, the braid diameter can be calculated by,

$$D_0 = 2 \left[\sqrt{\frac{(A_{rb,0} + A_{p,0})}{f_r \pi}} \right] \quad 4-7$$

Finally, the fiber volume fraction ($V_{f,i}$) of the braid-truded rod at i th die exit is obtained by,

$$V_{f,i} = (N_Y \pi D_f^2 N_f) / (4A_{Die,i} \cos \alpha_i) \quad i = 1, 2, 3, 4 \quad 4-8$$

According to an initial braid angle α_0 of 35° and Eqs. 4-1 - 4-7 the braid-truded rod fiber volume fraction, braid angle, braid pitch and the overfilling ratio at each exit die are listed in Table 4.3.

Table 4.3 Designed braid pitch, braid angle, fiber volume fraction, and the overfilling ratio at dies' exit

	Preform	1 st Die	2 nd Die	3 rd Die	4 th Die
Braid Diameter	6.23	5.2	5.00	4.90	4.80
Braid pitch	28.2	30.31	30.64	30.80	30.95
Braid angle	35	28.33	27.14	26.56	25.98
V_f	0.37	0.50	0.54	0.56	0.58
R_f	n/a	99.03	105.95	103.80	110.0

According to Table 4.3, the braid pitch and fiber volume content increase, and the braid angle decrease due to the reduction of braid diameter (die diameter).

The braid pitch was measured before and after pultrusion. The braid pitch and diameter were measured by a caliper on the braid preform and braid-truded rod at every 10 cm. The braid-truded samples were prepared from the manufactured rods for microscopic observation. The samples were mounted in epoxy and then polished to obtain the cross-section images using an optical microscope (Metallovert, Leitz).

4.3 Results

4.3.1 Braid geometry measurements

Table 4.4 presents the averaged measurements for both the geometries of the braid preform before pultrusion and braid-truded rod after pultrusion. The nominal braid angle was identical to the designed value from Table 4.3. However, the measured pitch length and braid angle are significantly different from the designed values of Table 4.3. These differences between actual and predicted values indicated that the proposed geometry-based design is not able to determine the braid geometry accurately. The geometry-based design does not take into account the mechanics of braid such as fiber-to-fiber contacts and fiber tension. To address the issues of the geometry-based design, a mechanical model should be developed for the braid-trusion process.

Table 4.4 Measurement on the braid preform before pultrusion and braid-truded rod after pultrusion.

	Braid pitch (mm)	Braid diameter (mm)	Braid angle
Braid preform	32.7 ± 0.8	7.3 ± 0.1	$35.2^\circ \pm 0.7$
Braid-truded rod	36.4 ± 0.5	4.7 ± 0.01	$22.15^\circ \pm 0.3$

As expected, the braid pitch increased by passing through the pultrusion dies. The braid angles (α) were calculated using the measured pitch (P) and diameter (D) via the Eq. 4-6. The braid angle of braid-truded rod decreased by 37% and the braid pitch elongated by 11% after pultrusion. It can be explained that the thermoplastic fibers melt and the braided carbon fibers become loose during pultrusion. At this moment, the dies compact the braid and the tensile load elongates the braid pitch.

4.3.2 Parametric studies

The liquefaction of the PEI started in the first pultrusion die. The composite impregnation is performed by passing through the four dies. Figure 4.3 illustrates a cross-section microscopy at 200 \times of a portion of the manufactured rod. Whilst the white circles are indicative of the carbon fibers, the gray-colored regions are the matrix and the black areas represent the voids.

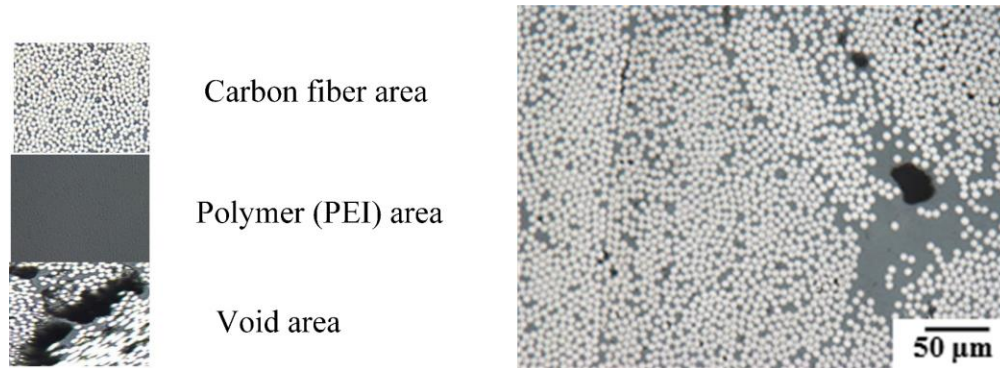


Figure 4.3 Microscopy image at 200 \times .

4.3.2.1 Spool tension

Figure 4.4 shows the entire cross-section of the composite rod with three different spool tension of 2.5, 40 and 80 N with speed of 50 mm/min and the cooling temperature of 200 °C (Parameter A-C). The fibers are well distributed throughout the cross-section. Resin rich regions can be observed in both along the yarn boundaries (Figure 4.4a-b) and the center of the braid-truded rod (Figure 4.4 c). It can be seen that the void content increases when increasing the spool tension. This can be an indication that raising the spool tension condenses the carbon fiber bundles and reduces their permeability. The same behavior is also observed in Lapointe *et al.* [88] for the carbon/PEEK unidirectional yarns pultrusion. One can conclude that spool tension has a significant effect on the impregnation of thermoplastic braid-truded composites.

4.3.2.2 Pultrusion speed

Figure 4.5 exhibits two distinct cross-sections of the composite rod manufactured with two different speeds of 50 and 150 mm/min with the same spool tension (Parameter A and F). These figures show a slightly higher amount of voids for the 150 mm/min braid-trusion. This indicates that the resin flow time was too short to allow impregnation of fiber bundles. It can also be observed

that the smooth surface of the rod is roughed in the high-speed case. At high-speed, it is suspected that the hot material at the heating die exit does not cool significantly. Therefore, the hot molten thermoplastic materials has less time to deconsolidate. This phenomenon can rough the surface of the braid-truded rod at high-speed.

4.3.2.3 Cooling die temperature

The influence of cooling die temperature on the braid-truded rod is shown in Figure 4.6. The results are presented for three different cooling die temperatures of the glass transition temperature ($T_g = 215^\circ\text{C}$) (Figure 4.6a), $T_g/2 = 107^\circ\text{C}$ (Figure 4.6b), and $T_g/4 = 54^\circ\text{C}$ (Figure 4.6c) with the same speed of 50 mm/min and the minimum spool tension (Parameter A, G and H).

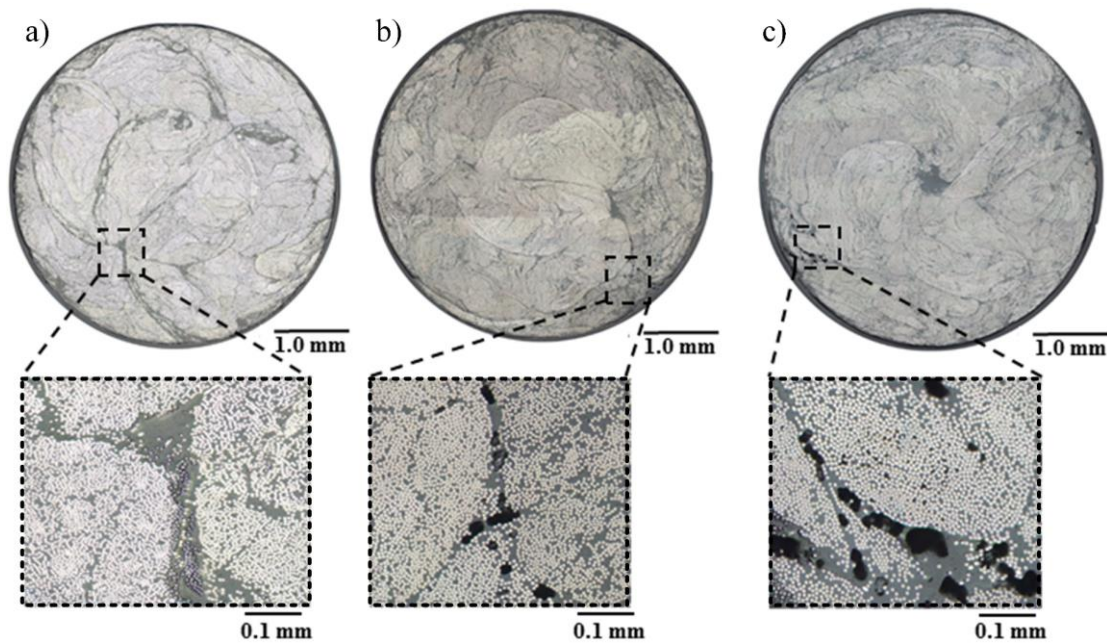


Figure 4.4 The effect of spool tension on the composite rod. The cross-section of the manufactured rod with the spool tension of 2.5 N (a), 40 N (b) and 80 N (c).

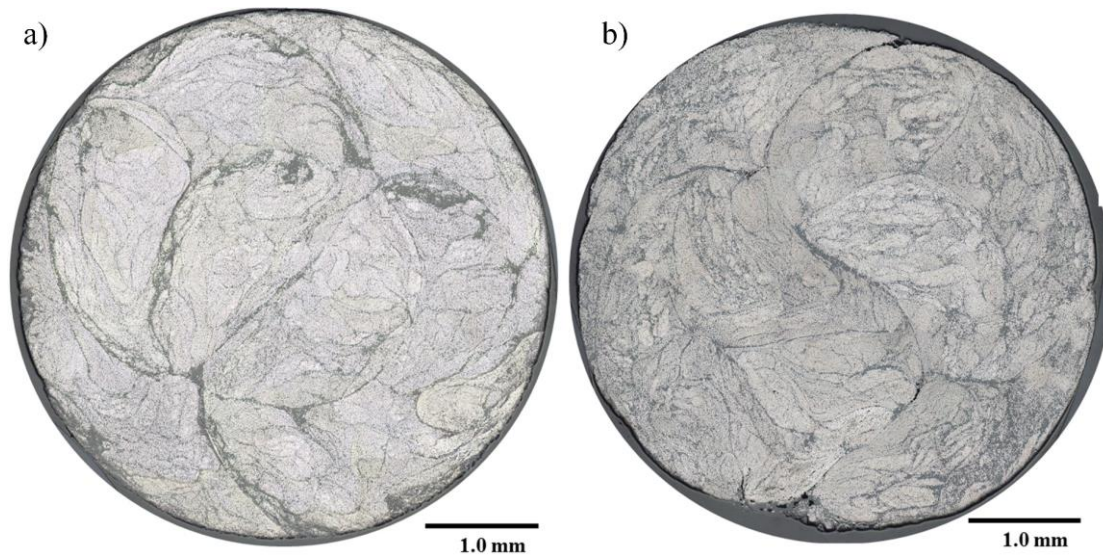


Figure 4.5 The effect of speed on the composite rod. The cross-section of the braid-truded rod with 50 mm/min (a) and 150 mm/min (b).

It is seen in Figure 4.6a that surface finish at top and bottom of the image was irregular for the sample with cooling die temperature of T_g . Reducing the cooling die temperature to $T_g/2$ (Figure 4.6b) or $T_g/4$ (Figure 4.6c) resulted in a higher quality of the surface finish. This could be explained by faster cooling and therefore greater and faster shrinkage of the rod in the cooling die. The rod shrunk and debonded faster from the cooling die surface at the low cooling die temperature. There was no significant difference observed between the rod's surface finish with the cooling die temperature of $T_g/2$ and $T_g/4$.

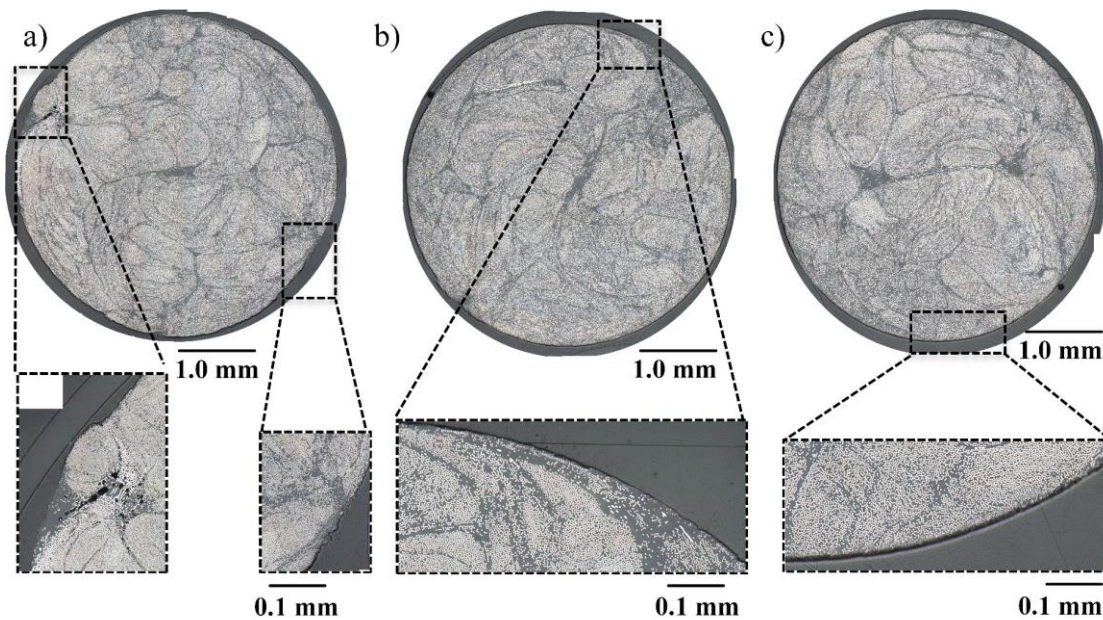


Figure 4.6 The cross-section of the braid-truded rod with the cooling temperature of (a) T_g , (b) $T_g/2$ and (c) $T_g/4$.

4.4 Conclusion

A thermoplastic braid-truded rod was manufactured using the biaxial braid. The commingled carbon/PEI fibers were used to manufacture the braid with 35° nominal braid angle. The biaxial braid was then pultruded using the multi-die pultrusion apparatus. The braid pitch and diameter was measured both before and after the pultrusion. During pultrusion, the preheater and pultrusion die temperatures were set at 300°C and 400°C , respectively. The spool tension, cooling die temperature, and speed were changed to evaluate their effect on the thermoplastic composite rod. The samples of the manufactured rod were prepared to characterize their morphology using the optical microscopy. It is found that these manufacturing parameters affect the thermoplastic composite rod and their effects can be summarized as,

- The braid angle of braid-truded rod decreased by 37% after pultrusion due to the dies compacting the braid and tensile load elongating the braid pitch.
- The void content raised slightly when the spool tension increased. Boosting the spool tension reduced the carbon fiber bundles permeability.

- The void regions grew with accelerating the process from 50 to 150 mm/min. The reason is that the resin flow time was too short to completely penetrate carbon fiber bundles.
- The manufactured rod with the high-speed process had a rougher surface finish.
- The high-quality surface finish was achieved when the cooling die temperature dropped from T_g to $T_g/2$, and pultruding at 50 mm/min. It is suspected that the rod shrunk and debonded faster from the cooling die surface at the low cooling die temperature.

In future chapters, a finite element model will simulate biaxial braids' deformation during pultrusion to obtain a more accurate prediction of the braid-truded rod geometry. Finally, due to the lack of the results for the thermoplastic biaxial braid-trusion in the open literature, the obtained results could be used as a benchmark for the future works.

**CHAPTER 5 ARTICLE 1: FIBER-LEVEL NUMERICAL SIMULATION
OF BIAXIAL BRAIDS FOR MESOSCOPIC MORPHOLOGY
PREDICTION VALIDATED BY X-RAY COMPUTED TOMOGRAPHY
SCAN**

Mohammad Ghaedsharaf ^a, Jean-Evrard Brunel ^b, Louis Laberge Lebel ^a

*^a Advanced Composite and Fiber Structure laboratory, Research Center for High Performance
Polymer and Composite Systems, Department of Mechanical Engineering, Polytechnique
Montréal, 2900 boul. Édouard-Montpetit, University of Montréal Campus, Montréal, H3T 1J4,
Canada*

^b Bombardier Aerospace, 1800 boul. Marcel-Laurin, Saint-Laurent, H4R 1K2, Canada

This article was published in *Composites Part B: Engineering*, Vol. 218, 1 August 2021, 108938

Highlights

- Fiber-level modeling methodology is proposed to predict the mesoscopic morphology of 1/1 and 2/2 biaxial braids.
- Braid diameter and yarn cross-section area are predicted with an average accuracy over 98%.
- Varying the fiber-to-fiber coefficient of friction has negligible impact on the braid jammed state angle.
- Low fiber-to-fiber coefficient of friction produces lenticular shaped yarn, while a high one produces an oval shaped yarn.
- Increasing the fibers' Young modulus impacts neither jammed state nor the yarn shape.

Abstract

This paper proposes a modeling methodology to predict the 3D and internal geometry of biaxial braids. Inspired by the digital element approach, braided yarns are modeled as a bundle of virtual fibers. Here we adopt truss elements to a virtual fiber with actual material properties instead of beam elements that have limitations due to the beam flexural rigidity. The mesoscopic morphology prediction of two common braid patterns of the diamond (1/1) and regular (2/2) are validated by a comprehensive quantitative comparison with X-ray micro-computed tomography (CT) scans of braided carbon fibers. We find that the fiber-level frictional behavior is able to explain the jammed state of braids wherein the frictional dissipation energy quickly grows, while the braid has a stable elongation, diameter, and braid angle. Parametric studies illustrate how the increase in the coefficient of friction affects the yarn cross-sectional shape, whereas it has an insignificant effect on the crimp and jammed state of braids. Models also reveal that changing a wide range of the fiber modulus of elasticity hardly impacts the mesoscopic morphology and crimp of the braids.

Keywords: A. Fibers, C. Finite element analysis (FEA), E. Braiding, Micro-computed tomography (CT) scan, Digital element approach (DEA)

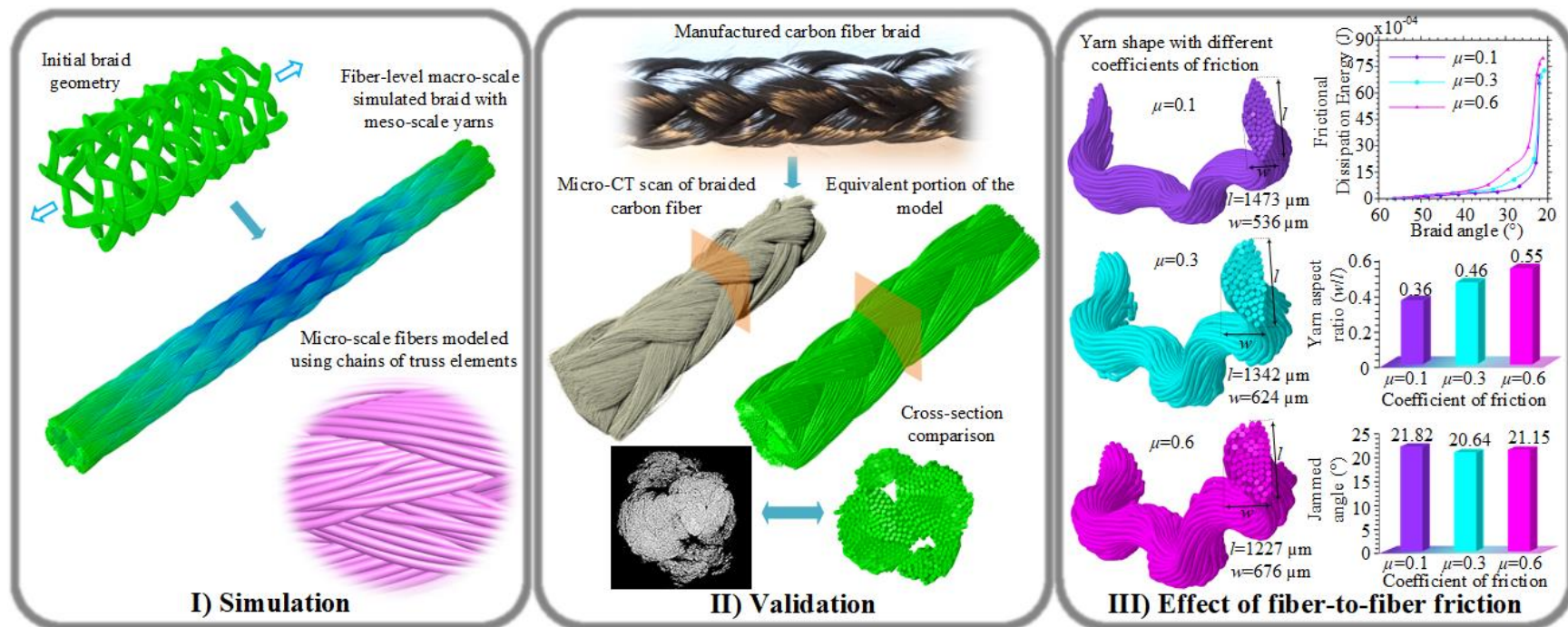


Figure 5.1 Graphical abstract

5.1 Introduction

Braids are long-established fabrics that today have engaged in modern applications. They provide impressive mechanical properties due to their oriented fibers [89, 90]. Braids also have high formability into complex shapes [21, 91]. Furthermore, braiding has a high-level of automation [19, 92]. As a result of these advantages, braids have become of great interest in composite manufacturing [10, 12, 13]. Since the application of braided-reinforced composites are growing, modeling tools are required to design and predict the braid geometry and mechanical behavior.

Modeling the 3D geometry of braids is a challenging task because of the complex architecture, inherently multiscale, discrete nature, and complicated friction interactions between discrete constitutive components. Figure 5.2 illustrates a schematic of multiscale modeling framework. The macro-scale biaxial braid (Figure 5.2a) is composed of discrete meso-sized yarns (Figure 5.2b) that are crossing over and under each other in a helix path along the braid axis. The yarns themselves are composed of discrete micron-sized fibers grouped together that are the smallest constitutive components of a fabric (Figure 5.2c).

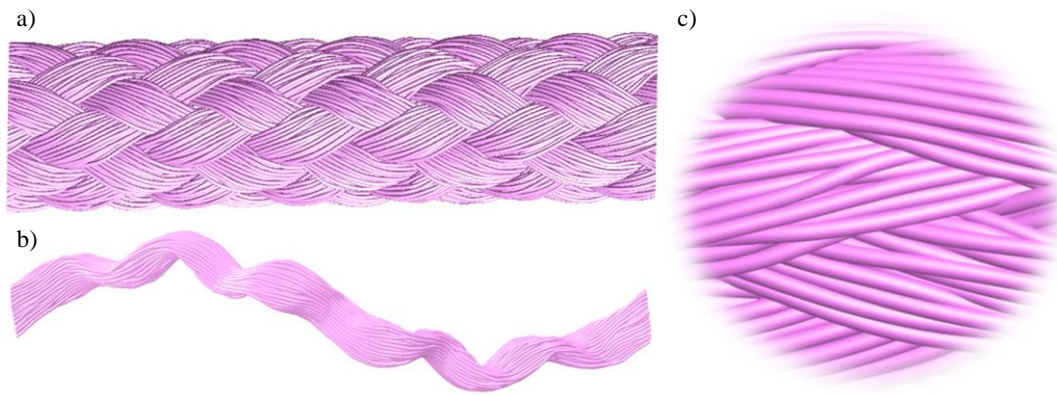


Figure 5.2 Multiscale modeling framework for a biaxial braid. (a) Macro-scale braid with multifilament yarns. (b) Individual meso-scale multifilament yarn. (c) Individual micro-scale fibers modeled using chains of truss elements (one chain by fiber).

Given the discrete nature of these fibrous materials, two discrete modeling approaches have been used to simulate these reinforcements of composites: the yarn-level (i.e. meso-scale) [56-59, 68, 93-95] and the fiber-level (i.e. micro-scale) [61, 62, 64, 66, 68, 70, 81, 96] approach. The yarn-level models usually contain a representative unit cell in which the yarns were considered as a solid continuum model [56-59, 93-95]. Since the nature of the yarn is discrete, meso-level models require

specific behavior to take into account the fibrous nature of the yarn [57, 58, 94]. In addition, in this approach, the yarn cross-section shape is usually simplified as elliptical or lenticular that often does not represent reality. On the other hand, fiber-level approaches provide a realistic simulation that can well describe the reality of fabrics [61, 62, 64, 66, 68, 70, 81, 96]. This approach allows simulating the fiber-to-fiber slippages and interactions inside a yarn as well as among yarns. Digital Element Approach (DEA) has been introduced as a powerful method to model the geometry of fabrics at the fiber-level [61, 62, 64]. In this concept, each yarn was discretized into a bundle of fibers and each individual fiber was made of a chain of truss (rod) elements. A contact algorithm detected the contact between fibers. Based on the DEA, several works were conducted on 2D and 3D fabrics. Mahadik and Hallett [68] presented a model of a 3D woven structure with layer-to-layer angle interlock structure. The yarn was simulated as an assembly of 19 fibers in which each fiber was modeled by a chain of beam elements. In another work, Green et al. [69] modeled a 3D woven structure based on the method initially introduced by Mahadik and Hallett [68] using beam elements. Durville [66] proposed a finite element approach to simulate fibrous material in which yarns were assembled as a bundle of 3D strain beam elements with a focus on the beams interaction. The large deformation of the fabric was simulated within an implicit solver using the quasi-static procedure. Vu et al. [81] simulated the tensile test of a braided synthetic rope for offshore industry application using Durville's method. Daelemans et al. [96] modeled a dry 3D woven structure to investigate the mechanical behavior.

DEA can model a fiber as a chain of beam [66, 68, 69, 81, 97] or truss [61, 96] elements. The 3D Timoshenko beam element has been used at the beginning of the work [97], however, the virtual fiber made of beam elements has a large bending and torsional stiffness compared to the actual carbon fiber. The bending (K_b) (Eq. (5-1)) and torsional stiffness (K_t) (Eq. (5-2)) of a cylindrical rod (an element) are directly proportional to the modulus of elasticity (E_f) and rigidity (G_f), respectively, and forth power of fiber's diameter (D_f).

$$K_b = \pi E_f D_f^4 / 64 \quad (5-1)$$

$$K_t = \pi G_f D_f^4 / 32 \quad (5-2)$$

Since the modeling of the actual yarn with a large number of fibers (e.g. 12,000 fibers) was unachievable due to the computational cost, the yarn was discretized in much fewer virtual fibers. Therefore, the diameter of the virtual fiber became much larger than that of the actual one. When the diameter of the fiber increases, the bending and torsional stiffness grow with the power of four. A few techniques have been used to tailor beam elements to reduce the flexural stiffness of the virtual fiber, including the decrease of the modulus of elasticity, using an elastic perfectly plastic material [69], and using a correction factor for the moment of inertia [81]. Nevertheless, as a result of the large bending and torsional stiffness, the beam elements with the actual mechanical properties are an inappropriate choice for constructing the virtual fiber. To tackle this problem, truss elements were used to model braided fibers as these elements carry no moments and forces perpendicular to the element axis and only can transmit axial forces [98].

The structure of biaxial braids is very unstable. Biaxial braids can easily elongate under low tensile loading. However, the braid elongation reaches a stable point wherein the yarn movement is no longer allowed. This phenomenon has been called the jammed state [20]. The jammed state phenomenon has been studied from different aspects, including geometric behavior, deformation status, and stress-strain state [20]. We believe that there is evidence to support a hypothesis that the frictional behavior between fibers plays an important role in this phenomenon, although no research has been found in the surveyed works.

Most fiber-level models have only been qualitatively validated using a comparison with actual images of fabrics such as microscopic, scanning electron microscope, and micro CT images [61, 62, 96]. A clear multiscale quantitative validation, including the investigation of the thickness, diameter, and cross-section area of the fabric and the yarn has not been reported in reviewed studies.

This paper presents a modeling methodology to determine the macroscopic and mesoscopic geometry of dry biaxial braids. The braided yarn was simulated as a bundle of individual fibers using truss elements. An explicit quasi-static finite element framework handled the braid's large deformation and fiber-to-fiber contact. Periodic boundary conditions (PBCs) were assigned to organize the ends of braid during deformation. Convergence studies determined how many fibers

in each yarn and how many elements in each fiber are required to achieve stable numerical results. The proposed models predicted the geometry configuration of two more common braid patterns, namely diamond (1/1) and regular (2/2). We provided further support for the validation of the model using a multiscale quantitative comparison of braid's diameter and the area of yarn cross-section with micro-CT images of the braided carbon fibers. To confirm the hypothesis that the frictional behavior between fibers significantly contributes to the jammed state phenomenon of braids, we explored the relationship between the frictional dissipated energy of braids and the jammed state phenomenon. The parametric studies demonstrated how the coefficient of friction and modulus of elasticity of fibers impact the simulation.

5.2 Modeling methodology

The general overview of the modeling workflow is displayed in Figure 5.3. The process contains the following steps:

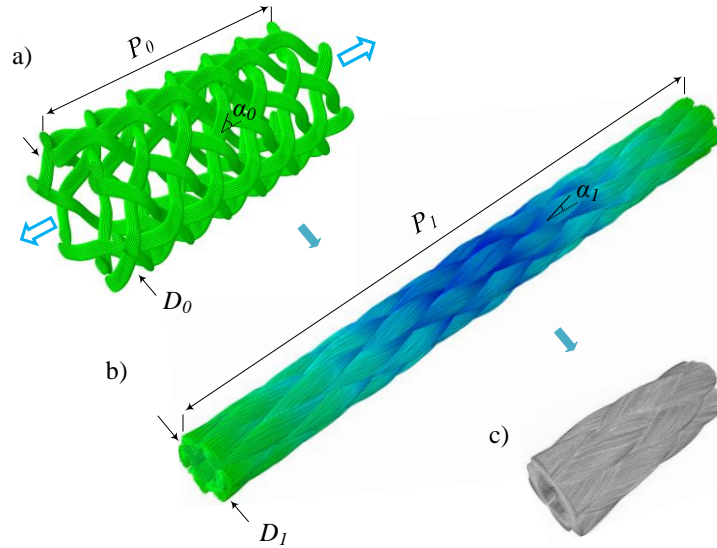


Figure 5.3 General overview of the modeling workflow. (a) A Python script generated the initial braid geometry in Abaqus FEA software. (b) Realistic braid geometry after the application of small loading on the initial braid geometry's end. (c) Validation of the methodology using micro-CT scan data (P_i : braid pitch, D_i : braid diameter, α_i : braid angle ($i=0, 1$), $P_0 < P_1$, $D_0 > D_1$, $\alpha_0 > \alpha_1$).

- I. A Python script created an initial braid geometry in the finite element analysis software Abaqus 6.18 with loose yarns in which each yarn is modeled as a bundle of virtual fibers (Figure 5.3a). The Python script automated the model generation and boundary conditions assignment.
- II. In order to obtain a realistic braid geometry, the simulation was conducted by the application of small loads on the initial braid geometry (Figure 5.3b). The model was solved using the Abaqus/Explicit solver. This solver is well suited to handle the complex contact between fibers and the highly nonlinear deformation.
- III. The methodology was validated using X-ray micro-CT scans of two common patterns of diamond and regular braided carbon fiber (Figure 5.3c).

The steps above are explained in detail in the following subsections.

5.2.1 Yarn discretization and mesh generation

The Python script automatically generated a loose braid geometry with input parameters of a pitch length (P_0), diameter (D_0), and the number of yarns (N_y) (Figure 5.3a). Figure 5.4a, b illustrate the yarn discretization. A circle-packing algorithm discretized the yarn into fibers with concentric layers ($L_n, n = 0, 1, \dots$), which its core (L_0) had one fiber (Figure 5.4b). The number of fibers in each layer was obtained by Eq. (5-3) and the total number of fibers in the yarn was calculated by Eq. (5-4).

$$N_{fL_n} = 6n \quad (5-3)$$

$$N_f = \left(\sum_{n=1}^{n=L_n} 6n \right) + 1 \quad (5-4)$$

The total area of fibers in a yarn section was determined by,

$$A_f = Y/\rho \quad (5-5)$$

where Y is the yarn's linear density (tex (g/Km)) and ρ is the fiber material density (g/cm³). The diameter of a virtual fiber was achieved by.

$$\Phi = \sqrt{4A_f / \pi N_f} \quad (5-6)$$

A small gap ($Gap_{fiber} = \Phi/3$) between fibers ensured that there was no initial penetration between fibers (Figure 5.4b). Figure 5.4c illustrates a virtual fiber made of a chain of truss elements. The truss element is a two-node member in which nodes allow only translational motions, i.e., they have three degrees of freedom. To simulate the flexibility of fibers, the end-to-end connected nodes are sharing their translational degrees of freedom. Each fiber was constructed using T3D2 truss elements.

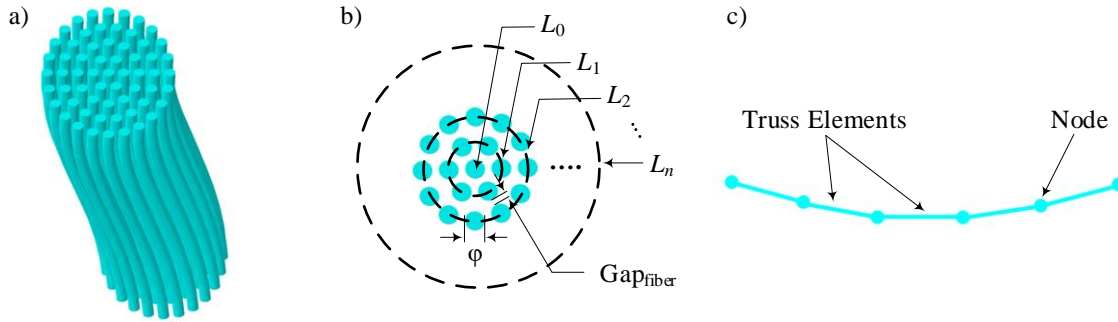


Figure 5.4 Yarn discretization by fibers. (b) Yarn cross-section showing fibers located in concentric layers with an initial gap between fibers (Gap_{fibres}). L_n is the n th layer. The core (L_0) has one fiber. Number of fibers in each layer: $N_{fL} = 6n$ ($n=1, 2, \dots, L_n$). Number of total fibers: $N_f = (\sum_{n=1}^{n=L_n} 6n) + 1$. The (c) Constitutive components of a fiber: truss elements connected with three degrees of freedom node (translational motions).

5.2.2 Contact detection

The general contact algorithm of Abaqus/Explicit was used to detect the contact between fibers. The general contact allows detecting many contact regions automatically and it is appropriate for fiber-to-fiber contacts. Penalty friction formulation defined for the contact mechanical tangential

behavior. A coefficient of friction of 0.3 was used, which has been proposed for carbon yarn interaction of braiding [99]. To minimize the penetration between touching fibers, the hard contact is used in the pressure-overclosure relationship for the contact mechanical normal behavior.

5.2.3 Periodic boundary conditions (PBCs)

The braid was modeled along one pitch, i.e. the distance required along the braid axis for one yarn to complete a full convolution. PBCs were prescribed on this single braid pitch as part of an infinite braid. This allows to limit the computation cost while still providing a periodic architecture without boundary effects. A dummy node was defined for implementation in PBCs, which was not attached to any other part of the model. The PBCs were prescribed in the transverse direction (x- and y-directions) through linear constraint equations defined as,

$$u_i^{Left} - u_i^{Right} + u_i^{DN} = 0, \quad u_i^{DN} = 0, \quad \text{with } i = x \text{ or } y \quad (5-7)$$

where u is nodal displacement, subscript i denotes the degree of freedom in x - and y -directions, superscripts of DN , $Left$, and $Right$ refer to dummy node and boundary nodes at the left and right side of the braid's end, respectively. The displacement of the dummy node (u_i^{DN}) is set to zero on both directions of x and y . This equation effectively equalized the transverse displacements of all corresponding nodes at braid ends. The motion of the end nodes at z -direction (i.e. axial direction) was driven by the application of forces along this direction.

5.2.4 Loading strategy

A small axial tension of 1N was smoothly applied to both ends of the loose braid within a quasi-static framework. In this framework, immediate loading may lead to the propagation of a stress wave through fibers and generate noisy and inaccurate results. This unfavorable effect was removed by ramping up the loading smoothly from zero to the maximum value. The smooth loading was assigned by an amplitude curve. An example of this smooth step amplitude curve can be seen in the Appendix A. During the loading, the fibers reoriented and slipped on each other to shape the realistic yarn cross-sections. This loading was applied to achieve the jammed state when the fiber deformation stops.

5.3 Experimental methods

To validate the modeling methodology, two biaxial braid patterns of diamond and regular were fabricated. Then, specimens were cut to characterize the internal braid structure using X-ray micro-CT scanning.

5.3.1 Braid fabrication

High strength 12k carbon fiber (TANSOME[®], Hyosung Advanced Materials) was used to manufacture the braid. The material properties of carbon fibers [100] are listed in Table 5.1.

Table 5.1 Material properties of carbon yarn [99, 100].

Density (g/cm ³)	1.80
Number of fibers per yarn	12,000
Yield (g/Km)	800
Modulus of elasticity (GPa)	250
Coefficient of friction	0.3

A 24-carrier braiding machine (KBL-24-1-110, Xuzhou Henghui Braiding Machine Co., Ltd.) produced both braid patterns. Both braid patterns were manufactured without mandrel or core. During braiding, the braids were pulled by the pulling mechanism. This caused the braid pitch to extend, the braid diameter to shrink, and yarns to rotate to a lower braid angle. This deformation stabilized when the yarns jammed together. The diamond braid pattern was manufactured using 12 bobbins mounted on the braiding machine, six rotating clockwise and six rotating counterclockwise. The carrier rotation speed was 8 RPM (0.133 RPS) and the take-up speed was 4.54 mm/s. The resulting braid pitch length was 34 mm. The regular braid pattern was manufactured using eight bobbins, four rotating clockwise and four rotating counterclockwise. The carrier rotation speed was 8 RPM and the take-up speed was 1.82 mm/s. The resulting pitch length was 13.6 mm. For both braid patterns, the obtained braid diameters were measured using the CT scans (see Section 3.3). The nominal braid angle was calculated using the resulting pitch length (P) and the measured diameter (D) according to Eq. (5-8).

$$\alpha_{nominal} = \tan^{-1}(\pi D/P) \quad (5-8)$$

The images of both braided carbon fibers are provided in the Appendix B.

5.3.2 X-ray micro-computed tomography (micro-CT)

Both braid pattern specimens were scanned using an X-ray CT system (XT H 225, Nikon). A fixture was designed to hold the specimen in the CT machine. The details of braids' holding fixture are provided in the Appendix B. The radiographs were acquired with a voxel size of 6.5 μm , a beam energy of 110 kV and a current of 60 μA . The radiographs were reconstructed using the CT PRO 3D software (Nikon) to generate a 3D view of both specimens. The image threshold was set at the beginning of image processing to extract the volume of interest from the whole volume. The whole volume contained a gray value distribution of the air (voids), fixture, and braided carbon fibers. The braided carbon fibers and voids were distinguished by thresholding the grayscale values. To tune the threshold of grayscale values, the grayscale values were set in the range of 8800-10070 from the whole range of 0-65535 using the histogram tool in the Dragonfly software.

5.3.3 Quantitative analysis method

The cross-sectional diameter of the braided patterns and the cross-sectional area of the braided yarns were quantified for both the model and CT slices, while other variables were only calculated for the model. Dragonfly software version 4.1 (Object Research Systems (ORS) Inc.) was used for the quantitative analysis of the CT images. Two slices were selected from each sample for the quantitative analysis and comparison with the equivalent cross-sections of the model. The braid diameter of each slice was averaged by measurement of the diameter at every 45 degrees (eight measurements for each section). The area of yarn cross-section was also averaged by measurement of all yarns cross-sectional area for each section.

The fiber-level braid model provided access to the local fiber angle. The braid angle was obtained by averaging the local orientation of all fiber elements in the braid model. To calculate the local orientation of an element, it was assumed that the element was the Euclidean vector of \vec{V} in space in which the orientation with respect to the braid axis (Z-axis) was obtained by the direction cosine:

$$\alpha_{element} = \cos^{-1}(V_z/\|V\|) \quad (5-9)$$

The local fiber angle calculated by Eq. (9) was affected by both the in-plane braid angle and the out-of-plane crimp angle. However, averaging the local fiber angles of all elements eliminates the crimp's impact on the braid angle. The braid elongation was calculated by Eq. (5-10) where P is the pitch length.

$$\bar{\epsilon} = (P - P_0)/P_0 \times 100 \quad (5-10)$$

During deformation, the radius (r) of each nodal point could be calculated by node's coordinates in a cylindrical coordinate system using Eq. (5-11). The radius of the braid varied along the thickness of the braid; therefore, the averaged radius was considered on the deformation history. The dimensionless diameter (\bar{D}) was achieved by Eq. (5-12), where the variable of D_0 is the initial averaged diameter.

$$r = \sqrt{x^2 + y^2} \quad (5-11)$$

$$\bar{D} = 2r/D_0 \quad (5-12)$$

To describe the yarn cross-section transition shape from the circular to the lenticular, a ratio of the minor diameter (w) to the major diameter (l) was defined as the yarn aspect ratio (flattening ratio, δ).

$$\delta = w/l, \quad 0 < \delta \leq 1 \quad (5-13)$$

This ratio can also be a criterion to measure the compression level of the yarn.

The percentage of local crimp (fibers crimp) was calculated as,

$$crimp = ((L/P) - 1) \times 100 \quad (5-14)$$

where L is the fiber's length, which was calculated as the sum of the constituent elements' length (L_i^e) of the fiber.

$$L = \sum_{i=1}^{i=N_e} L_i^e \quad (5-15)$$

where N_e is the number of elements in each fiber. The braid crimp was considered as the average of fibers crimp.

5.4 Results and discussion

The initial pitch length and outer diameter were determined by trial and error to achieve the expected final deformed pitch length. In all presented examples, the following values were set as the input for the Python script to generate the initial geometry: the diamond braid pattern possessed 12 yarns ($N_y = 12$) with an initial pitch length of $P_0 = 20$ mm and an initial outer diameter of $D_0 = 10$ mm. The regular braid pattern contained 8 yarns ($N_y = 8$) with an initial pitch length of $P_0 = 4.5$ mm and an initial outer diameter of $D_0 = 5.5$ mm.

5.4.1 Numerical convergence study

Figure 5.5a represents the convergence of the elongation of the diamond braid under 1N tensile loading against the number of fibers per yarn (fibers/yarn) along with the element size. This figure shows the elongation of the braid for 7, 19, 37, 61, 91 fibers per yarn. Each curve had a result for element size of 0.67, 0.34, 0.23, and 0.17 mm (60, 120, 180, 240 elements per fiber). The results were diverged for 7 and 19 fibers per yarn. Although the model using of 37 fibers per yarn with the element size of 0.23 mm (180 elements/fiber) seems to converge at ~68% of elongation, it diverged with increasing the number of elements to 240 elements per fibers. The 61 and 91 fiber per yarn curves showed convergence at ~68% of elongation with the element size of 0.23 mm. Therefore, the model was converged using 61 fibers per yarn with the element size of 0.23 mm.

5.4.2 Geometrical convergence study

To ensure that the geometry of the model will converge in addition to the numerical convergence of the braid elongation, Figure 5.5b-g demonstrate the geometrical convergence of the model.

These figures illustrate the same axial cross-section of the diamond braid with a different number of virtual fibers per yarn in which five different colors were assigned to each cross-section for better comparison. Figure 5.5 consists of the braid cross-section with 7 (Figure 5.5b), 19 (Figure 5.5c), 37 (Figure 5.5d), 61 (Figure 5.5e), and 91 (Figure 5.5f) fibers per yarn. Figure 5.5g exposes the geometrical comparison. Figure 5.5g layers images with 37 (cyan, upper layer), 61 (purple, middle layer) and 91 (green, inner layer) fiber per yarn. Three layers overlapped and similar cross-section shapes were observed. This comparison showed that 37 fibers per yarn was sufficient to obtain the geometric convergence. However, since the numerical stability of the method has been achieved earlier by 61 fibers per yarn, hereafter 61 fibers were used to model the yarn.

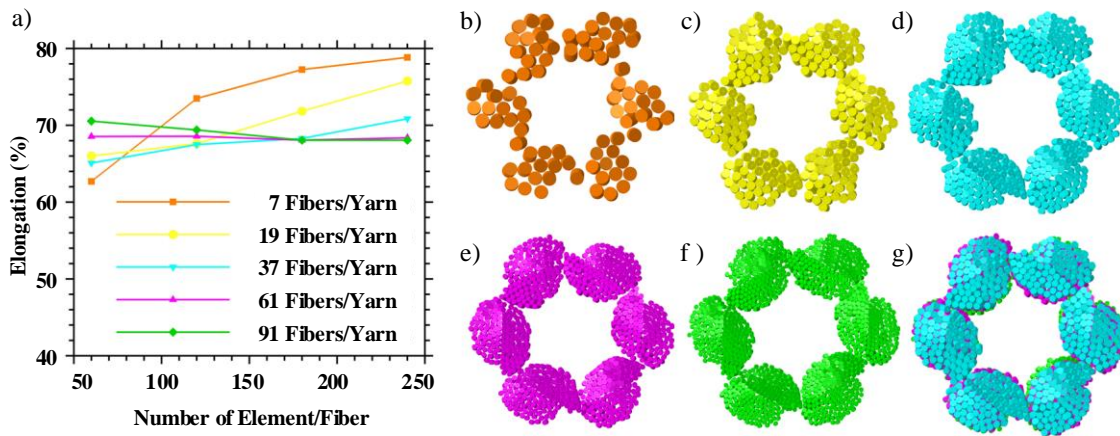


Figure 5.5 (a) Convergence of the elongation of the braid pitch under 1N tensile load. (b-g) Geometrical convergence of the braid cross-section against the number of fibers per yarn. (b) 7 fibers/yarn. (c) 19 fibers/yarn. (d) 37 fibers/yarn. (e) 61 fibers/yarn. (f) 91 fibers/yarn. (g) Comparison of the superimposed cross-sections.

5.4.3 Validation

To validate the present methodology, the diamond and regular braid patterns were modeled and quantitatively compared with the CT scan data of the braided carbon fiber.

5.4.3.1 Diamond braid (1/1)

Figure 5.6a,b show two different cross-sections of A and B with their equivalent CT slices, selected from the diamond braid model. The model predicted the braid's diameters of 3.81 ± 0.08 mm for section A and 3.73 ± 0.11 mm for section B, compared to the actual braid's diameter of 3.89 ± 0.33 mm (Figure 5.6a) and 3.79 ± 0.24 mm (Figure 5.6b) for the equivalent slices. The model predictions were within 2.06% (Figure 5.6a) and 1.58% (Figure 5.6b) percentage errors. Moreover, CT images showed a large void at the center of the braid due to the diamond pattern structure and yarns arrangement. The model well predicted a similar void at the center of the braid's cross-section. Figure 5.6c represents the 3D isometric view of the model with an equivalent CT image. The 3D view of the CT scan illustrated considerable in-plane waviness of the braided yarns. The model correspondingly captured the in-plane crimp of the braided yarns. Also, the same nominal braid angle of 19° was calculated for both model and actual carbon fiber braid using Eq. (5-8).

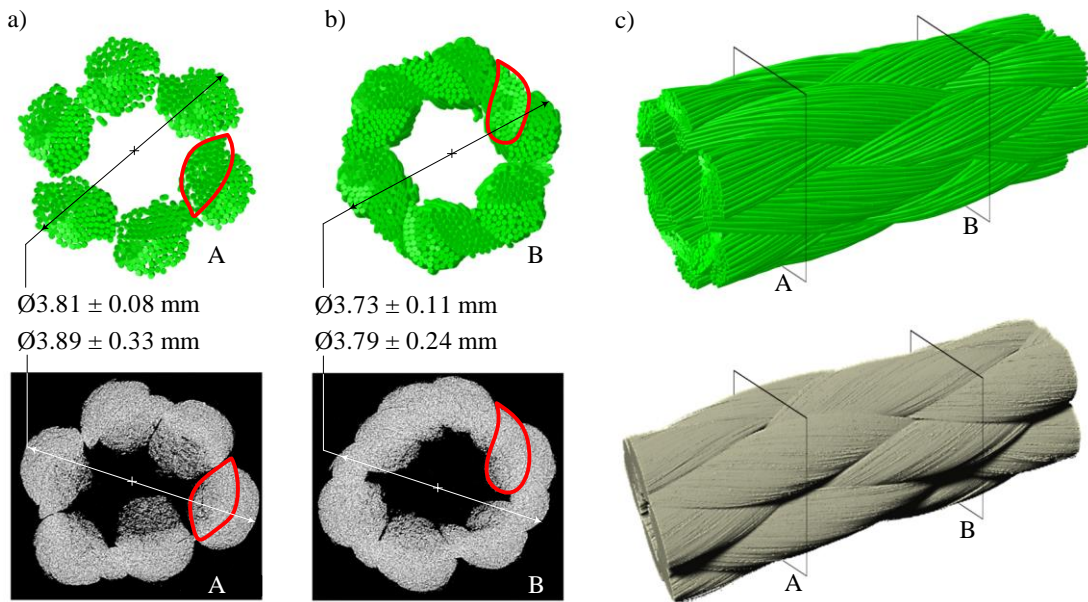


Figure 5.6 Validation of the diamond (1/1) braid model by comparing with the CT images. (a-b) Two different cross-sections comparison. The red closed areas specify the similar yarn cross-section shape between models and CT images. (c) The 3D isometric view comparison between the model and CT scan.

5.4.3.2 Regular braid (2/2)

Figure 5.7a,b indicate two different cross-sections of A and B for the regular braid model with equivalent CT slices. The model's predicted braid diameter of 3.13 ± 0.11 mm was well comparable with the actual braid diameter of 3.10 ± 0.12 mm in Figure 5.7a. Furthermore, the braid diameter of 3.04 ± 0.18 mm was achieved by the model compared with the actual braid diameter of 2.99 ± 0.27 mm in Figure 5.7b. An excellent agreement was found between the predicted diameters and the experimental results for the regular braid with percentage errors of 0.97% (Figure 5.7a) and 1.67% (Figure 5.7b). Moreover, slice A shows small voids at the center of the cross-section as well as slice B demonstrates two small voids between yarns, which well predicted by the model's cross-sections. In addition, Figure 5.7c renders the 3D isometric view of the model with the equivalent CT image. The 3D view of the model also illustrated a good representation of the waviness of the yarn path. Furthermore, the same nominal braid angle of 35° was calculated for both model and actual carbon fiber braid using Eq. (5-8).

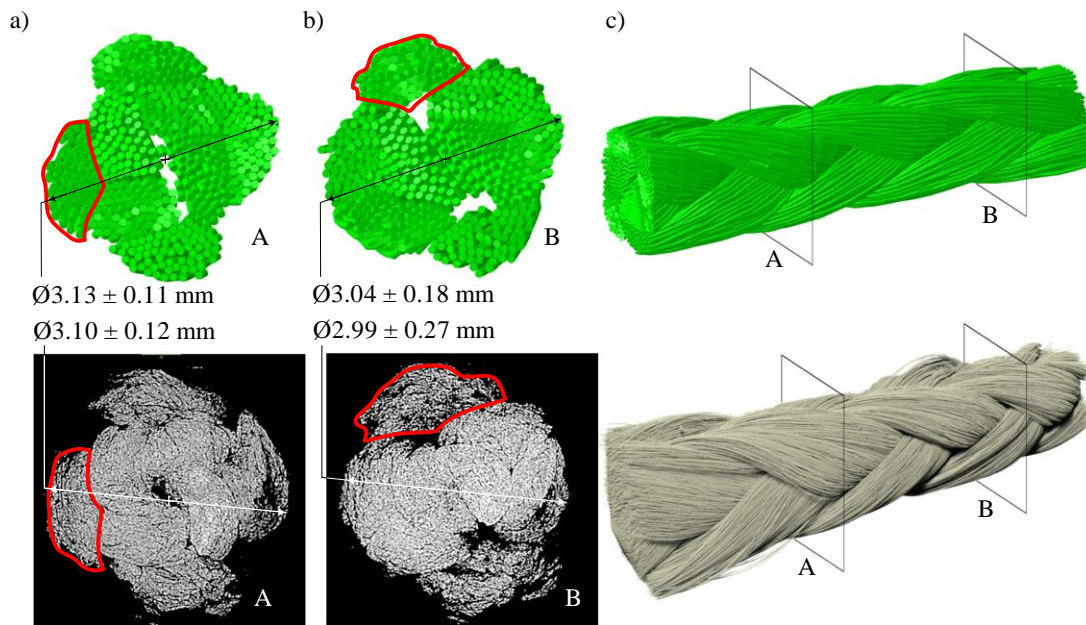


Figure 5.7 Validation of the regular (2/2) braid model by comparing with the CT images. (a-b) Two different cross-sections comparison. The red closed areas specify the similar yarn cross-section shape between models and CT images. (c) The 3D isometric view comparison between the model and CT scan.

5.4.3.3 Yarn cross-section area and aspect ratio

The yarn cross-section area was recognized in CT images by tracking a small gap between the yarn's boundaries. To demonstrate the distinction between yarns' cross-section, a video of braids cross-section along the longitudinal axis is available online (<https://youtu.be/GYRgw8OtA9o>) for both braid patterns of diamond and regular quantified in this paper. For example, a yarn cross-section area of CT images was manually segmented by a red boundary in each Figure 5.6a,b and Figure 5.7a,b with the equivalent yarn cross-sections of the models. A remarkable similarity was visible between the shape of specified yarns of models and the corresponding CT images. The area of the yarn cross-section of models was compared with the equivalent area of CT images for both the diamond and regular patterns in Table 5.2. The model's yarn cross-sections area of 0.66 ± 0.04 and 0.65 ± 0.03 mm² for the diamond pattern were similar to the equivalent area of 0.67 ± 0.10 and 0.66 ± 0.05 mm² of CT images, respectively. Furthermore, the model calculated yarn cross-sections area of 0.82 ± 0.04 and 0.85 ± 0.05 mm² for the regular pattern. Those were similar to the equivalent area of 0.81 ± 0.10 and 0.85 ± 0.12 mm² measured in the CT scan cross-section. The model predicted the area of yarn cross-sections with a mean percentage error of 1.06%.

Table 5.2 Yarn cross-section area comparison.


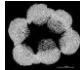

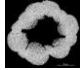

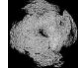

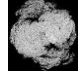

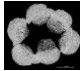

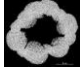

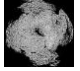

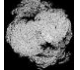
Braid pattern		Model's yarn cross-section area (mm ²)		Actual yarn cross-section area (mm ²)	Error
Diamond (1/1)		0.66 ± 0.04		0.67 ± 0.10	1.49%
		0.65 ± 0.03		0.66 ± 0.05	1.52%
Regular (2/2)		0.82 ± 0.04		0.81 ± 0.10	1.23%
		0.85 ± 0.05		0.85 ± 0.12	0.00%

Table 5.3 compares the yarn aspect ratio between models and CT slices. Two clockwise (CW) and two counterclockwise (CCW) yarns from diamond and regular braid patterns corresponding to slices of A and B in Figure 5.6 and Figure 5.7 were selected for comparison. The aspect ratio of

0.45 ± 0.05 for diamond pattern model was similar to 0.41 ± 0.07 of CT slices. The model predicted 0.50 ± 0.04 for the yarn aspect ratio of the regular pattern, which perfectly matched the same value of CT slices. The quantitative assessment of the yarn aspect ratio revealed excellent agreements between the experimental measurements and the model predictions with a mean percentage error of 3.30%. This insignificant error was created by the slight difference between the prediction and CT data for the CW yarn of the diamond pattern, caused by the asymmetric shape of the CT slice.

Table 5.3 Yarn's aspect ratio comparison.

Braid pattern	Model's slice	Yarn type		Mean	CT's slice	Yarn type		Mean
		CW	CCW			CW	CCW	
Diamond (1/1)		0.47	0.46	0.45 ± 0.05		0.33	0.47	0.41 ± 0.07
		0.38	0.48			0.39	0.46	
Regular (2/2)		0.44	0.50	0.50 ± 0.04		0.44	0.50	0.50 ± 0.04
		0.52	0.54			0.53	0.54	

5.4.4 Parametric studies

5.4.4.1 Jammed state phenomenon: frictional outlook

Figure 5.8a-c illustrate the frictional dissipation energy versus elongation (Figure 5.8a), dimensionless diameter (Figure 5.8b), and braid angle (Figure 5.8c) curves during the deformation. These curves were plotted for three coefficients of friction of $\mu = 0.1, 0.3$, and 0.6 with a modulus of elasticity of 230 Gpa.

The key feature of these diagrams was that each curve was divided into three parts: the linear, non-linear, and linear again. The first linear part had a gentle slope with low frictional dissipation energy and the largest share of the elongation, diameter shrinkage, and braid angle reduction. This part was explained by a large rearrangement of loose fibers with few contacts. This part was also where

yarns rotate toward the braid axis to allow the large elongation of the pitch. The second part exhibited non-linear behavior in which fibers were reoriented with increasing of contacts. The third linear part was able to explain the jammed state phenomenon of biaxial braids. When fibers were sufficiently reoriented, the non-linear behavior switched to the linear through the jammed state. In this state, the frictional dissipation energy immediately increased with a steep slope due to the maximum contact between fibers, while the elongation, diameter, and braid angle had no major changes.

Figure 5.8d-f compare the cross-sections in the middle of the braid pitch for the three coefficients of friction. The yarn cross-sections were slightly compacted by reducing the coefficient of friction. To closer inspect the effect of the coefficient of friction on the yarn cross-section area, the same yarn (the yellow one) was separately shown in Figure 5.8g-i with the yarn cross-section dimensions for the three coefficients of friction. In terms of dimensions, the major diameter (l) was shrunk and the minor diameter (w) was elongated by increasing the coefficient of friction. Figure 5.8j illustrates the comparison of the yarn aspect ratio ($\delta = w/l$) at the jamming state and Figure 5.8k compares the jamming angle for the three coefficients of friction. δ increased as the coefficient of friction increased. The rise in the coefficient of friction from 0.1 to 0.3, 0.3 to 0.6, and 0.1 to 0.6 affected the shape of yarn cross-section with 27.78%, 19.57%, and 52.77% increases in δ , respectively. In other words, the cross-sectional shape of the yarn with a lower coefficient of friction was closer to the lenticular shape. There was also an insignificant change of the jamming angle with the growth of the coefficient of friction. Figure 5.8 j-k show that the increase in the coefficient of friction had a negligible effect on the jamming angle, while it affected the yarn cross-section shape in the jamming state.

5.4.4.2 Modulus of elasticity

The same models were launched for the modulus of elasticity of 60, 150, and 300 GPa with a coefficient of friction of 0.3. The corresponding curves were plotted for the force versus elongation (Figure 5.9a), dimensionless diameter (Figure 5.9b), and braid angle (Figure 5.9c) during deformation. The curves with the different modulus of elasticity were superimposed and no effect on the braid deformation was observed by changing the modulus of elasticity. The jammed state

was also visible at the end of these curve where the elongation, diameter, and braid angle had insignificant variations. Figure 5.9d-f represent the braid cross-sections in the middle of the braid pitch for the three moduli. They showed the similar yarn cross-sections were reproduced by changing the modulus of elasticity. To evaluate more carefully, the same yarn cross-section (the yellow one) in the middle of the braid pitch was separately represented with dimensions for the three moduli of elasticity in Figure 5.9g-i. In the yarn cross-section dimensions, no major changes were observed. Figure 5.9j shows the comparison of δ and Figure 5.9k represents the comparison of the jamming angle for the three moduli of elasticity. These comparisons showed that changing the modulus of elasticity hardly affected the jamming angle, yarn aspect ratio, and yarn cross-sectional shape in the jammed state.

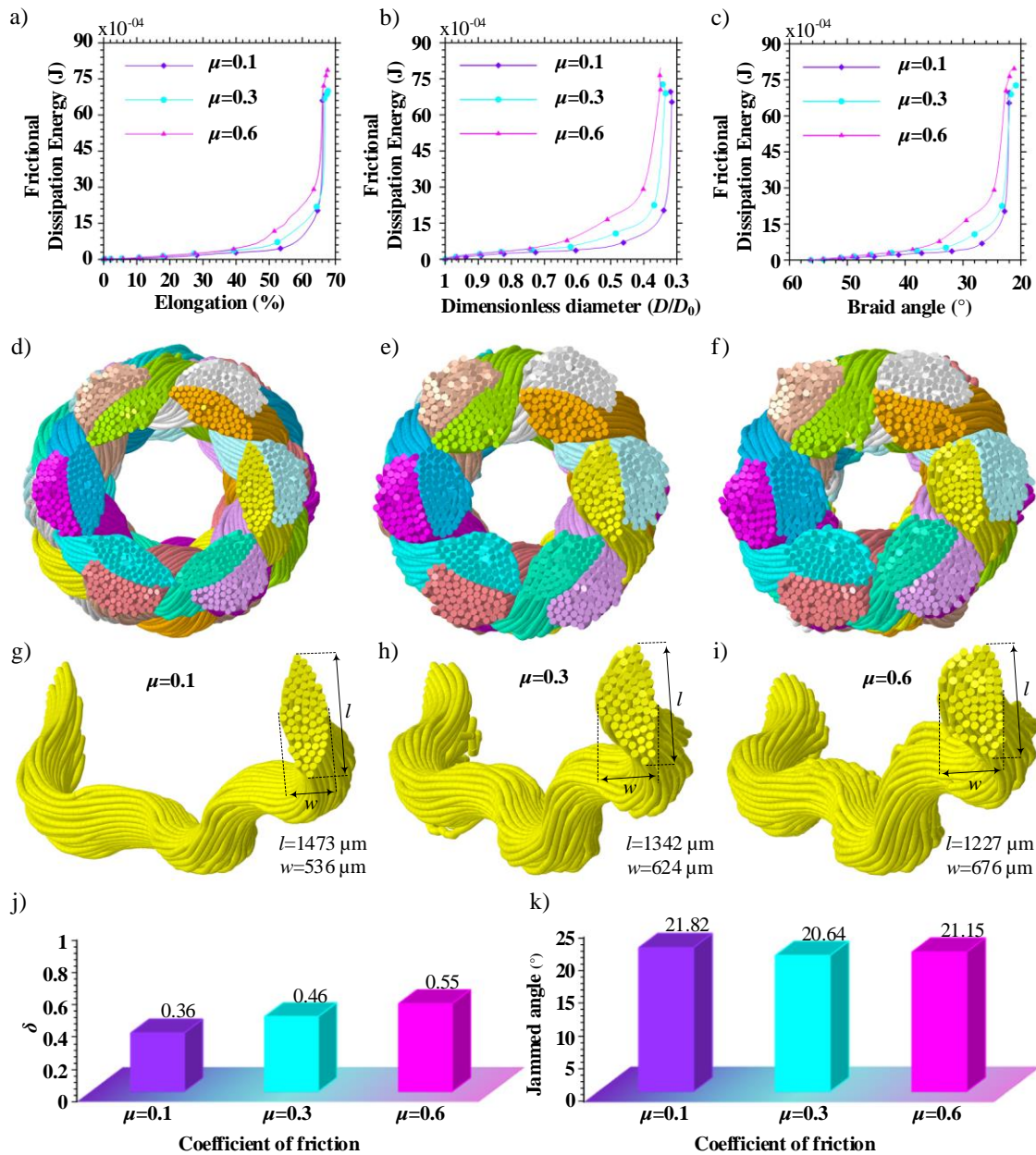


Figure 5.8 Effect of the fiber-level friction on the jammed state and mesoscopic morphology of braids. Diagrams of the frictional dissipation energy against (a) elongation, (b) dimensionless diameter, and (c) braid angle. (d-f) Comparison of braid cross-sections in the middle of braid pitch. (e-g) Quantitative analysis of one of the yarns' cross-sections in the middle of braid pitch. (j) Comparison of the yarn aspect ratio. (k) Comparison of the jammed angle. All comparisons were performed for $\mu=0.1, 0.3$, and 0.6 .

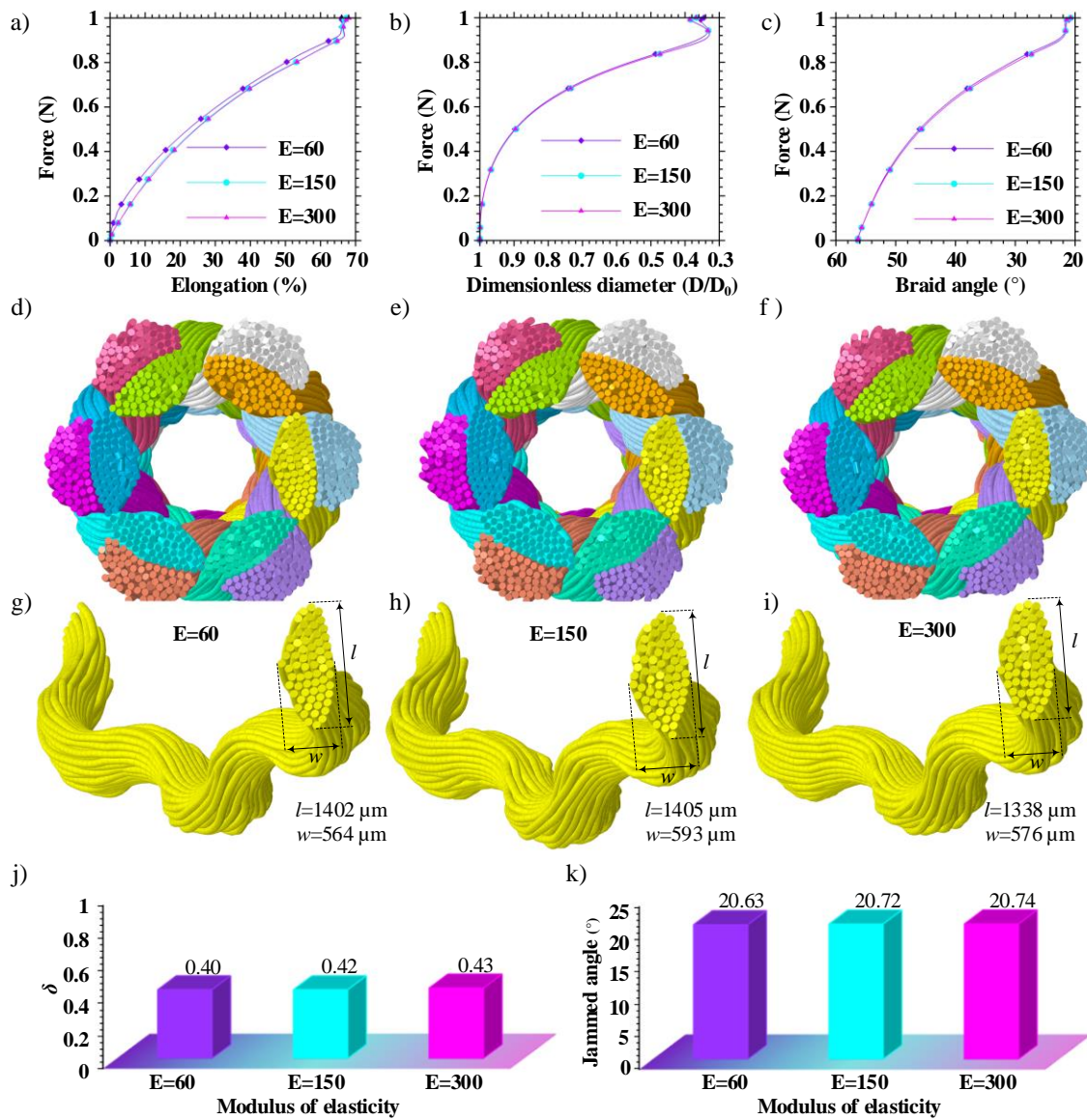


Figure 5.9 Effect of the fiber-level elastic modulus on the jammed state and mesoscopic morphology of braids. Diagrams of the force against (a) elongation, (b) dimensionless diameter, and (c) braid angle. (d-f) Comparison of braid cross-sections in the middle of braid pitch. (e-g) Quantitative analysis of one of the yarns' cross-sections in the middle of braid pitch (j) Comparison of the yarn aspect ratio. (k) Comparison of the jammed angle. All comparisons were performed for $E=60, 150$, and 300 MPa.

5.4.4.3 Crimp

Figure 5.10 compares the crimp of diamond and regular patterns at the jammed state. Figure 5.10 also demonstrates the effects of coefficient of friction (Figure 5.10a) and modulus of elasticity (Figure 5.10b) on the braid's crimp. To investigate the effect of coefficient of friction in Figure 5.10a, bar charts were plotted for three coefficients of friction of $\mu = 0.1, 0.3$, and 0.6 with a modulus of elasticity of 230 GPa. The results of models were also plotted in Figure 5.10b for the modulus of elasticity of $60, 150$, and 300 GPa with a coefficient of friction of 0.3 to evaluate the modulus of elasticity's influence on the crimp of braids. In general, the crimp of regular braid was more than diamond one. For example, the crimp of 10.11% was obtained for the regular pattern with $\mu = 0.3$, $E = 150$, and the jammed angle of 24.17° , which was 1.7% more than the corresponding diamond braid with the jammed angle of 20.64° . These comparisons showed that changing the coefficient of friction hardly affected the crimp. Also, an insignificant impact of modulus of elasticity on the crimp of braids at the jammed state was obtained.

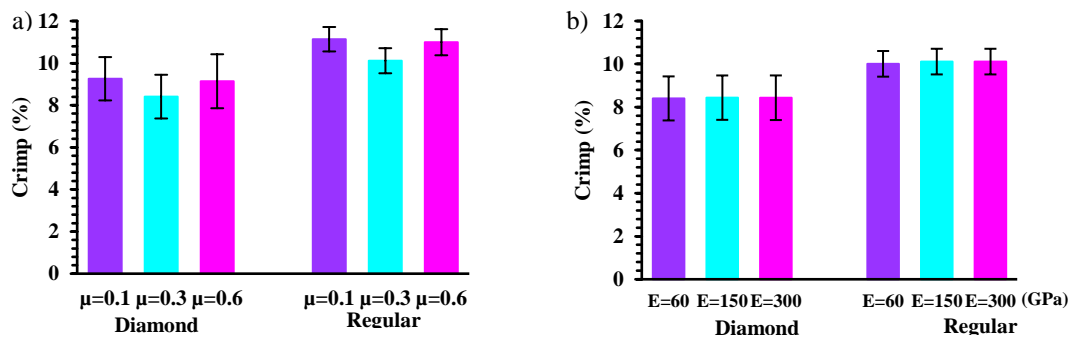


Figure 5.10 Comparison of the crimp percentage between diamond and regular braided patterns at the jammed state for coefficients of friction of $\mu = 0.1, 0.3$, and 0.6 (a) and moduli of elasticity of $E=60, 150$, and 300 GPa (b).

5.5 Conclusions

A numerical modeling methodology was presented to predict the macroscopic geometry and mesoscopic morphology of the diamond and regular biaxial braids. A braided yarn was modeled by a bundle of virtual fibers made of chain of truss elements. The convergence study revealed that

61 virtual fibers per yarn along with the element size of 0.23 mm resulted in a realistic braid geometry simulation. The models well predicted the diameters of both the diamond and regular braided carbon fibers with a mean percentage error of 1.57% compared to X-ray micro CT scans. The arrangement of yarns and braid patterns led to creation of small and large voids in the braid cross-sections, which were well predicted by the simulation. The numerical simulation accurately configured the fibers distribution within yarns and the shape of yarn cross-sections. The area of yarns cross-sections and aspect ratio acquired from the simulation showed an excellent agreement with the experimental data of CT images with a mean percentage error of 1.06% and 3.3%, respectively. The frictional behavior explained the jammed state of biaxial braids when the frictional dissipation energy was quickly increased during deformation, whereas the braid elongation, diameter, and braid angle were stable. Parametric studies illustrated that the increase in the coefficient of friction from 0.1 to 0.6 affected the yarn cross-sectional shape with a 52.77% increase in the yarn aspect ratio, while there were no major changes in the jamming angle and crimp. The variation of the modulus of elasticity in the range of 60 to 300 GPa had an insignificant impact on the mesoscopic morphology, crimp, and the jammed state of the braid. The ability of this modeling methodology is currently being investigated to capture the mechanical behavior of fiber-level biaxial braids. In addition, the potential application of this model is now being employed to understand the sophisticated braid deformation throughout the composite manufacturing process of the thermoplastic braid-trusion technique. These topics are reserved for future publications.

Acknowledgments

This work was supported by the Bombardier Aviation; the Natural Science and Engineering Research Council of Canada (NSERC) [CRDPJ488387-15]; the Advanced Materials Research and Innovation Hub PRIMA Québec [R10-009]; and the Pultrusion Technique Inc. The authors would like to express their gratitude to members of the Shape Memory Alloys and Intelligent Systems Laboratory (LAMSI) at the École de Technologie Supérieure (ÉTS) for CT scans.

CHAPTER 6 ARTICLE 2: MULTISCALE NUMERICAL SIMULATION OF THE FORMING PROCESS OF BIAxIAL BRAIDS DURING THERMOPLASTIC BRAID-TRUSION: PREDICTING 3D AND INTERNAL GEOMETRY AND FIBER ORIENTATION DISTRIBUTION

Mohammad Ghaedsharaf ^a, Jean-Evrard Brunel ^b, Louis Laberge Lebel ^a

^a *Advanced Composite and Fiber Structure laboratory (ACFSlab), Research Center for High Performance Polymer and Composite Systems (CREPEC), Department of Mechanical Engineering, Polytechnique Montréal, 2900 boul. Édouard-Montpetit, Campus of the University of Montreal, Montreal, H3T 1J4, Canada*

^b *Bombardier Aerospace, 1800 boul. Marcel-Laurin, Saint-Laurent, H4R 1K2, Canada*

This article was published in *Composites Part A: Applied Science and Manufacturing*, Vol. 150, November 2021, 106637

Highlights

- The model predicts macroscopic braid architecture changes during pultrusion with an average accuracy of over 99%.
- Mesoscopic morphology and high local fiber volume fraction of a thermoplastic braid-truded rod is predicted.
- Local fiber orientation distributions vary along the braid radius; conversely, they are uniformly distributed along the braid pitch.
- There are significant differences between the local fiber orientation and the nominal braid angle.

Abstract

Thermoplastic braid-trusion is a composite manufacturing process that combines braiding and pultrusion of hybrid yarns containing reinforcement and polymer fibers. During pultrusion, the melting of the polymer fibers leads to complex morphological changes at the macro, meso and micro scales. We introduce here a multiscale numerical simulation methodology to model this process. In this methodology, braided yarns are modeled as bundles of virtual discrete fibers using chains of truss elements. A thermoplastic composite braided rod was pultruded according to the simulated braid-trusion. During braid-trusion, it was observed that the braid architecture was significantly modified, which was reliably predicted by the model through macroscopic measurements of 7.6% pitch elongation, 44.0% diameter reduction, and 45.0% nominal angle reorientation. The model also predicts the yarns' cross-section area having high local fiber volume fraction of about 60% due to yarn compaction during pultrusion. These predictions of mesoscopic morphology and internal geometry are quantitatively validated using X-ray micro-computed tomography (CT) scans of the braid-truded rod. Three local fiber orientation distributions of the in-plane, out-of-plane, and with respect to the longitudinal braid axis are extracted using micro-scale analysis of virtual fibers. We found that a significant amount of fibers are oriented around specific radii ranging from 30 – 70% and 60 – 100% of the outer radius before and after pultrusion, respectively. By contrast, the local fiber orientation is uniformly distributed along the pitch length. The microscale model also shows considerable discrepancies between local and nominal braid angles.

Keywords: Thermoplastic resin; Micro-mechanics; Process Modeling; CT analysis; Pultrusion

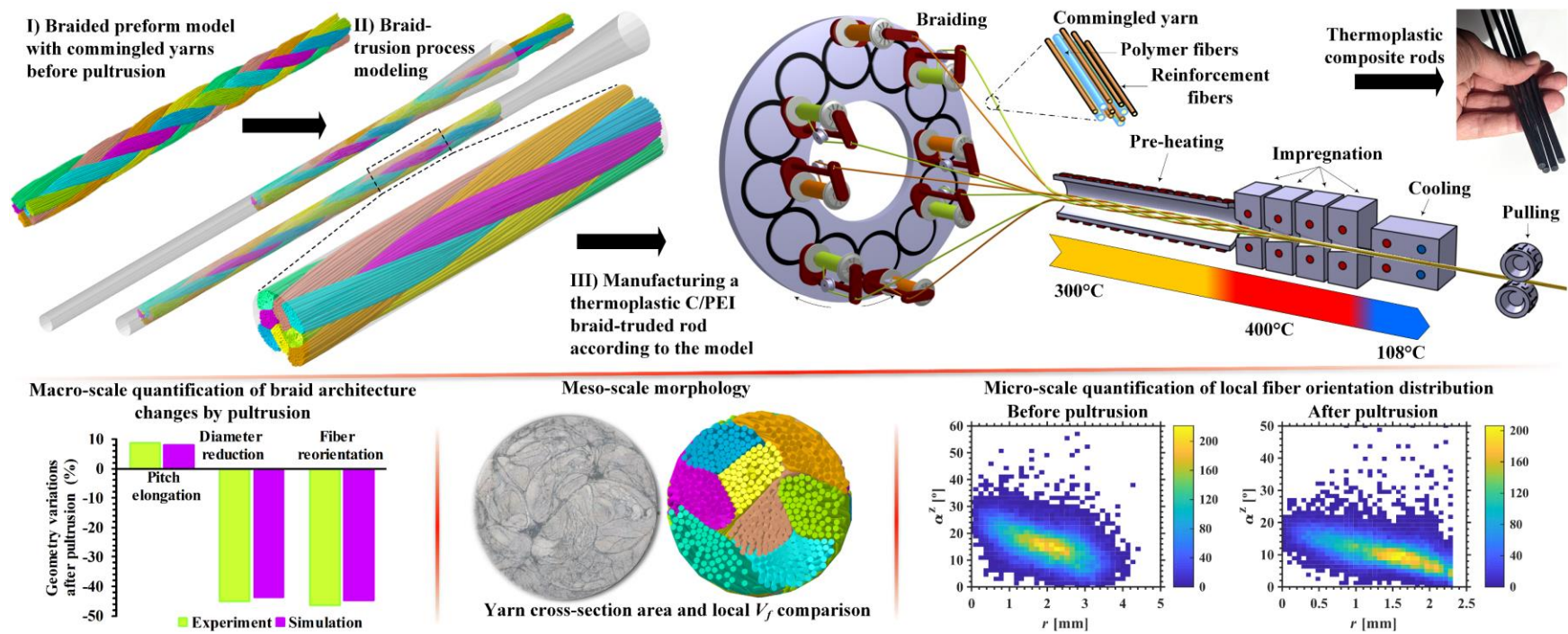


Figure 6.1 Graphical abstract

6.1 Introduction

Pultrusion is an uninterrupted manufacturing technique to produce fiber-reinforced polymer composites with constant cross-sections and high-fiber volume fraction using both thermoset [12, 101-104] and thermoplastic [105-111] matrix systems. The fiber orientation of pultruded composites is usually unidirectional; however, pultrusion of braids allows control of the fiber orientation in desired directions [22, 112]. Braiding is an ancient textile manufacturing technique, which today is very attractive to composites manufacturing due to the arrangement of multi-directional fibers [13, 22]. Both braiding and pultrusion are highly automated techniques [13], the combination of which provides the braid-trusion technique [22, 112].

Triaxial and biaxial braids are the two most common 2D braid structures [20]. Figure 6.2a,b illustrate the structure of triaxial and biaxial braids. The triaxial braids have three yarns system arrangements consisting of two bias yarns having a nominal braid angle (α) with respect to the braid longitudinal axis as well as an extra axial yarn parallel to the longitudinal braid axis [20]. The axial yarn secures the braid structure under axial loads [24, 25]. In comparison to triaxial braids, biaxial braids have only two oriented yarn system arrangements [20]. The absence of axial yarns in biaxial braids confers a high formability advantage. Figure 6.2c shows the formability of the biaxial braid under axial loads. The biaxial braid structure easily deforms under axial tensile and compressive loads. The tensile axial force elongates pitch length and reduces diameter. Conversely, the compressive force leads to a reduction in pitch length and an expansion in diameter. Given the stable nature of the structure of the triaxial braids, most studies have reported that only the triaxial braids were used as reinforcements in thermoplastic braid-trusion [1-3, 5, 6]. In addition, the most important advantage of thermoplastic composites over thermosets is their recyclability since they can be reshaped after forming process through a thermoforming procedure [9]. A combination of advantages of biaxial braids and thermoplastic materials motivated us to manufacture thermoplastic composites reinforced by biaxial braids having high formability in a post-forming process [10].

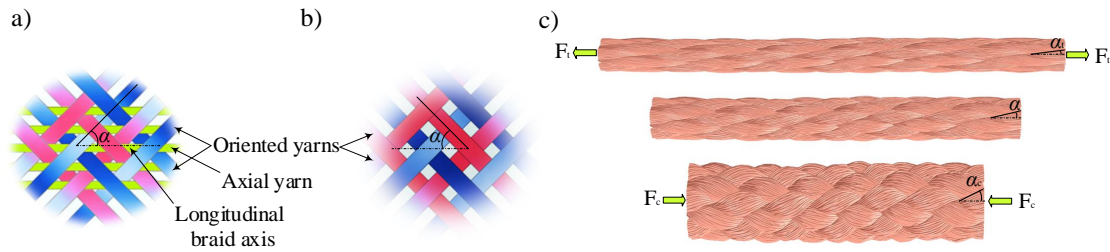


Figure 6.2 (a) Triaxial and (b) biaxial braid structures. (c) Deformation of the biaxial braid under tensile (F_t) and compressive (F_c) loads. α is the braid angle with respect to the longitudinal braid axis ($\alpha_t < \alpha < \alpha_c$).

There are few publications on thermoplastic braid-trusion [1-3, 5, 6] and the process is still under development [9, 10]. Figure 6.3 illustrates a schematic of an example of a thermoplastic braid-trusion system. The braiding machine is joined to the pultrusion apparatus to feed hybrid yarns into the system [1-3, 5, 6]. The hybrid yarns are an intimate mix of thermoplastic and reinforcement fibers, having advantages such as low impregnation flow path length and ease of handling [1, 15]. The most commonly used hybrid yarns for thermoplastic braid-trusion are the parallel hybrid or the co-wound [1], commingled [1, 2], and pre-consolidated tapes [9]. The braid is formed by intertwining yarns by moving two sets of yarn carriers in opposite directions along a sinuous circular track. Figure 6.3 shows four carriers rotating clockwise and four others rotating counterclockwise. To reduce the required time for melting the thermoplastic polymer, the braid is first preheated to a temperature close to the thermoplastic polymer melting point in the preheating module [1-3, 5, 6]. In Figure 6.3, this pre-impregnation die is shown as a hollow tube with an electrical heating tape wrapped around it. A traction system then pulls the preheated braid into an impregnation module. Figure 6.3 presents an impregnation module of a multi-die system, including four successive heated dies [10, 88, 113, 114]. Each heated die has a tapered zone where the molten thermoplastic polymers impregnate braided fibers. The decrease of the cross-sectional area of the tapered zone creates a backflow of melted polymers, causing more pressure to achieve better impregnation [17, 18]. The die filling ratio was also defined as the material area at the die entrance over the exit area, which should be over 100% to reach resin back-flow. Each of the four heated dies also has a constant cross-section zone and the last one is connected to the cooling die where

the thermoplastic polymers are solidified. This system has shown an effective improvement in the surface finish of pultruded products while limiting adhesion forces [114].

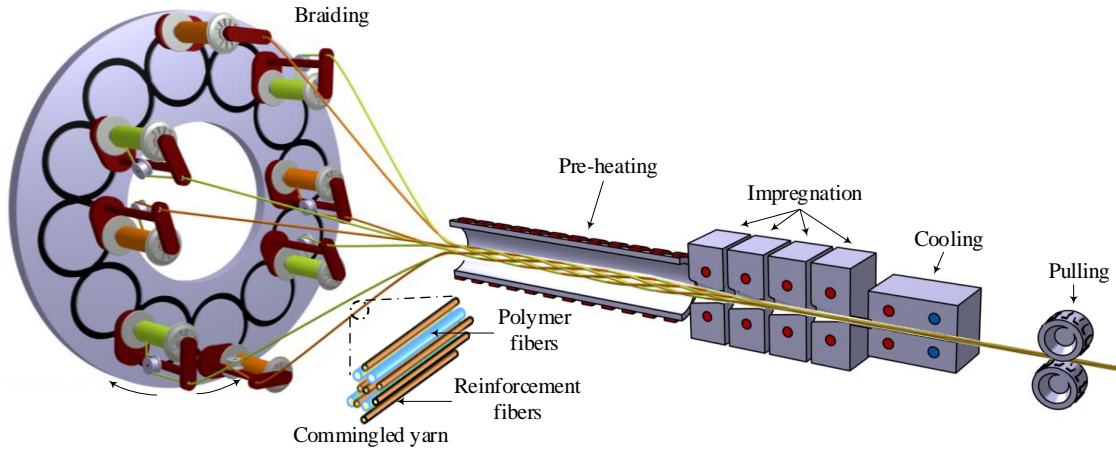


Figure 6.3 Thermoplastic braid-trusion system. The braiding machine feeds braided commingled yarns into the system. After preheating, the polymer fibers melt in heated dies, impregnate the reinforcement fibers, and solidify upon cooling.

Thermoplastic braid-trusion is a challenging process due to the complex deformation phenomena of the braid inside the pultrusion die. Braids are subjected to axial tension during the pultrusion process, which leads to change of the braid architecture and the reorientation of fibers. In the case of using triaxial braids [5], the pulling force has no role in the reorientation of the fibers since the longitudinal deformation is restrained by the axial yarns. Nevertheless, the consolidation only contributes to the reorientation of the fibers through the expansion of the braid perimeter. By contrast, in the case of braid-trusion using biaxial braids [10], the braid deformation is more complicated since the pulling force not only elongates the braid pitch but also reduces the braid perimeter. So the main challenge is the proper filling of the pultrusion die cross-section by the braided fibers. If the braid perimeter is shorter than the die cavity cross-sectional perimeter, the fibers cannot be well distributed throughout the cross-section of the profile, creating resin-rich regions and undesirable voids. On the contrary, if the braid perimeter is too long, the friction forces on the die wall increases due to compacted fibers, fibers may break, leading to an interruption of the process. A modeling methodology is hence required to design the braid for the braid-trusion process. However, most studies in the field of thermoplastic braid-trusion have not proposed a

design methodology for the pultrusion of braids, nor have they given specific details about the braid architecture used. Most reported designs of the braid architecture have been followed by the experimental trial-and-error method to achieve successful braid-trusion. Laberge Lebel and Nakai [5] developed a geometrical model and proposed a design method for triaxial braids to manufacture an L-shaped beam. Their model described the circumferential deformation of the triaxial braid when the braid was compacted in the die. They hypothesized that yarns had constant elliptical cross-sections. This did not represent the reality where yarns are shaped by compression inside the die, interactions of the yarn with adjacent yarns and the die wall, and intra-yarn fibers rearrangement. Ghaedsharaf et al. [10] proposed a simple and successful design methodology for biaxial braids to manufacture a thermoplastic braid-truded rod using a multi-die pultrusion line. To describe the geometry of a tubular braid, they opened and flattened the tubular braid as a rectangle in which the width, height, and diagonal were the braid circumference, pitch length, and fiber length, respectively. They assumed that the length of the braided fiber (rectangle's diagonal) was an invariant geometrical parameter before and after pultrusion. Based on this assumption, they calculated the pitch length and the nominal braid angle after pultrusion. Although these geometrical models might be the only design of the braid that has been reported for the thermoplastic pultrusion, there were simplifications and uncertainties since the fiber-to-fiber contacts as well as the interaction between fibers and the die wall were neglected. The major problem of the geometrical models was the lack of an accurate prediction of the braid angle before and after pultrusion. Furthermore, the geometrical models were unable to predict the correct filling of the die by the braid deformation and detect the manufacturing-induced defects such as yarn wrinkles.

Reinforcing fibers have an inherent multiscale and discrete nature and can be categorized into three microscopic, mesoscopic, and macroscopic scales. Micron-sized discrete fibers are bundled together to make a meso-sized yarn and discrete yarns are intertwined to fabricate a macro-sized preform. Based on the multiscale and discrete nature of preforms, the forming process can be simulated in one or a combination of three scales to understand different aspects of the same problem. Most macroscopic models simulated the preform as a continuous medium [44-46, 48, 49]. The general assumption of considering the preform as a continuous medium was the absence of macroscopic slippages between yarns [50]; however, this assumption has been disproved for

some forming processes that had large macroscopic slippages between yarns [71]. In addition, given the nature of such discrete structures of reinforcements, the continuous models neglected the local fiber slippage [50]. The discrete models can compensate for these weaknesses of the continuum models. The discrete models can be categorized into yarn-level (mesoscale) [51, 56, 57, 59, 60] and fiber-level (microscale) [61, 62, 64, 70, 96, 115-119] approaches. The yarn-level approaches considered the yarn as a solid continuum model [51, 56, 57, 59, 60]. Since the yarn is inherently discrete, the yarn-level approaches needed a specific mechanical behavior to simulate the fibrous nature of the yarn. Although the mesoscopic approaches provided reliable models, they required the complex constitutive laws of continuum mechanics [57]. Compared to the approaches previously described, the fiber level modeling approaches have provided realistic simulations by considering the fiber slippages and the contact friction between fibers [61, 62, 64, 70, 84, 96, 115-119]. The digital element approach (DEA) has been developed to simulate the geometry of fiber-level fabrics [61, 62, 64]. This approach discretized a yarn into a bundle of fibers with proper contact representation between fibers. Each virtual fiber was made of a chain of truss [61, 62, 84, 96] or beam [66, 97] elements.

In the light of reviewed works, the major challenges in the field of thermoplastic braid-trusion are inadequate research on the use of biaxial braids, the complex deformation of braids during pultrusion, the correct filling of the pultrusion die by the braided fibers, and the lack of a reliable model to understand above-mentioned challenges. Given the recent numerical fiber-level simulations and the lack of adequate research in the forming process of braids during pultrusion, it is important to simulate the process using an approach that is able to take into account the fibers' slippages and mechanical interactions between fibers and the die wall.

We propose a numerical simulation methodology for the forming process of biaxial braids during thermoplastic braid-trusion in an explicit fiber-level finite element framework. Inspired by the digital element approach, the virtual fibers were bundled as a yarn. The fiber's flexibility behavior was imitated using a chain of truss elements. A thermoplastic composite rod was successfully pultruded using the designed braid. The model was quantitatively validated using X-ray micro-computed tomography (CT) data. To explore how the pultrusion process affects the braid architecture, comparison studies between the braided preform and pultruded braid were conducted

using a multiscale quantitative analysis. At the macroscopic scale, the pitch length, diameter (thickness), and nominal braid angle were compared before and after pultrusion. The mesoscopic morphology and local fiber volume fraction of yarns were predicted along the braid-truded rod. The microscale braid model also provided access to the local fiber orientation distribution.

6.2 Workflow

This work contains four main steps. First, the braided preform is simulated (step I). Second, the braid-trusion process is simulated (step II). Then, a thermoplastic composite rod is braid-truded using the model (step III). Finally, a quantitative validation is performed comparing post-processing analyses of the model using the manufactured braid-truded rod characterization (step IV). Figure 6.4 displays the modeling workflow, described by the following steps I and II. Figure 6.8 also shows the manufacturing of a thermoplastic braid-truded rod, which is briefly explained in step III as follows.

- I. To model a biaxial braid before pultrusion, a Python script automatically generated a loose braid geometry in the finite element analysis software Abaqus 6.18 (Figure 6.4a). In this step, the fiber material cross-section area was considered as the commingled yarn including the total area of reinforcement and polymer fibers. Each yarn was modeled as a bundle of virtual fibers (Figure 6.4a). The simulation was conducted by applying small loads on the initial braid geometry (Figure 6.4b). The result is a relaxed braid geometry as obtained after the braiding process (Figure 6.4b). The model was solved using the Abaqus/Explicit solver. This solver is well suited to handle the complex contact between fibers and the highly nonlinear deformation.
- II. The braid-trusion process was simulated. This step began with the modeling of a biaxial braid with similar pitch length and diameter as the previous step (Figure 6.4c), except that the yarns were only composed of reinforcement fibers since the polymer fibers were melted during pultrusion. This difference in material area is shown in Figure 6.5. The pultruded braid was then modeled by moving a pultrusion die over the braid, effectively filling the die by the braided fibers (Figure 6.4d-h).

- III. The designed braided preform was manufactured using commingled carbon and polyetherimide (PEI) fiber yarns. The manufactured braid was then successfully pultruded using a multi-die pultrusion line to manufacture a thermoplastic composite rod (Figure 6.7).
- IV. To validate the model, a multiscale quantitative analysis was carried out. After macroscopic measurements of the braided preform and pultruded rod, a quantitative mesoscopic morphology of the pultruded rod was conducted using the X-ray micro CT of the pultruded rod. The microscopic fibers orientation distribution of the braid was also compared before and after pultrusion.

The steps above are described in detail in the following subsections.

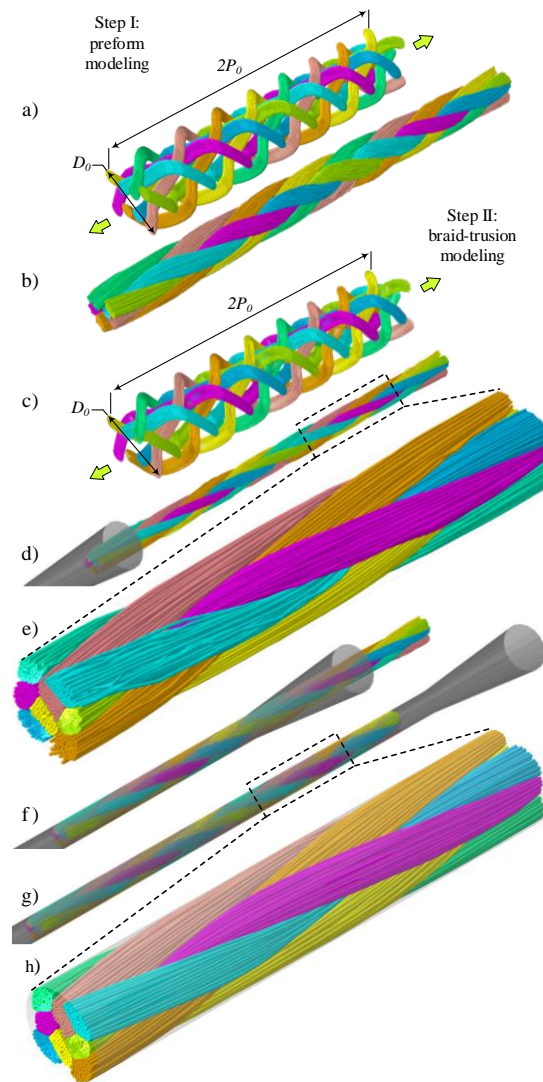


Figure 6.4 Workflow of the modeling procedure. (a,b) Step I: model of braided preform. (a)

Initial braided preform geometry. The fibers cross-section area was considered the sum of reinforcement and matrix fibers area as commingled fibers. (b) Relaxed unconsolidated braided preform geometry. (c-h) Step II: braid-trusion simulation. (c) Braided reinforcement geometry in which fibers cross-section area is considered as the reinforcement fibers' area only. P_0 , D_0 , and loading conditions are the same as the braided preform. (d-g) Braid-trusion simulation in which the pultrusion die moved over the braid. (d) Braid before pultrusion. (e) Magnification of the braid before entering the die. (f) During pultrusion. (g) The braid is inside the straight section of the pultrusion die. (h) Magnification of the braid-truded rod.

6.3 Modeling methodology

A loose braid with a regular pattern (2/2), a diameter (D_0), and an initial length of two pitches ($2P_0$) was automatically generated by a Python script. The braid was modeled with two pitches length because a region of interest that is equal to one pitch length from the middle of the model was selected for post-processing analysis; this will allow the analyzed segment to be far enough from the ends and probable effects of boundary conditions. The number of fibers per yarn (N_f) was specified by an algorithm generating a circular packing arrangement, which has been provided in another study [84]. Since the computational power limitation precluded the use of an actual number of fibers (e.g. 30 000 fibers per yarn) to model a yarn, simulations were conducted with a lower number of fibers, while still providing an accurate representation of the yarn's geometry. The reduction in the number of fibers increases the diameter of virtual fibers. If fibers are made of beam elements, the increase in the diameter causes a large growth in the bending and torsional stiffness of the virtual fibers [66, 97]. To circumvent the increase in the flexural stiffness, we modeled virtual fibers using chains of truss elements with the actual modulus of elasticity of carbon fibers ($E=230$ GPa) instead of beam elements. A truss element is a two-node member, in which nodes allow only translational motions, i.e., they have three degrees of freedom. The end-to-end connected nodes shared their translational degrees of freedom to simulate the flexibility of fibers. Each fiber was meshed using T3D2 truss elements. This number of fibers and the size of elements were determined by studying the convergence of the braided yarn's geometry. The detail of the convergence study can be found in Ghaedsharaf et al. [84]. Based on this convergence study, 61 fibers per yarn along with the element size of 0.23 mm were used to model the yarn.

A dry biaxial braid made of commingled fibers was first simulated by loading the loose fibers to generate a braided preform before pultrusion. In a quasi-static framework, a small tension of 0.1N was smoothly applied to both ends of the loose braid in the axial direction to achieve the realistic braid geometry. As the braid has a periodic structure, periodic boundary conditions were prescribed at both ends of fibers in the lateral directions [84]. The total cross-section area of fibers (A_t) was determined as the sum of reinforcement and matrix filament area in the commingled fibers before pultrusion according to Eq. (6-1),

$$A_t = A_f + A_m \quad (6-1)$$

where subscripts f and m indicate the properties of reinforcement of fibers and matrix materials, respectively. The areas of reinforcement and matrix are expressed by Eq. (6-2),

$$A_f = \frac{Y_f}{\rho_f}, \quad A_m = \frac{Y_m}{\rho_m} \quad (6-2)$$

where Y is the yarn's linear density (g/Km), ρ is the density (g/cm³). The carbon and PEI commingled fibers' cross-sectional area is shown in Figure 6.5a.

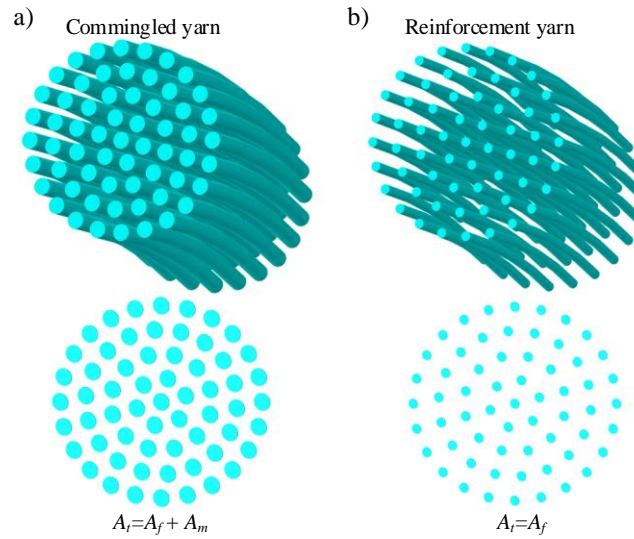


Figure 6.5 (a) Commingled yarn cross-section area. The total cross-section area of fibers (A_t) was determined as the sum of reinforcement (A_f) and matrix (A_m) filament area in the commingled fibers before pultrusion. (b) Reinforcement yarn cross-section area. As the matrix fibers were melted during pultrusion, the total cross-section area of fibers was lowered to only reinforcement fibers area (A_f).

The matrix fibers were melted during the pultrusion process and hence only the cross-section area of the reinforcement fibers (A_f) was considered for pultrusion simulation. The reinforcement fiber area is shown in Figure 6.5b. The pultrusion process simulation consisted of two steps, beginning with the simulation of the braided preform made of only reinforcement fibers following the same

procedure described above. The initial braid pitch, fibers length, and braid diameter of that reinforcement-only braid were the same as the model of the braid with commingled yarns.

Figure 6.6 shows a pultrusion die created as a rigid shell consisting of tapered and cylindrical zones. The tapered length was 31.75 mm with a tapered angle of 5° and the cylindrical zone had a length of 150 mm. During the experiment, the thermoplastic polymer solidifies upon cooling which keeps the braid in a consolidated state. In the simulations, the polymer was not modeled. Therefore, a straight cylindrical die section of 150 mm was used. This ensures that the full length of the braid is constrained by the die cylindrical wall after its passage in the conical portion. This prevents the deconsolidation of the braid during simulation. The die was meshed using 6588 three-dimensional four-node quadrilateral discrete rigid elements of R3D4. The die was then moved over the braided preform from the tapered side, which was coaxially located next to the braided preform. A displacement of 150 mm was smoothly applied to the die in the axial direction (z -axis). The other transverse and rotational movements of the die were constrained. Also, only one end of the braid that first touched the die was fixed in the axial direction (z -axis) while no constraints were assigned to another end, allowing the braid to elongate during pultrusion

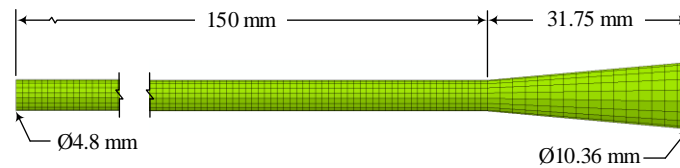


Figure 6.6 Rigid die meshed using 3D four-node quadrilateral discrete rigid elements.

The general contact algorithm of Abaqus/Explicit was used to handle the inter-fibers contact and the interaction between the die wall and fibers. General contact allows detecting many contact regions automatically and is appropriate for fiber-to-fiber contacts. Penalty friction formulation was defined for the contact mechanical tangential behavior. To avoid convergence problem, this formulation models the stick-slip frictional behavior by replacing the “stick” component by a so-called “elastic slip” where small relative movement is allowed. This movement is guided by a penalty stiffness that is computed based on the element length. Details about this formulation can be found in Abaqus documentation [98]. For the slip component of the relative motion, a coefficient

of friction of 0.3 was used which has been proposed for carbon yarn interaction of braiding [99]. To minimize the penetration between touching fibers, hard contact was used in the pressure-overclosure relationship for the contact mechanical normal behavior.

6.4 Experiments

6.4.1 Materials

The reinforcement was carbon fibers (AS4, HEXCEL, $\rho=1.79 \text{ g/cm}^3$) and the matrix was PEI (Ultem, $\rho=1.27 \text{ g/cm}^3$) in the form of fibers. These fibers were commingled (Concordia Fibers LLC) and coated with 1 wt% proprietary sizing. Two yarns type were used. The first one commingled a 3K carbon filament tow ($Y_f = 0.2 \text{ g/m}$) with PEI fibers in a 58 vol.% ratio. The second one commingled a 12K carbon filament tow ($Y_f = 0.8 \text{ g/m}$) with PEI fibers in a 54 vol.% ratio. A commingled yarn of 30,000 (30K) carbon fibers was assembled by co-winding two 3K and two 12K carbon fibers around bobbins. The 30K commingled yarns contained 56 vol.% of carbon and 44 vol.% of PEI.

6.4.2 Braiding

A 24-carrier braiding machine (KBL-24-1-110, Xuzhou Henghui Braiding Machine Co., Ltd.) produced a regular braid pattern (2 over 2) without a mandrel. A 15 m braid was manufactured using eight 30K commingled yarns. Only 8 carriers of the braiding machine were equipped with bobbins, four rotating clockwise and four rotating counterclockwise. The carrier rotation speed was 0.13 RPS and the braid take-up speed was 4.5 mm/s. The resulting pitch length was 34 mm.

6.4.3 Pultrusion

The braided preform was then wound around a spool and mounted on a tension-controlled creel set at 2N in front of the pultrusion line. Figure 6.7 exhibits a forming assembly of a multi-die pultrusion line. The pultrusion apparatus was comprised of a preheater, four heated dies, a cooling die, and a puller system. The puller system pulled the braid into the forming assembly. The braid was first passed through the preheater with a temperature of 300 °C below the melting point of PEI. The

preheater was made of a heating tube with a length of 300 mm and an inside diameter of 50 mm wrapped by a controlled heater. The braid was then entered into the multi-die heating system composed of four consecutive dies separated by a distance of approximately 2 mm. Each heated die molding surface consisted of a tapered conical zone followed by a straight cylindrical zone. The tapered length was 31.75 mm with a tapered angle of 5° with respect to the die axis. The cylindrical length was 6.65 mm. The last die had an extra protruding thin-walled tube inserted into the cooling die's inlet. The tube created a separation distance of 8.4 mm between the last heating die and the cooling die. The internal and external diameters of the tube were 4.8 and 6.39 mm. This tube low cross-section limits the thermal interference between the heating and cooling dies. Explanations of this cooling system can be found in a recently published study [114]. Each heated die was heated to the PEI's processing temperature of 400°C using two controlled cartridge heaters. In the heated dies, the melted polymers impregnated the reinforcing fibers bed. The diameters of the cylindrical zones were designed in the order of 5.1, 5.0, 4.9, and 4.8 mm. The designed reduction in the diameters gradually increased the fiber volume fraction (V_f) of the pultruded braid. The calculation method of the fiber volume fraction and filling ratio has been provided in the previous study [10]. Based on the nominal braid pitch, diameter and fiber angle, the fiber volume fraction of the braid in the dies was 48%, 50%, 52%, and 54% from the first to the fourth die. The decrease in the dies' diameter also allowed material overfilling of the dies with ratio of 102.74%, and 106.9% in the last two dies. The braid was finally solidified in the cooling die having a length of 47.6 mm and a diameter of 4.8 mm. The die was equipped by two cartridge heaters and two air-cooling channels to accurately control the cooling temperature. The temperature of the cooling die was reduced to half of the glass transition temperature of PEI ($T_g/2$) based on the findings indicated in previous practical study of the cooling die temperature [10]. All temperatures were controlled using embedded thermocouples (type J) through a closed-loop control system. The 15 m braided preform was pultruded at a processing speed of 50 mm/min. The speed was read by an encoder. The entire set of components from the preheater to the cooling die were assembled on two guide rails fastened on linear bearings, moving only in the pultrusion direction. A load cell blocked the movement of the assembly to read the pulling force. A data

acquisition system (LabVIEW) recorded temperatures, speed, and force using sensors connected to a computer during the experiment.

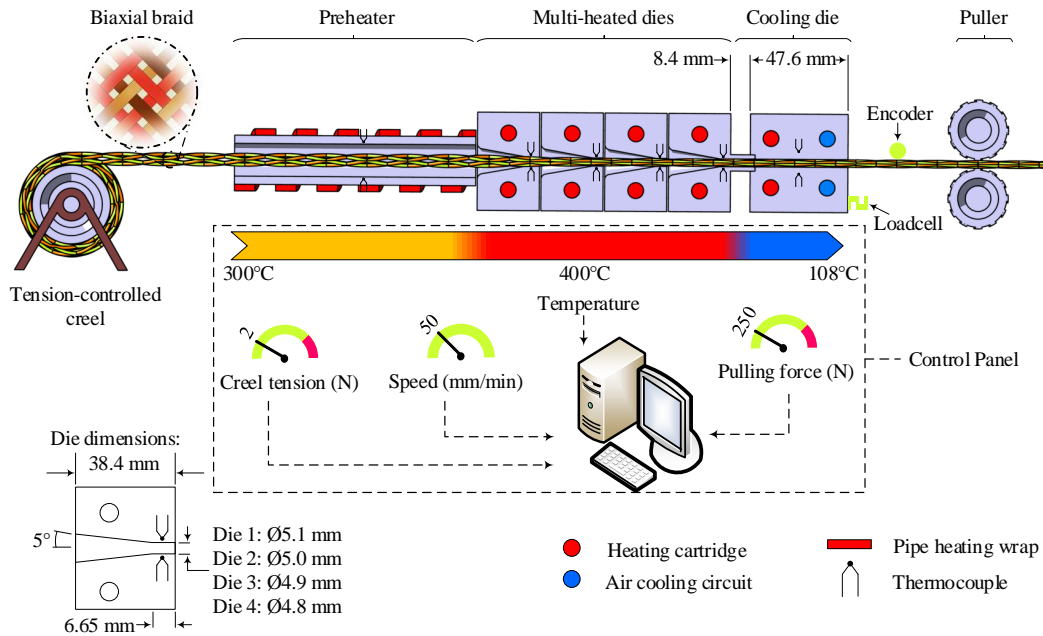


Figure 6.7 Schematic of cross-section view of the multi-die pultrusion system. The apparatus consisted of a tension-controlled creel, preheater, four heated dies, cooling die, puller, and control unit.

6.5 Characterization

6.5.1 X-ray micro computed tomography scan (CT scan)

A 50 mm specimen cut from the pultruded rod was scanned using an X-ray CT system (Xradia-520 versa, Zeiss). The specimen was scanned at two overlapping positions stitched together to assemble a 3D image stack of a 10 mm composite rod. The radiographs were acquired with a voxel size of 5 μm , a beam energy of 50 kV and a current of 80 μA . Two sets of 3200 projections were acquired then stitched for the image reconstruction. The image reconstruction and stitching were automated using Scout-and-Scan Control System (v14.0, Zeiss). The stitched reconstructed 3D image consisted of 1800 slices perpendicular to the rod axis. The reconstructed images were imported into Dragonfly software (version 2020.1, Object Research Systems (ORS) Inc.) for

segmentation, 3D visualization, and quantitative analysis. Since the contrast between carbon fibers and matrices was low in CT images, two yarns were segmented to distinguish the regions of interest. To shorten the analysis, only one yarn of clockwise and one yarn of counterclockwise were segmented here. Ten slices at every 180 slices were selected for manual segmentation. Both yarns in the selected slices were manually labeled with two colors of orange and green, following by the use of an interpolation operation tool in the software to fill the slices between the 10 selected ones with the corresponding labels.

6.5.2 Quantitative analyses

The fiber orientation, pitch length, and radius of the braid were quantitatively analyzed before and after the pultrusion at both macroscopic and microscopic scales. The mesoscopic morphology analysis of the yarn cross-section area and the local fiber volume fraction were also quantified for the pultruded braid. All quantitative analyses of the model were investigated along one pitch length centered on the modelled braid of a total length of two pitches.

6.5.2.1 Macroscopic scale

The nominal braid angle was determined by the following relation in which πD was the braid circumference and P was the pitch length equal to the length of the braid for one complete carrier rotation.

$$\alpha_{nominal} = \tan^{-1}(\pi D/P) \quad (6-3)$$

The length of the braid pitch was measured before and after pultrusion by measuring the axial distance of four consecutive yarns. Twenty measurements of the pitch length along the braid axis were recorded for both the braided preform and braid-truded rod. In the case of the model, the pitch length was averaged by measurements of the pitch length of eight yarns. The elongation of the pitch length was calculated by

$$\bar{\varepsilon} = (P_2 - P_1)/P_1 \times 100 \quad (6-4)$$

where P_1 and P_2 are the pitch length of the braid before and after pultrusion. The diameter of the braided preform and braid-truded rod were also recorded by averaging 20 diameter measurements along the braid length, each of which was measured three times (60 measurements). The reduction ratio of the diameter was calculated by

$$\bar{D} = (D_2 - D_1)/D_1 \times 100 \quad (6-5)$$

where D_1 and D_2 were the diameters before and after pultrusion.

6.5.2.2 Mesoscopic scale

The area of the yarn cross-section was averaged over three measurements for each yarn cross-section using the measurement tool in the Dragonfly software. The local fiber volume fraction was calculated using the fraction of the fiber material content of each yarn over the measured yarn cross-section area.

6.5.2.3 Microscopic scale

The fiber-level simulation provided access to the local fiber orientation of the braid using quantification of the orientation of the elements. To quantify the local fiber orientation, the post-processing analysis was conducted using a Python script. To calculate the local orientation of an element, it was assumed that the element was a Euclidean vector between the two nodes' coordinates. Figure 6.8 shows a truss element as a constitutive member of fiber with nodes i and $i+1$ in two coordinates systems of global (Cartesian, xyz) and local (normal-tangent-axial, ntz).

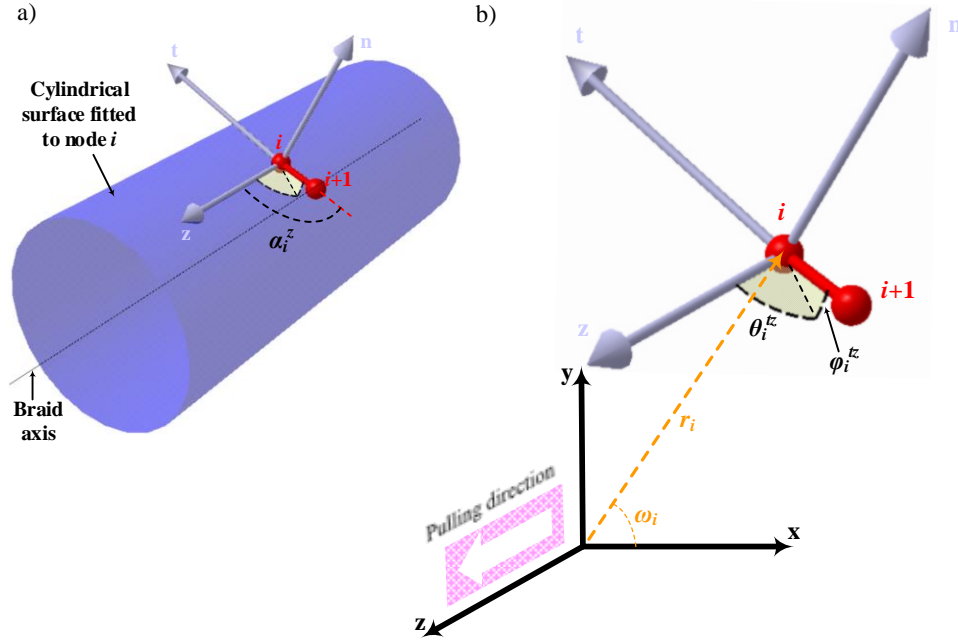


Figure 6.8 Global and local systems and definition of α_i^z , θ_i^{tz} and ϕ_i^{tz} for an element with two nodes of i and $i+1$. (a) A cylindrical surface with the same longitudinal axis with the braid is fitted to node i . The n -coordinate is normal to the cylindrical surface in the radial direction, the z -coordinate is parallel to the longitudinal braid axis, and the tz -plane is the plane tangent to the cylindrical surface. α_i^z is the angle between the element and the z -coordinates. (b) The angle of θ_i^{tz} is the in-plane angle between the element's projection in the tz -plane and z -coordinate. The angle of ϕ_i^{tz} is the out-of-plane angle between the element and its projection in the tz -plane. r_i and ω_i determine the position of the origin of the local coordinates related to the global coordinates.

In the xyz coordinate system, the element vector is expressed using the global coordinates of the element nodes i and $i + 1$ through Eq. (6-6),

$$\vec{V}_i^{xyz} = \begin{bmatrix} V_i^x \\ V_i^y \\ V_i^z \end{bmatrix}, \text{ with } V_i^x = (x_{i+1} - x_i), V_i^y = (y_{i+1} - y_i), V_i^z = (z_{i+1} - z_i) \quad (6-6)$$

The element orientation with respect to the z -axis (braid axis) was calculated by the direction cosine, according to Eq. (6-7),

$$\alpha_i^z = \cos^{-1} \left(\frac{V_i^z}{|\vec{V}_i^{xyz}|} \right) \quad (6-7)$$

The braided preform and braid-truded rod had a cylindrical shape. Therefore, as shown in Figure 6.8, the in-plane and out-of-plane angles were calculated with respect to the tz -plane that was tangent to node i and perpendicular to the radius of node i (\vec{r}_i). The origin of the normal-tangent local system was also attached to node i with identical z -axis to the global system. The n -axis (normal-axis) was in the cylinder radial direction and t -axis (tangent-axis) was hence determined by the right-hand rule and tangent to the cylinder surface. The element vector in the ntz coordinate system can be expressed by Eq. (6-8),

$$\vec{V}_i^{ntz} = \begin{bmatrix} V_i^n \\ V_i^t \\ V_i^z \end{bmatrix}, \text{ with } V_i^n = (n_{i+1} - n_i), V_i^t = (t_{i+1} - t_i), V_i^z = (z_{i+1} - z_i) \quad (6-8)$$

The description of vector \vec{V}_i^{xyz} with respect to global coordinates was known; therefore, the description of the same vector with respect to the local system (\vec{V}_i^{ntz}) was computed using Eq. (6-9),

$$\vec{V}_i^{ntz} = [R_z(\omega_i)]^{-1} \vec{V}_i^{xyz} \quad (6-9)$$

where $R_z(\omega_i)$ is a mapping rotation about the z -axis by ω_i degrees as expressed by Eq. (6-10),

$$R_z(\omega_i) = \begin{bmatrix} \cos \omega_i & -\sin \omega_i & 0 \\ \sin \omega_i & \cos \omega_i & 0 \\ 0 & 0 & 1 \end{bmatrix} \quad (6-10)$$

The in-plane (θ_i^{tz}) and the out-of-plane (ϕ_i^{tz}) angles were calculated with respect to the tz -plane as explained in Eqs. (6-11) and (6-12),

$$\theta_i^{tz} = \tan^{-1} \left(\frac{V_i^t}{V_i^z} \right) \quad (6-11)$$

$$\varphi_i^{tz} = \sin^{-1} \left(\frac{V_i^n}{|V_i^{ntz}|} \right) \quad (6-12)$$

Absolute values of the fiber orientation were calculated for all cases.

6.6 Results and Discussion

The model's initial pitch length and outer diameter were determined by trial and error to achieve the expected final deformed pitch length of the actual braided preform. The following values were set as the input for the Python script to generate the initial geometry of the braid: the regular braid pattern contained 8 yarns with an initial pitch length of $P_0 = 38.5$ mm and an initial outer diameter of $D_0 = 17$ mm for both the braided preform and the braid for pultrusion process simulation.

6.6.1 Macroscopic analysis

Figure 6.9 indicates macroscopic comparison analysis between the model and experimental data for both the braided preform before the pultrusion process and the braid-truded rod. Figure 6.9a shows that the predicted pitch length of 51.0 ± 0.3 mm for the braided preform was comparable with the experimental measurement of 51.0 ± 2.4 mm. After the pultrusion process, the pitch length of 54.9 ± 0.5 mm was predicted, and then compared to the experimental data of 55.4 ± 1.5 mm in Figure 6.9a. Figure 6.9b validates the braid diameter prediction. A braided preform diameter of 8.4 ± 0.5 mm was achieved by the model compared with the measured braided preform diameter of 8.6 ± 0.9 mm. After pultrusion, the predicted braid-truded rod diameter of 4.7 ± 0.1 mm fully matched the experimental measurement of 4.8 ± 0.0 . This close agreement and low measurement standard deviation is expected since in both cases, the geometry is constrained by tooling surfaces. Figure 6.9c validates the nominal braid angle using the obtained braid diameter and pitch length through Eq. (6-3). The model predicted the nominal angle of 27.4° for the braided preform, compared to the nominal angle calculated using the experimental data of 27.9° . Moreover, the prediction of nominal braid angle remained accurate even for the braid-truded rod with the

predicted angle of 15.1° compared to the fiber angle of 14.9° calculated from the experimental data. Figure 6.9d illustrates the variations of the braid geometry after the pultrusion process. Pultrusion elongated the pitch length by 8.6% based on the experimental data, compared to the elongation of 7.6% predicted by the model. During pultrusion, the biaxial braid was submitted to a pulling force ranging from 200 to 400N, measured by the load cell installed on the pultrusion system. The braid diameter was also constrained by the pultrusion die tooling surfaces. This resulted in elongation of the pitch length. The experimental measurements indicated the reduction of braid diameter by 45.3%, closely matched with a 44.0% reduction of the diameter calculated by the model's results. The nominal braid angle was reoriented by 46.5% based on the experimental measurements data. The model predicted the nominal braid angle reduction by 45.0%. Besides the pulling force and the dies dimensional constraints, melting the polymer fibers created more spaces between reinforcement fibers. This space allowed the reinforcement fibers to reorganize and reach a lower braid angle. It is expected that the angle reached is close to the braid lock state (jamming angle). Further inspection of the braid mesostructure will confirm this assumption. The macroscale geometrical quantitative assessment of the braided preform and braid-truded rod revealed excellent agreements between the experimental measurements and the model predictions.

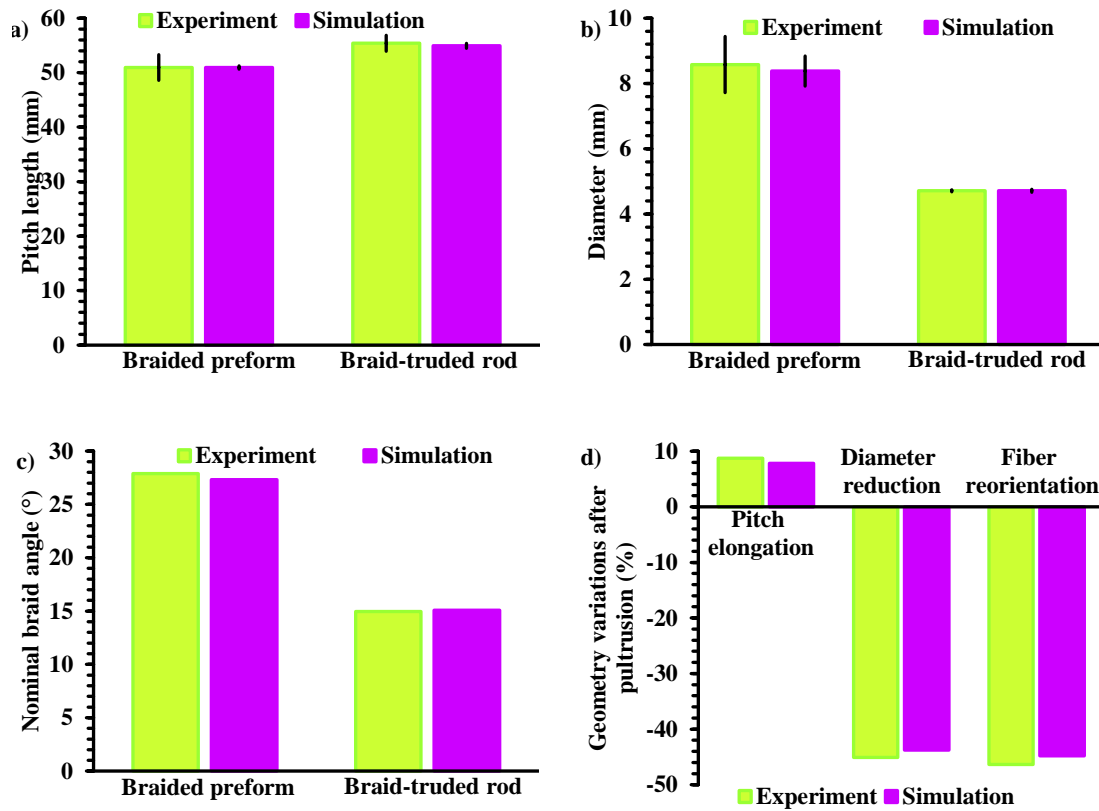


Figure 6.9 Quantitative macroscopic validation of the model before and after pultrusion. Comparison of the pitch length (a), the braid diameter (b), and the nominal braid angle (c). (d) Variations of the braid architecture after pultrusion.

6.6.2 Mesoscopic analysis

Figure 6.10 shows the cross-section of the braid-truded rod captured by an optical microscope. The fibers were well distributed, and a void-free cross-section was obtained. This shows that the resin flow time was sufficient to impregnate the fibers bundles. Resin-rich regions can be observed between yarns where fibers bundles interacted with each other.



Figure 6.10 Cross-section image of the carbon fiber/PEI braid-truded rod.

Figure 6.11 illustrates the quantified mesoscopic morphology of the braid-truded rod cross-sections for comparison between model and experimental data. Figure 6.11a shows two segmented yarns in the 3D CT scan of the braid-truded rod labeled by green (clockwise) and orange (counterclockwise) colors. The accuracy of the segmentation of yarns was evaluated visually by comparing the random slices with the initial images before segmentation. Although a satisfactory accuracy was observed in the segmentation output, small errors were visible such as unsegmented corners of the yarns and mistakenly labeled matrix area. Hence, five errorless segmented slices (I to V) were extracted for quantitative comparisons with equivalent cross-sections of the model (Figure 6.11b). Figure 6.11d exhibits an equivalent 3D portion from the model to extract five equivalent cross-sections for the comparison. Figure 6.11c displays the comparison between the extracted slices of the CT scan and model. Significant similarities were visible between the shape of segmented yarns and the corresponding model images. Although, the use of more fibers in the yarns model may lead to more accurate results.

The quantified areas of the yarn cross-sections corresponding to slices I to V were compared for both clockwise and counterclockwise yarns in Figure 6.12a and Figure 6.12b, respectively. The

averaged area of $2.08 \pm 0.06 \text{ mm}^2$ for five slices closely matched the model's averaged area of $1.97 \pm 0.09 \text{ mm}^2$ with an agreement of 94.88%. The local fiber volume fractions for both segmented yarns were compared with predicted values of the model in Figure 6.12c,d. The local area and fiber volume fraction data slightly varied from slice to slice along the yarn path. These local variations were attributed to the local configuration of the yarn in the braid structure. When all data was pooled, the averaged fiber volume fraction of $57.44\% \pm 1.75$ was calculated by the CT scan data, compared to the averaged volume fraction of $60.61\% \pm 2.85$ predicted by the model with an agreement of 94.49%. The yarns were compacted together in the pultrusion die, which led to a high local fiber volume fraction. This indicates that the braid reached the locked state where the braid angle is jammed. At this state, the pitch cannot elongate more, and the braid angle cannot reduce further.

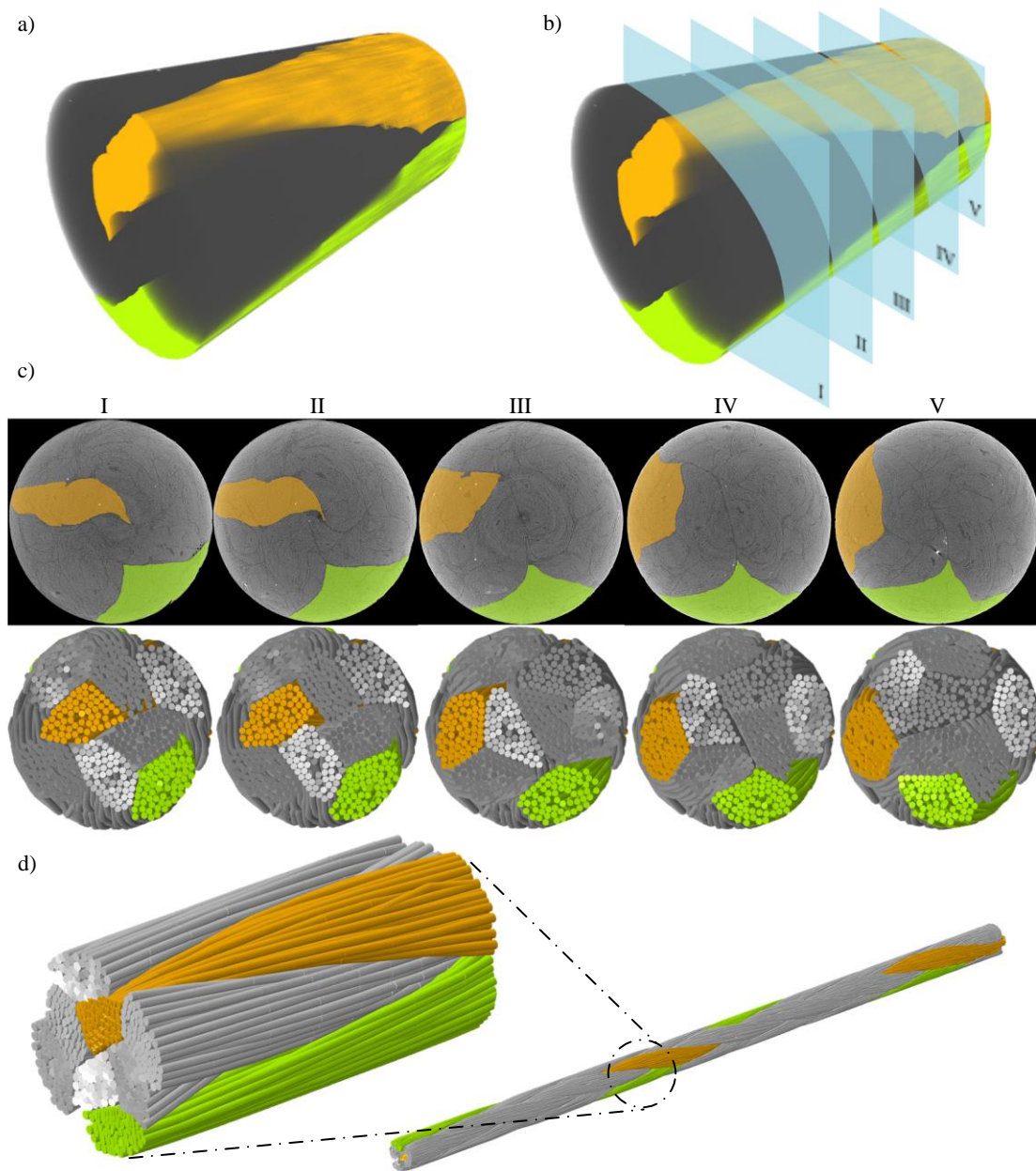


Figure 6.11 (a,b) 3D segmented clockwise (green) and counterclockwise (orange) braided yarns. (c) Comparison of the braid-truded yarns cross-sections morphology between the model and CT images along the yarn path. (d) 3D portion of the model to extract five cross-sections to compare with the equivalent CT images.

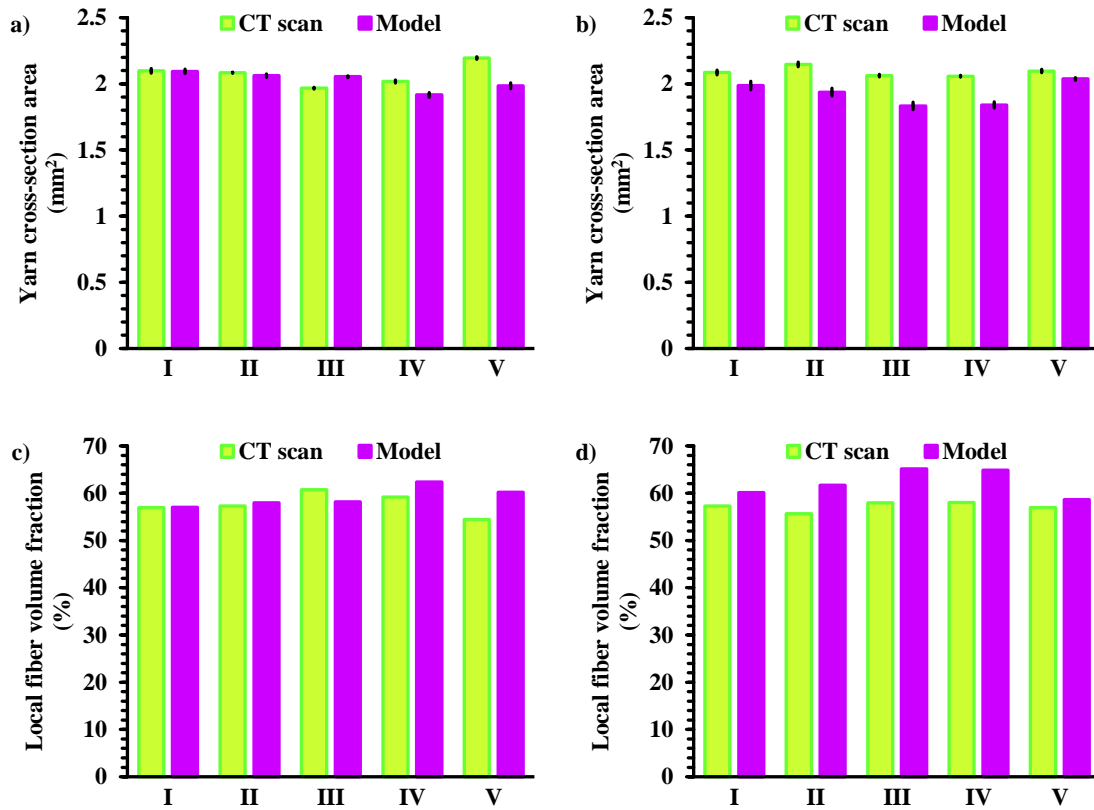


Figure 6.12 Comparison of the yarn cross-section area of the braid-truded rod along the yarn path between the CT data and predicted values for five slices of the clockwise (a) and counterclockwise (b) yarns. Local fiber volume fraction corresponding to the clockwise (c) and counterclockwise (d) yarns along the yarns path.

6.6.3 Microscopic analysis

To validate the prediction of the local fibers orientation, similar slices from the middle of the model and CT scan of the braid-truded rod in the yz -plane were evoked for comparison (Figure 6.13a,d). Figure 6.13b illustrates the slice of the model consisting of 2,000 elements and 4,000 nodes. Figure 6.13c shows a magnification of the fiber distribution of the model's slice. Figure 6.13d represents the equivalent CT slice divided into 60 square portions. In each square portion, three local fiber orientations were manually measured using the angle measurement tool in the Dragonfly software.

For example, Figure 6.13e-g are three portions of the CT slice showing fiber orientation measurements. The mean and standard deviation of the predicted and measured fiber orientations were compared in Table 6.1. The experimental measurements of the fiber orientation of 5.80 ± 5.35 closely matched the predicted 5.33 ± 4.98 of the FE model, demonstrating the high validity of the model. The large standard deviation was also accurately predicted, indicating a scattered distribution of the fibers orientation.

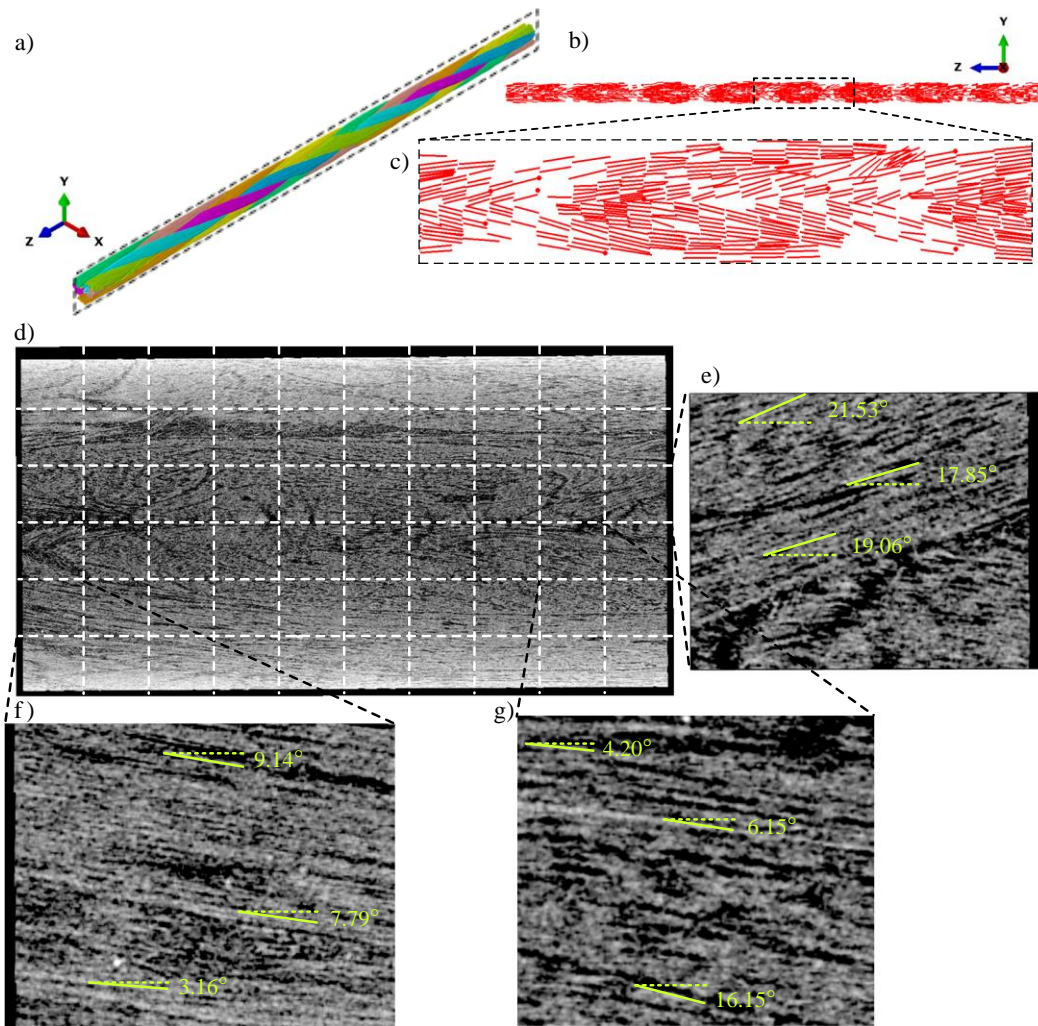


Figure 6.13 Validation of the prediction of the fibers orientation. (a,b) Extracted model's slice from middle of the braid in the yz-plane. (c) Zoomed section of the model's slice showed the fiber distribution. (d) Equivalent CT slice divided 60 portions to measure the fibers orientation. (e-g) Zoomed portions of the CT slice illustrated fiber orientation measurements.

Table 6.1 Validation of the prediction of the in-plane fiber orientation.

	Mean [°]	Standard deviation
Model	5.33	4.98
CT scan	5.80	5.35

The local fiber orientation distributions of the model were visualized using binned scatter plots in Figure 6.14 and Figure 6.15. Each binned scatter plot contained 46,360 local fiber orientation data point records. These plots represent the large data points of fibers orientation grouped into small square cells (pixels) in addition to an aggregated data in each cell. An encoded color bar depicted the count of records, visualizing two terms of distribution and density (concentration) of fibers orientation data points.

Figure 6.14 shows the local fiber orientation along the radius of the braid before and after pultrusion. Figure 6.14 illustrates that the local fiber orientation was not uniformly distributed across the thickness and a significant amount of fibers were oriented around a specific range of angles and radii. Figure 6.14a,b contrast the in-plane fiber orientation distribution between the braided preform and the pultruded braid along the radius. Figure 6.14a visualized that θ^{tz} before pultrusion was concentrated around the domain of 0 - 16°, restricted by radii ranging from 1.2 to 3.2 mm (equal to 27% - 73% of the outer radius) whereas Figure 6.14b visualized that the pultruded braid had a density of θ^{tz} around 0 - 10° within radii ranging from 1.4 to 2.3 mm (equal to 61% - 100% of the outer radius). This indicates a decrease of 6° in the density of in-plane fiber orientation after the pultrusion process. Figure 6.14c,d exhibit the juxtaposition of the distribution of the out-of-plane fiber orientation between the braided preform and the pultruded braid along the radius. Figure 6.14c unveiled that a considerable amount of fibers before pultrusion were oriented around the domain of 0 - 16°, encircled by radii ranging from 1.5 to 3 mm (equal to 35% - 70% of the outer radius) whilst Figure 6.14d visualized that the out-of-plane braid angle φ^{tz} after pultrusion was concentrated around 0 - 10°, surrounded by radii ranging from 1.3 to 2.3 mm (equal to 57% - 100%

of the outer radius). This indicates a decrease of 6° in the density of out-of-plane fiber orientation after the pultrusion process.

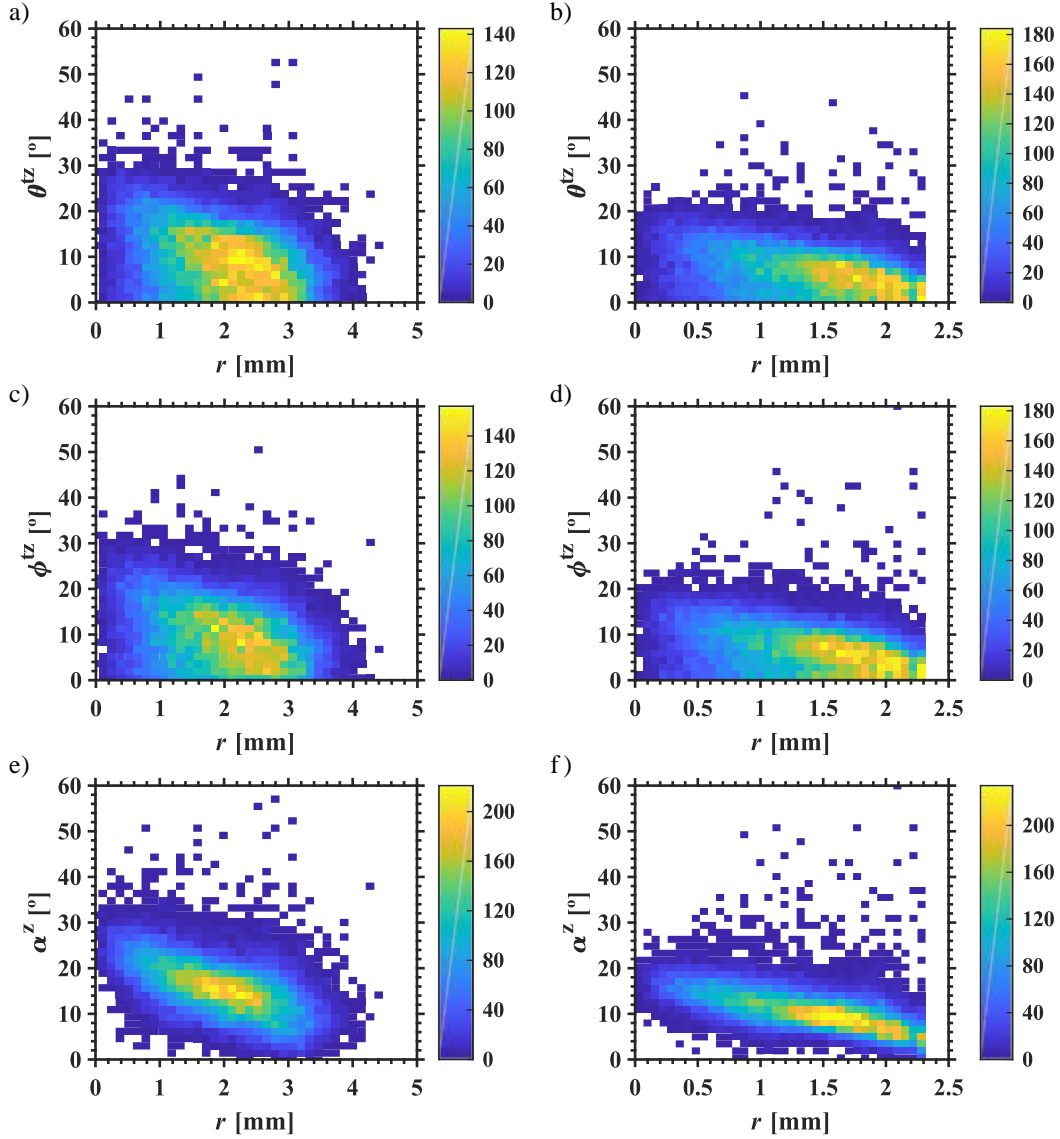


Figure 6.14 Distribution of the in-plane fiber orientation along the radius for the braided preform (a) and pultruded braid (b). Distribution of the out-of-plane fibers orientation along the radius for the braided preform (c) and pultruded braid (d). Distribution of the fibers orientation with respect to the z-axis along the radius for the braided preform (e) and pultruded braid (f).

Figure 6.14e,f compares the distribution of the fiber orientation with respect to the z-axis (longitudinal braid axis) between the braided preform and the pultruded braid along the radius. Figure 6.14e illustrated that α^z before pultrusion was concentrated around the domain of 10 - 20°, enclosed by radii ranging from 1.3 to 2.6 mm (equal to 30% - 59% of the outer radius) whilst Figure 6.14f visualized that the pultruded braid had a density of α^z around 5 - 12° within radii ranging from 1.3 to 2.3 mm (equal to 57% - 100% of the outer radius). These results indicate that the pultrusion process reduced the density of fiber orientation with respect to z-axis by a range of 5 - 8°.

The mean of θ^{tz} , φ^{tz} , and α^z , obtained in the microscopic analysis, was compared with $\alpha_{nominal}$ from the macroscopic analysis. Table 6.2 lists the mean values with their standard deviation for both the braided preform and the pultruded braid. It should be noted that the large standard deviations in Table 6.2 expressed the wide dispersion of the distribution of the fiber orientation. The mean of θ^{tz} , φ^{tz} , and α^z were much lower than $\alpha_{nominal}$. The differences between $\alpha_{nominal}$ and θ^{tz} , φ^{tz} , and α^z before pultrusion were 18.5°, 18.6°, and 11.7° and after pultrusion were 8.5°, 8.14°, and 4.3°, respectively. There were considerable discrepancies between the local fiber orientation and the nominal braid angles. The nominal braid angle was calculated using the outer diameter in Eq. (6-3). These significant discrepancies invalidate the assumption that the nominal braid angle represents the local fiber orientation. It is expected that this lack of validation is greater for small diameter braids such as the one pultruded herein. The microscopic analyses of the local fiber orientation (Figure 6.14a-f) also revealed that the local fiber orientation of biaxial braids varied along the braid radius so that the fiber orientation was concentrated within a certain magnitude of radius. This behavior can be explained by the fact that there was no core (mandrel or filler) inside the braid, so the braided yarns were collapsed on themselves, causing yarn compression and reducing the angle of fibers. In the case of the existence of the core, the core will apply outward radial pressure on the braided yarns, spreading the yarns on the core and closer to the external diameter. This will result in having local fiber orientations close to the nominal braid angle.

Table 6.2. Comparison of the mean of local fiber orientations with the nominal braid angle.

	Braided preform		Braid-truded rod	
	Mean	Standard deviation	Mean	Standard deviation
θ^{tz} [°]	8.84	5.85	6.60	4.43
φ^{tz} [°]	8.78	5.78	6.54	4.45
α^z [°]	15.68	7.27	10.76	7.61
$\alpha_{nominal}$ [°]	27.4	-	15.1	-

Figure 6.15 demonstrate the correlation between the local fiber orientation and the pitch length for both the braided preform (Figure 6.15a,c,e) and the pultruded braid (Figure 6.14b,d,f). The distribution of θ^{tz} , φ^{tz} , and α^z along the pitch length were compared before and after pultrusion in Figure 6.15a,b, Figure 6.15c,d, and Figure 6.15e,f, respectively. These figures confirmed the distribution and density of the fiber orientation explained by Figure 6.14 a-f. However, in contrast to the fiber orientation distribution along the braid radius, Figure 6.15 depicted uniform fiber orientation distribution along the pitch length. Hence, distributions of θ^{tz} , φ^{tz} , and α^z were hardly influenced by the pitch length of braids.

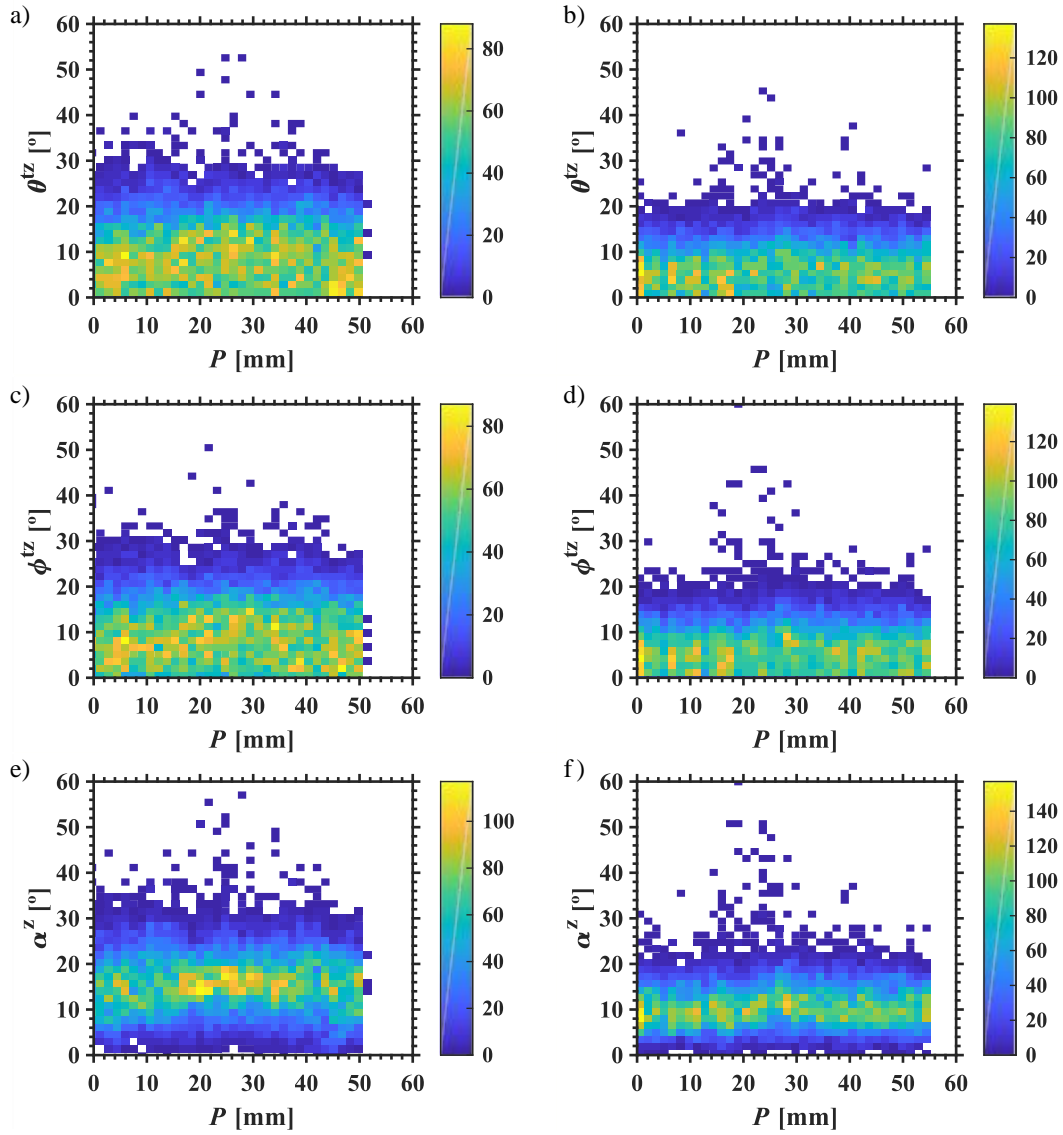


Figure 6.15 Distribution of the in-plane fiber orientation along the pitch length for the braided preform (a) and pultruded braid (b). Distribution of the out-of-plane fibers orientation along the pitch length for the braided preform (c) and pultruded braid (d). Distribution of the fibers orientation with respect to the z-axis along the pitch length for the braided preform (e) and pultruded braid (f).

6.7 Conclusion

A multiscale numerical model was presented to simulate the forming process of biaxial braids during the thermoplastic braid-trusion process. The modeling approach used discrete fibers made of chains of truss elements. Those fibers were bundled into yarns. Eight yarns were assembled to form a regular rope braid configuration that was virtually pultruded. The same braid configuration was experimentally pultruded using carbon fiber/PEI yarns. It was observed that the pultrusion process changed the braid architecture similarly in the simulation and reality. The simulation prediction of 7.6% pitch elongation, 44.0% diameter reduction, and 45.0% reorientation of the nominal braid angle after pultrusion had excellent agreement with macro-scale measurements over the braid-truded rod. For mesoscopic morphology characterization, the prediction of yarns cross-section area and local fiber volume fraction of the braid-truded yarns were compared with the quantified micro CT scan data, which closely matched with an agreement of 95%. The micro-scale analysis visualized three distributions of the local fiber orientation of in-plane, out-of-plane, and the angle with respect to the longitudinal braid axis. Remarkably, distributions of the local fiber orientation varied along the braid radius. Indeed, the fibers were oriented within a certain range of radius around 30 – 70% and 60 – 100% of the outer radius before and after pultrusion, respectively. Conversely, distributions of the local fiber orientation were uniform along the pitch length. Moreover, there were notable discrepancies between the local fiber orientation and the nominal braid angles, which invalidated the hypothesis that the nominal braid angle described the local fiber orientation for small, rope-like braids.

The results presented herein gives insights on the multiscale morphology of braid-truded composites supported by experimental data. This braid-trusion modeling methodology will soon be used to study the effects of inter-fibers and fibers-to-die wall friction on the morphology, and most importantly, the pulling force required. While the yarn twist was negligible in the experiment reported here, the effects of yarn twist can be included in future studies. Finally, the results have also shown that the morphology predictions were accurate for these specific braid-trusion conditions even if the polymer flow effects were not considered. However, this assumption may not be accurate for all polymer properties, pultrusion conditions and braid architectures. The

viscous polymer flow effects will also be investigated in future studies to determine its influence on the morphology and the pulling force.

Acknowledgments

This work was supported by the Bombardier Aviation; the Natural Science and Engineering Research Council of Canada (NSERC) [CRDPJ488387-15]; the Advanced Materials Research and Innovation Hub PRIMA Québec [R10-009]; and the Pultrusion Technique Inc. The authors would like to express their gratitude to Marie-Hélène Bernier for CT scans.

CHAPTER 7 GENERAL DISCUSSION

7.1 General discussion on published achievements

Although biaxial braids in thermoplastic braid-truded composites can benefit from the high formability of reinforcements through a thermoforming process, a comprehensive investigation on the use of biaxial braids in thermoplastic braid-trusion has not been reported in surveyed works. In this thesis, we studied the use of biaxial braids in thermoplastic braid-trusion to manufacture composites rods. To design the manufacturing process, a simple geometry-based method was proposed to produce braid-truded rods using commingled fibers and a multi-die pultrusion system.

One of the major barriers to transfer the thermoplastic braid-trusion technique into a mass production process in the composites market is the absence of simulation to perceive the sophisticated deformation of the braid during the pultrusion process. In this thesis, we introduced a numerical simulation methodology for the forming process of biaxial braids during the thermoplastic braid-trusion process. To this end, a realistic biaxial braid was simulated using a quasi-static finite element framework, shown a high level of accuracy in quantitative comparisons with CT scan data. In this approach, braided yarns were modeled as a bundles of discrete fibers in which chains of truss elements simulated the flexibility of fibers. The fiber-level model allowed analyses of the effects of inter-fibers friction on the internal geometry, jamming state, and crimp of braids. We took advantage of the proposed braid model to simulate the forming process of biaxial braids during thermoplastic braid-trusion by passing the pultrusion die over the braided preform. To the best of our knowledge, this is the first modeling methodology that is able to predict the braid's geometry in macro, meso, and micro scales before and after pultrusion. We also devised a cutting-edge solution for the local fiber orientation distribution using the innovative fiber-level model.

7.2 General discussion on unpublished achievements

7.2.1 Inter-fibers frictions effects

In this section, the inter-fibers friction was investigated for the model developed in Chapter 6. Figure 7.1-7.3 illustrate the local fiber orientation distribution with three coefficients of friction of $\mu = 0.1, 0.4$, and 0.6 for the inter-fibers contact and the contact between fibers and the die wall. The comparisons showed that changing the inter-fibers coefficient of friction slightly affected the local fiber orientation distribution. The range of distributions and densities of the local fiber orientation along the braid radius become relatively wider by increasing the coefficient of friction for θ^{tz} (Figure 7.1), φ^{tz} (Figure 7.2), and α^z (Figure 7.3). To closer evaluate the effect of the coefficient of friction on the local fiber orientation, the mean and standard deviation (SD) of the local angles corresponding to Figure 7.1 to Figure 7.3 were listed in Table 7.1. The results in Table 6.1 can also be presented in the form of vertical bar graphs, as shown in Figure 7.4. Figure 7.4 illustrates that the increase in the coefficient of friction from 0.1 to 0.4, 0.4 to 0.6, and 0.1 to 0.6 slightly influenced the mean of local fiber orientation with 13%, 3%, and 16% increases, respectively.

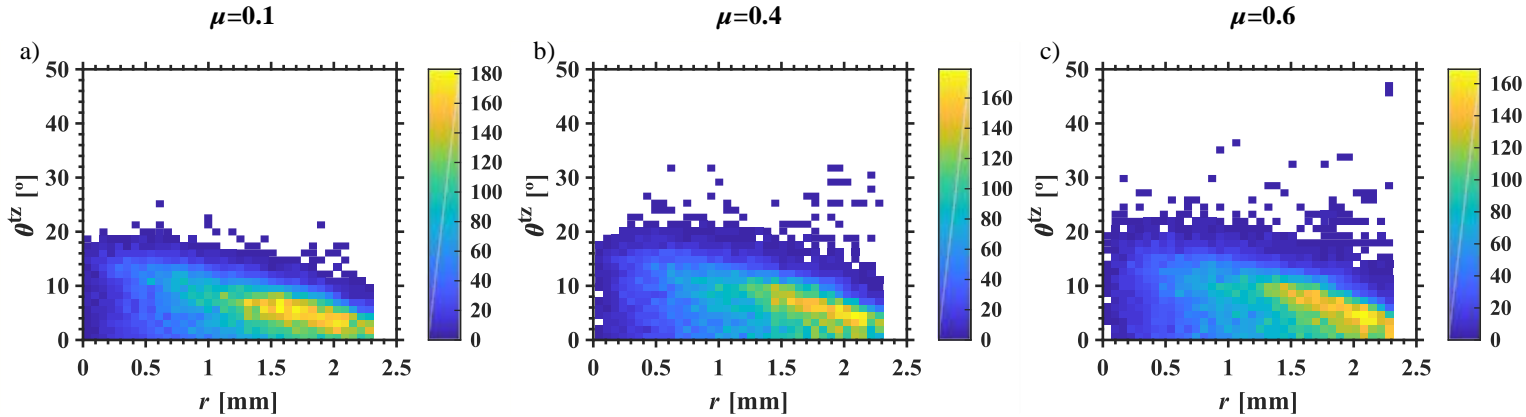


Figure 7.1 Effect of coefficients of friction on the in-plane fiber orientation distribution. Distribution of θ^{tz} along the braid radius for $\mu = 0.1$ (a), $\mu = 0.4$ (b), and $\mu = 0.6$ (c).

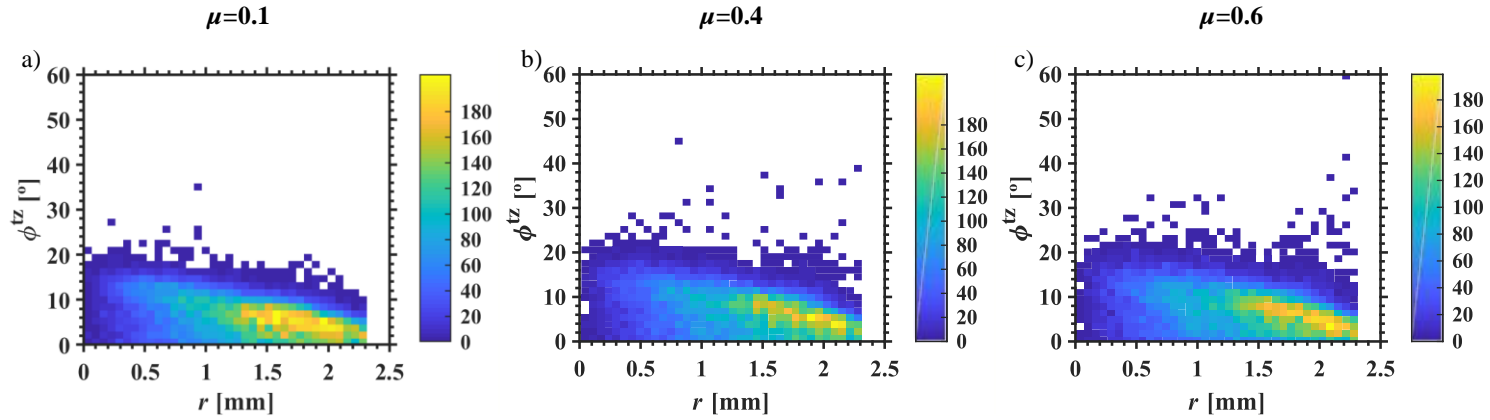


Figure 7.2 Effect of inter-fibers friction on the out-of-plane fiber orientation distribution. Distribution of ϕ^{tz} along the braid radius for $\mu = 0.1$ (a), $\mu = 0.4$ (b), and $\mu = 0.6$ (c).

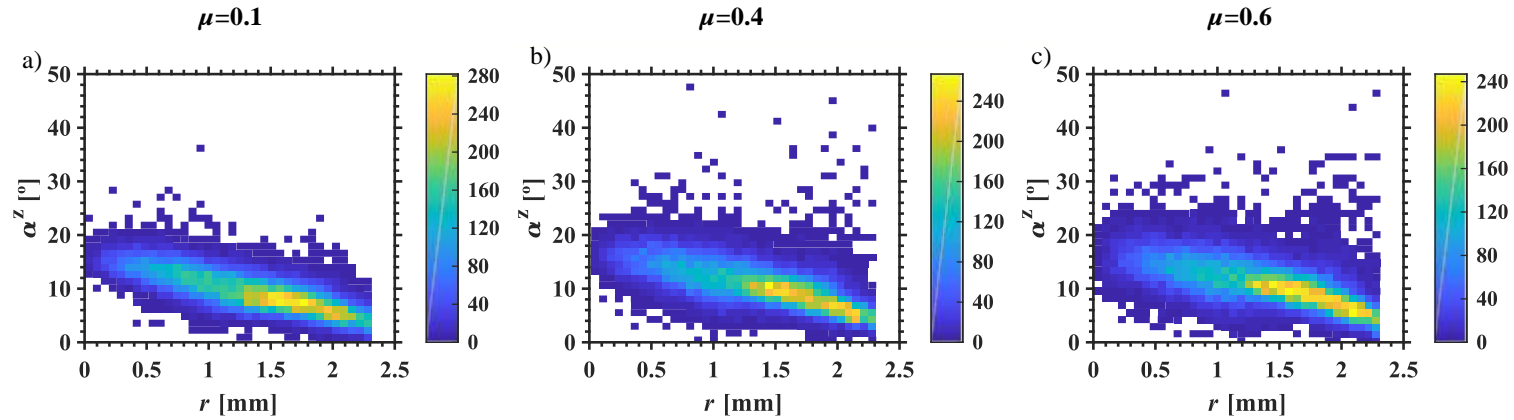


Figure 7.3 Effect of coefficients of friction on the local fiber orientation distribution with respect to the braid's longitudinal axis. Distribution of α^z along the braid radius for $\mu = 0.1$ (a), $\mu = 0.4$ (b), and $\mu = 0.6$ (c).

Table 7.1 Effect of the inter-fibers coefficient of friction on the local fiber orientation.

	$\mu=0.1$		$\mu=0.4$		$\mu=0.6$	
	Mean	SD	Mean	SD	Mean	SD
θ^{tz} [°]	6.04	4.01	6.80	6.83	7.00	6.06
φ^{tz} [°]	6.01	5.24	6.80	6.76	6.95	6.74
α^z [°]	9.45	4.41	10.66	6.99	10.94	6.66

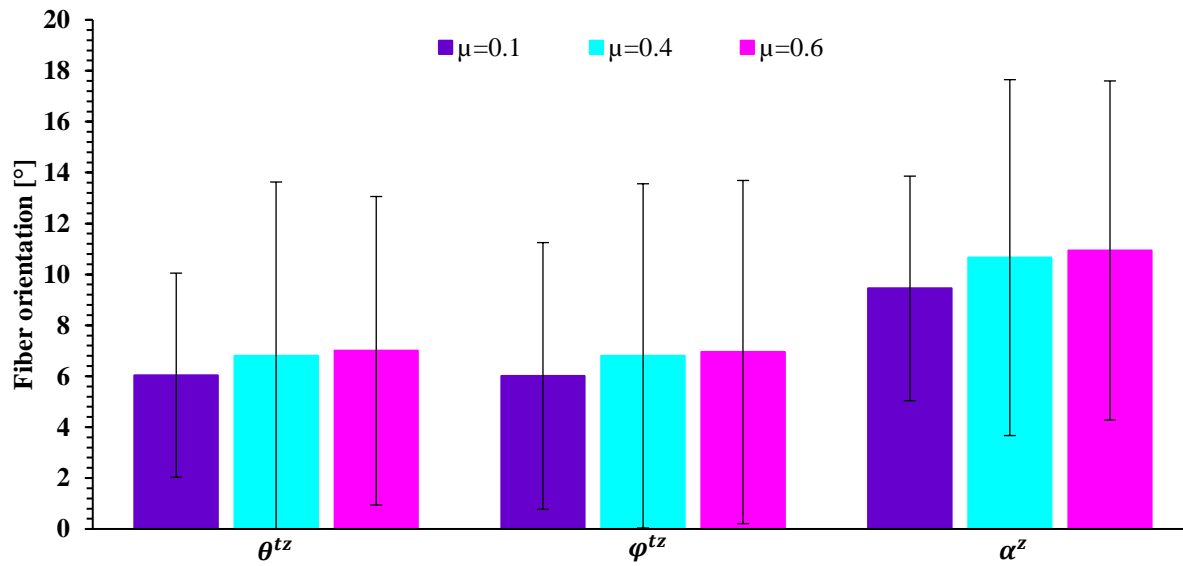


Figure 7.4 Effect of the inter-fibers coefficient of friction on the local fiber orientation.

Figure 7.4 shows that the standard deviations in the entire population of angles are wide and much larger than the difference between the averages for each orientation classification. This indicates that the coefficient of friction has a limited effect on the orientation of the fibers. Therefore, it can be confirmed that for the conditions modeled, the fiber orientation is mostly driven by contacts between solids.

7.2.2 Friction effects between fibers and the die wall

In this section, the friction between braided fibers and the die wall was analyzed for the model developed in Chapter 6. Figure 7.5 to Figure 7.7 illustrate the local fiber orientation distribution with three coefficients of friction for the contact between fibers and the die wall ($\mu = 0.1, 0.4$, and 0.6) while the fiber-to-fiber coefficient of friction of $\mu_f = 0.3$ was kept for the three simulations. The comparisons showed that changing the coefficient of friction of the contact between fibers and the die wall hardly affected the distribution of θ^{tz} (Figure 7.5), φ^{tz} (Figure 7.6), α^z (Figure 7.7). To inspect more carefully, the mean and standard deviation of the local angles corresponding to Figure 7.5 to Figure 7.7 were listed in Table 7.2 and Figure 7.8. Figure 7.8 shows that the variation of the coefficient of friction between fibers and the die wall had an insignificant impact on the mean of local fiber orientations.

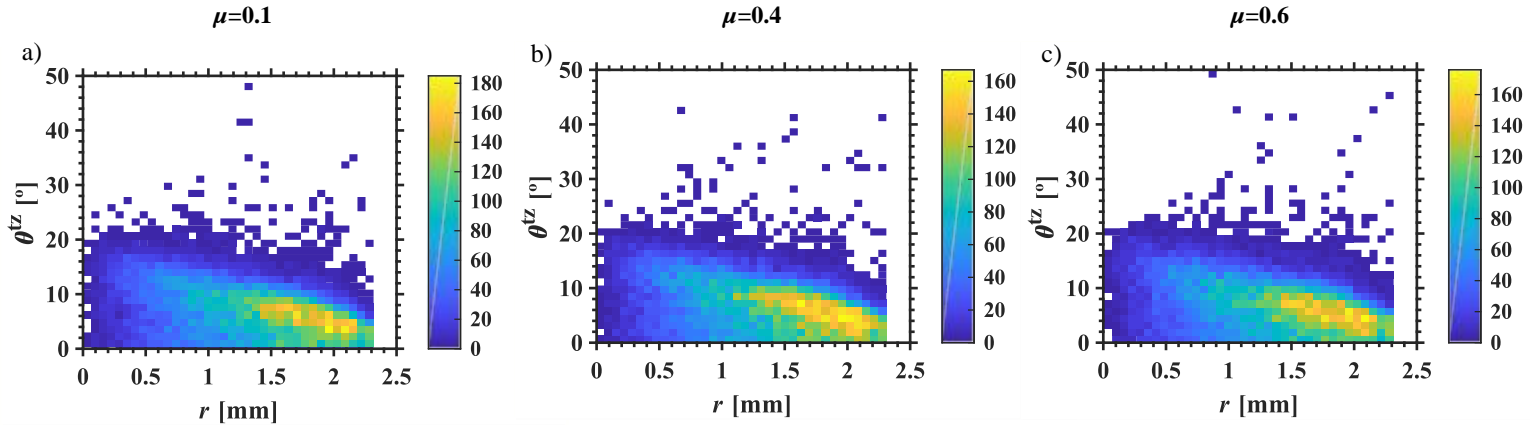


Figure 7.5 Effect of friction between fibers and the die wall on the in-plane local fiber orientation distribution. Distribution of θ^{tz} along the braid radius for $\mu = 0.1$ (a), $\mu = 0.4$ (b), and $\mu = 0.6$ (c).

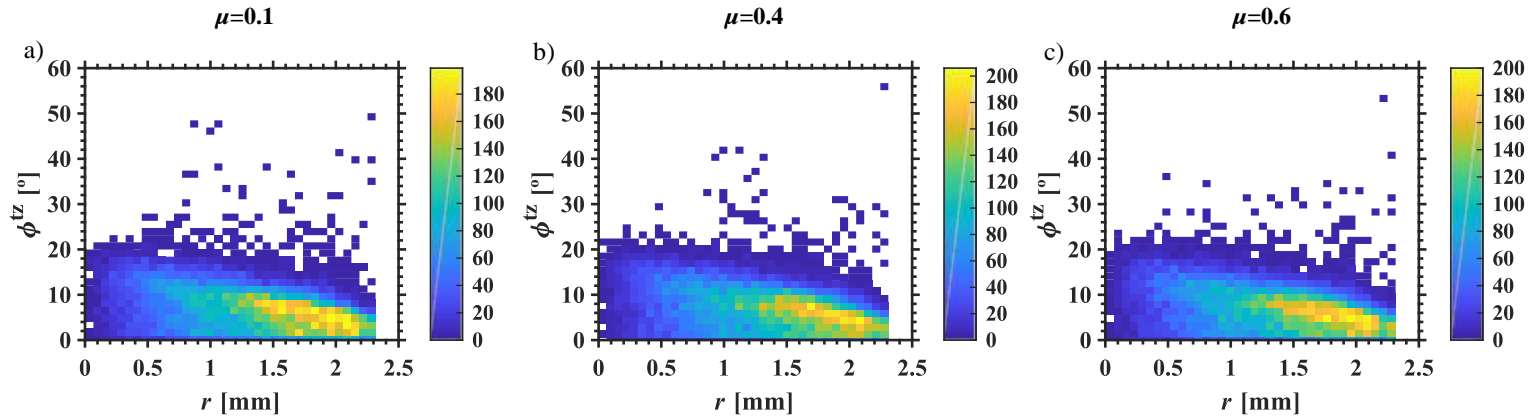


Figure 7.6 Effect of friction between fibers and the die wall on the out-of-plane local fiber orientation distribution. Distribution of φ^{tz} along the braid radius for $\mu = 0.1$ (a), $\mu = 0.4$ (b), and $\mu = 0.6$ (c).

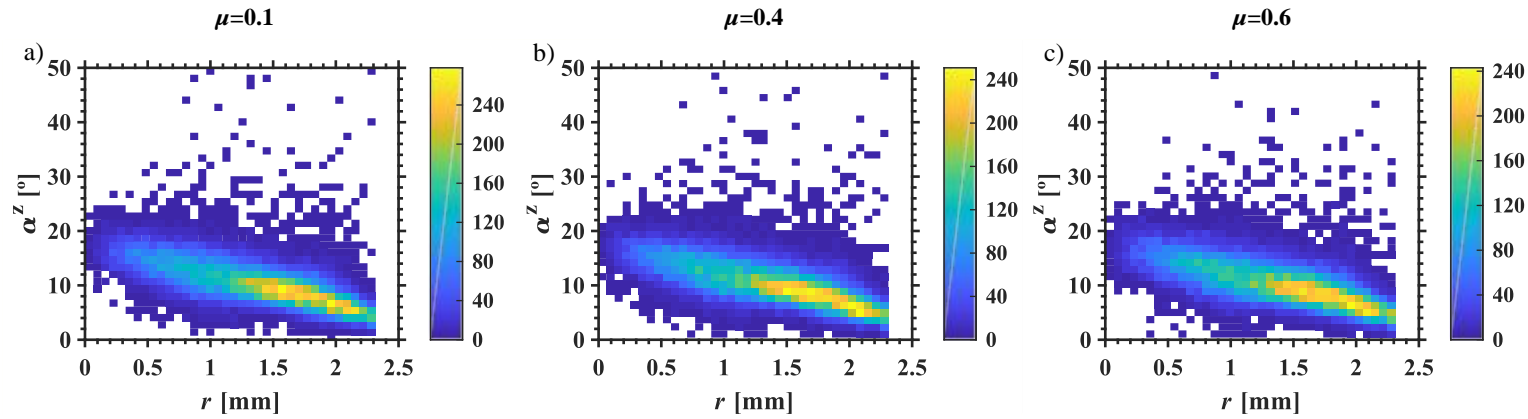


Figure 7.7 Effect of friction between fibers and the die wall on the local fiber orientation distribution with respect to the braid's longitudinal axis. Distribution of α^z along the braid radius for $\mu = 0.1$ (a), $\mu = 0.4$ (b), and $\mu = 0.6$ (c).

Table 7.2 Effect of the coefficient of friction between braided fibers and the die wall on the local fiber orientations.

	$\mu=0.1$		$\mu=0.4$		$\mu=0.6$	
	Mean	SD	Mean	SD	Mean	SD
θ^{tz} [°]	6.23	4.08	6.20	4.08	6.35	4.25
φ^{tz} [°]	6.19	4.08	6.20	4.08	6.34	4.18
α^z [°]	10.52	7.67	10.55	7.55	10.57	7.72

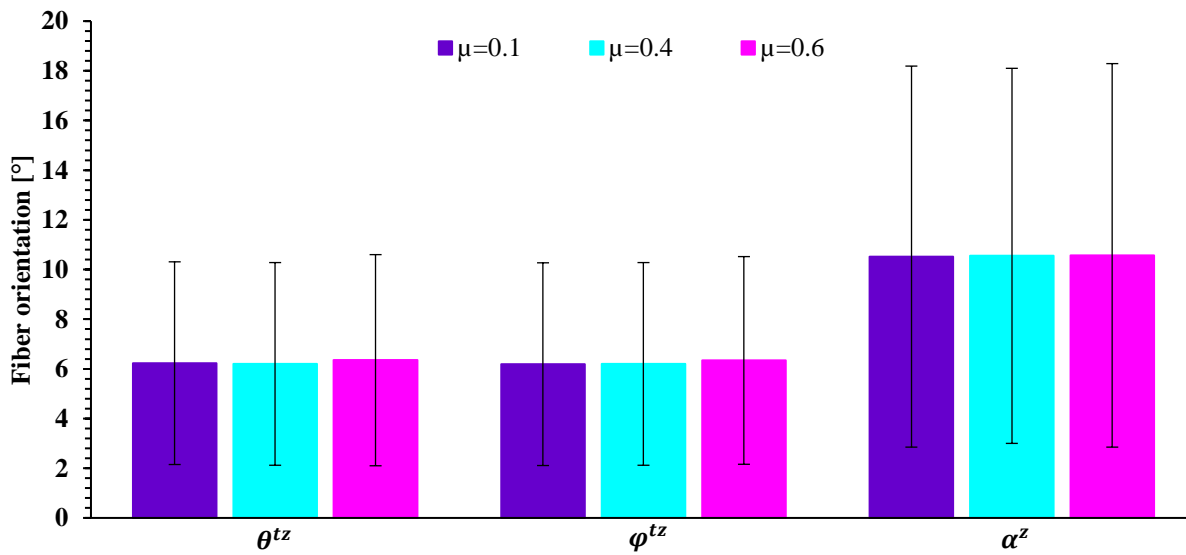


Figure 7.8 Effect of the coefficient of friction between braided fibers and the die wall on the local fiber orientations.

Figure 7.9 shows the frictional dissipated energy curves against the displacement of the braid inside the die for the three coefficients of friction. As shown in Figure 7.9, the frictional dissipated energy increased with increasing the coefficient of friction between fibers and the die wall. All curves had the same behavior when the braid passed through the tapered zone. The frictional dissipated energy increased nonlinearly as fibers contacted the tapered zone's die wall. However, as soon as the braid left the tapered zone, both processes with the low and medium coefficients of friction ($\mu =$

0.1 and 0.4) behaved differently from the process with the high coefficient of friction ($\mu = 0.6$). In those instances of low and medium coefficients of friction ($\mu = 0.1$ and 0.4), the frictional dissipated energy remained almost constant when the braid was fully entered into the cylindrical zone. On the contrary, the frictional dissipated energy of the process with the high coefficient of friction ($\mu = 0.6$) linearly increased when the braid was passed through the cylindrical zone. This behavior indicated that contact forces between fibers and the die wall became low and there were no considerable contact forces variations for both cases of the low and medium coefficients of friction. Conversely, in the case of the high coefficient of friction, the contact forces between fibers and the die wall remained constantly high during pultrusion. This high-level of contact forces can be dangerous for the thermoplastic pultrusion and eventually may terminate the process. Two appropriate examples of this are the damage of fibers during pultrusion and the improper design of braid for the process, which have been experimentally investigated for unidirectional thermoplastic pultrusion [88] and triaxial braid-trusion [4]. In these studies, the damaged fibers and excess filling of the pultrusion dies escalated the frictional resistance against the pulling force during pultrusion and led to a sudden interruption of the process.

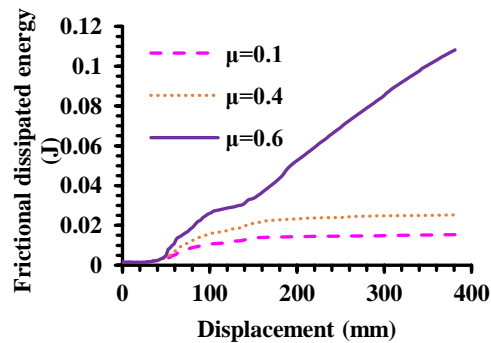


Figure 7.9 Effect of coefficient of friction between fibers and the die wall on the frictional dissipated energy.

CHAPTER 8 CONCLUSION AND RECOMMENDATION

8.1 Contribution

In Chapter 4, we addressed the issue of the use of biaxial braids to manufacture thermoplastic composites using the braid-trusion technique. Since the biaxial braid has an unstable structure under tension, most previous works used triaxial braids as reinforcements in the thermoplastic braid-trusion technique because axial yarns in triaxial braids stabilize their structure. In this study, a simple geometry-based method was proposed to design the manufacturing process of thermoplastic biaxial braid-trusion. A thermoplastic biaxial braid-truded rod was successfully manufactured according to the proposed design method using carbon fiber/PEI commingled fibers. The variation of three spool tensions of 2.5, 40, and 80 N was investigated. We found that the spool tension had a significant effect on the impregnation and void content of thermoplastic braid-truded rods. The void-free rod's cross-section was achieved by the experiment with the minimum spool tension of 2.5 N, while the void content was increased by increasing the spool tension. This behavior indicated that raising the spool tension condenses the carbon fiber bundles and reduces the permeability. To evaluate the impact of processing speed, two experiments were conducted with moderately low speed of 50 mm/min and moderately high speed of 150 mm/min. The 150 mm/min process illustrated a slightly higher amount of voids as the resin flow time was too short to allow the impregnation of fiber bundles. The smooth surface of the rod manufactured with 50 mm/min processing speed was also roughed after accelerating the process. The reason was the hot molten thermoplastic materials had less time to deconsolidate appropriately. The effect of cooling die temperature on the surface finish of the rod was explored by varying three temperatures of T_g , $T_g/2$, and $T_g/4$. We found that the decrease in the cooling die temperature from T_g to $T_g/2$ resulted in a higher surface finish quality. However, dropping the temperature from $T_g/2$ to $T_g/4$ had an insignificant effect on the surface finish of the braid-truded rod. This indicated that faster cooling and shrinkage of the rod in the cooling die were occurred by the lower cooling temperatures. Indeed, the rod shrunk and debonded faster from the cooling die surface at $T_g/2$ and $T_g/4$.

In Chapter 5, we developed a fiber-level modeling methodology to simulate biaxial braids. Although the geometry-based design proposed in Chapter 4 had advantages of simplicity and ease of use, it neglected inter-fibers mechanical interactions and frictional contact between fibers and

the die wall. Furthermore, it was unable to predict the multiscale geometry of braids. To compensate for these deficiencies, we took advantage of the fiber-level FE model of 1/1 and 2/2 braids in which the braided yarn was simulated as a bundle of discrete fibers using truss elements. The proposed methodology was validated using a comprehensive quantitative comparison with micro CT scans of braided carbon fibers. To confirm the hypothesis that the inter-fibers contact remarkably contributes to the jammed state phenomenon, we scrutinized the correlation between the frictional dissipated energy of braids and the jammed state phenomenon through the fiber-level model. We found that inter-fibers friction had a considerable effect on the shape of braided yarns and their aspect ratio. The increase in the coefficient of friction from 0.1 to 0.6 affected the shape of yarn cross-section with 52.77% increases in the yarn's aspect ratio. However, insignificant changes in the jamming angle and the yarn's crimp were observed with increasing the coefficient of friction. We also showed that changing the modulus of elasticity hardly affected the jamming angle, yarn aspect ratio, yarn cross-sectional shape, and yarn's crimp in the jammed state.

In Chapter 6, we took the advantage of the model developed in Chapter 5 to simulate the forming process of the biaxial braids during thermoplastic braid-trusion. The multiscale braid-trusion model provided a comprehensive understanding of the complex deformation of biaxial braids during the process. A regular braid with discrete fibers was modeled, and then it was virtually pultruded. The same carbon fiber/PEI braid configuration was fabricated and experimentally pultruded. It was distinguished that the pultrusion process significantly changed the braid architecture similarly in both virtual and reality experiment at the macro scale. The model predicted a 7.6% pitch elongation, a 44.0% diameter reduction, and a 45.0% reorientation of the nominal braid angle after pultrusion, which had excellent agreements with experimentally measurements. The model predicted the internal geometry, mesoscopic morphology, and local fiber volume fraction of braid-truded yarns, which matched the CT data with an agreement of 95%. The fiber-level braid model provided access to the local fiber orientation distribution. We illustrated that the local fiber orientation of biaxial braids varied along the braid radius so that the fiber orientation was aggregated within a certain magnitude of radius, which was about 30 – 70% and 60 – 100% of the outer radius of the braid before and after pultrusion, respectively. Conversely, the local fiber orientation along the pitch length was uniformly distributed. The model also demonstrated significant discrepancies between

the local fiber orientation and the nominal braid angles. These considerable differences invalidate the assumption that the nominal braid angle represents the local fiber orientation.

In Chapter 7, the friction between fibers and the die wall was examined for the model developed in Chapter 6. The inter-fibers coefficient of friction has a limited impact on the local fibers' angle. Thus, it can be confirmed that the fiber orientation is mostly obtained by contacts between solids for the modeled conditions. Also the increase in the coefficient of friction between fibers and the die wall ranging from low (0.1) to high (0.6) hardly affected the local fiber orientation, whilst their frictional dissipated energy behaved differently. The processes with low (0.1) and moderate (0.4) coefficients of friction had approximately constant frictional dissipated energy, whereas the frictional dissipated energy linearly increased during pultrusion for the process with the high coefficient of friction (0.6). Although an insignificant effect was found on the fibers orientation by changing the coefficient of friction between fibers and the die wall, the present simulation recommended a design with a minimum frictional resistance, which is an essential factor to have a safe thermoplastic braid-trusion process.

8.2 Limitation and future research direction

We are confident that our research will serve as a base for future studies on thermoplastic braid-trusion. The findings and limitations of this thesis suggest the following opportunities for future researches:

- **Investigation of the polymer flow on the micro-geometry of braid-truded composites**

In this thesis a dry braid deformation was simulated during pultrusion and no polymer flow was considered. Despite the simulation of dry braids studied here showed reliable results for the local fiber orientation, but the effect of polymer flow on the braid's micro-geometry should be investigated in future studies. Also, since the viscosity of thermoplastic polymers varies with increasing the temperature during the pultrusion process, this polymer behavior may affect the pulling force and solids' interaction in the pultrusion die. These problems must be addressed in future works.

- **Accelerating the thermoplastic pultrusion process**

The manufacturing speed of thermoplastic pultrusion is still rather slow due to the high viscosity of thermoplastic materials. This technique requires more numerical and experimental researches to accelerate the process.

- **Effect of the braid pattern and angle on the thermoplastic braid-trusion process**

More commonly used braid patterns for composite manufacturing are the diamond (1/1), regular (2/2), and hercules (3/3), which should be studied for thermoplastic braid-trusion. The 3D braid architecture also needs to be investigated for thermoplastic pultrusion.

The fiber orientation has a significant effect on the mechanical properties of composites. The impact of braid angle on the void content, impregnation, and mechanical properties of braid-truded composites is recommended to analyze in future works.

- **Mechanical behavior of fiber-level braid model**

This thesis only addressed the geometrical aspects of the biaxial braids using the fiber-level modeling approach. We recommend researching the ability of this approach to capture the mechanical behavior of braids.

- **Investigation of the local fiber orientation on the different braid architectures**

We analyzed the local fiber orientation of the braided preform and braid-truded rod only with the regular pattern using the fiber-level model. Future studies should concentrate on investigations of the local fiber orientation of braids with different architecture.

- **Effect of inter-fibers friction and contact interactions between fibers and the die wall**

The primary investigation of the effect of friction between fibers and the pultrusion die wall on the micro-geometry of the braid-truded rod was carried out in this thesis. However, it requires more examinations on the inter-fibers friction and their influences on the pultrusion pulling force.

- **Characterization of manufacturing-induced defects during thermoplastic braid-trusion**

The prospect of being able to characterize the manufacturing-induced defects using the proposed model serves as a continuous stimulus for future research.

REFERENCES

- [1] W. Michaeli and D. Jürss, "Thermoplastic pull-braiding: Pultrusion of profiles with braided fibre lay-up and thermoplastic matrix system (PP)," *Composites Part A: Applied Science and Manufacturing*, vol. 27, no. 1, pp. 3-7, 1996/01/01 1996, doi: [http://dx.doi.org/10.1016/1359-835X\(95\)00004-L](http://dx.doi.org/10.1016/1359-835X(95)00004-L).
- [2] G. Bechtold, S. Wiedmer, and K. Friedrich, "Pultrusion of thermoplastic composites-New developments and modelling studies," *Journal of Thermoplastic Composite Materials*, vol. 15, no. 5, pp. 443-465, 2002.
- [3] M. Milwich, "Thermoplastic braid pultrusion," in *Proceedings of ICCM*, 2009, vol. 17.
- [4] L. Lebel, H. Daisuke, Y. Tanaka, and A. Nakai, "Braid-trusion of jute/polylactic acid composites," in *25th American society for composite technical conference and 14th US-Japan conference on composite materials. Dayton, Ohio, USA*, 2010.
- [5] L. L. Lebel and A. Nakai, "Design and manufacturing of an L-shaped thermoplastic composite beam by braid-trusion," *Composites Part A: Applied Science and Manufacturing*, vol. 43, no. 10, pp. 1717-1729, 2012.
- [6] A. Memon and A. Nakai, "The Processing Design of Jute Spun Yarn/PLA Braided Composite by Pultrusion Molding," *Advances in Mechanical Engineering*, vol. 5, p. 816513, 2013, doi: doi:10.1155/2013/816513.
- [7] J. Schäfer, T. Gries, R. Schuster, and C. Lammel, "Continuous production of fibre reinforced thermoplastic composites by braiding pultrusion," in *Proceedings of the 20th International Conference on Composite Materials*, 2015: ICCM Copenhagen.
- [8] M. Milwich, "Pultrusion of braids," in *Advances in Braiding Technology*: Elsevier, 2016, pp. 355-381.
- [9] B. Maron, C. Garthaus, A. Hornig, F. Lenz, M. Hübner, and M. Gude, "Forming of carbon fiber reinforced thermoplastic composite tubes-Experimental and numerical approaches," *CIRP Journal of Manufacturing Science and Technology*, vol. 18, pp. 60-64, 2017.
- [10] M. Ghaedsharaf, J.-E. Brunel, and L. Laberge Lebel, "Thermoplastic composite rod manufacturing using biaxial braid-trusion," in *Proceedings of the ECCM18-18th European Conference on Composite Materials, Athens, Greece*, 2018.
- [11] S. V. Hoa, *Principles of the manufacturing of composite materials*. DEStech Publications, Inc, 2009.
- [12] S. G. Advani and K.-T. Hsiao, *Manufacturing techniques for polymer matrix composites (PMCs)*. Elsevier, 2012.
- [13] P. Boisse, *Advances in composites manufacturing and process design*. Woodhead Publishing, 2015.
- [14] A. C. Long, *Composites forming technologies*. Elsevier, 2014.
- [15] R. Alagirusamy, R. Figueiro, V. Ogale, and N. Padaki, "Hybrid yarns and textile preforming for thermoplastic composites," *Textile Progress*, vol. 38, no. 4, pp. 1-71, 2006.

- [16] B. T. Åström and R. B. Pipes, "Modeling of a thermoplastic pultrusion process," *SAMPE Quarterly (Society of Aerospace Material and Process Engineers);(United States)*, vol. 22, no. 4, 1991.
- [17] B. T. Åström and R. B. Pipes, "A modeling approach to thermoplastic pultrusion. I: Formulation of models," *Polymer Composites*, vol. 14, no. 3, pp. 173-183, 1993.
- [18] D.-H. Kim, W. I. Lee, and K. Friedrich, "A model for a thermoplastic pultrusion process using commingled yarns," *Composites science and technology*, vol. 61, no. 8, pp. 1065-1077, 2001.
- [19] S. Rana and R. Figueiro, *Braided structures and composites: production, properties, mechanics, and technical applications*. CRC Press, 2015.
- [20] F. K. Ko, C. M. Pastore, and A. A. Head, *Atkins & Pearce handbook of industrial braiding*. Atkins & Pearce, 1990.
- [21] S. Xiao, P. Wang, D. Soulat, X. Legrand, and H. Gao, "Towards the deformability of triaxial braided composite reinforcement during manufacturing," *Composites Part B: Engineering*, vol. 169, pp. 209-220, 2019.
- [22] J. P. Carey, *Handbook of advances in braided composite materials: theory, production, testing and applications*. Woodhead Publishing, 2016.
- [23] Y. Kyosev and Schilgerius, *Topology-based modeling of textile structures and their joint assemblies*. Springer, 2019.
- [24] K. Birkefeld, M. Röder, T. von Reden, M. Bulat, and K. Drechsler, "Characterization of Biaxial and Triaxial Braids: Fiber Architecture and Mechanical Properties," *Applied Composite Materials*, vol. 19, no. 3, pp. 259-273, 2012/06/01 2012, doi: 10.1007/s10443-011-9190-2.
- [25] D. Boris, L. Xavier, and S. Damien, "The tensile behaviour of biaxial and triaxial braided fabrics," *Journal of Industrial Textiles*, vol. 47, no. 8, pp. 2184-2204, 2018, doi: 10.1177/1528083716654469.
- [26] F. T. Peirce, "5—THE GEOMETRY OF CLOTH STRUCTURE," *Journal of the Textile Institute Transactions*, vol. 28, no. 3, pp. T45-T96, 1937/03/01 1937, doi: 10.1080/19447023708658809.
- [27] D. Brunnschweiler, "Braids and Braiding," *Journal of the Textile Institute Proceedings*, vol. 44, no. 9, pp. P666-P686, 1953/09/01 1953, doi: 10.1080/19447015308687874.
- [28] A. Kemp, "An Extension of Peirce's Cloth Geometry to the Treatment of Non-circular Threads," *Journal of the Textile Institute Transactions*, vol. 49, no. 1, pp. T44-T48, 1958/01/01 1958, doi: 10.1080/19447025808660119.
- [29] C. M. Pastore, A. B. Birger, and E. Clyburn, "Geometrical modelling of textile reinforcements," 1995.
- [30] S. V. Lomov, G. Huysmans, and I. Verpoest, "Hierarchy of Textile Structures and Architecture of Fabric Geometric Models," *Textile Research Journal*, vol. 71, no. 6, pp. 534-543, 2001, doi: doi:10.1177/004051750107100611.

- [31] S. V. Lomov, R. S. Parnas, S. B. Ghosh, I. Verpoest, and A. Nakai, "Experimental and Theoretical Characterization of the Geometry of Two-Dimensional Braided Fabrics," *Textile Research Journal*, vol. 72, no. 8, pp. 706-712, 2002, doi: doi:10.1177/004051750207200810.
- [32] T. Alpyildiz, "3D geometrical modelling of tubular braids," *Textile Research Journal*, vol. 82, no. 5, pp. 443-453, 2012.
- [33] F. Robitaille, B. R. Clayton, A. C. Long, B. J. Souter, and C. D. Rudd, "Geometric modelling of industrial preforms: Woven and braided textiles," *Proceedings of the Institution of Mechanical Engineers, Part L: Journal of Materials: Design and Applications*, vol. 213, no. 2, pp. 69-83, 1999, doi: doi:10.1177/146442079921300201.
- [34] F. Robitaille, A. Long, I. Jones, and C. Rudd, "Automatically generated geometric descriptions of textile and composite unit cells," *Composites Part A: Applied Science and Manufacturing*, vol. 34, no. 4, pp. 303-312, 2003.
- [35] M. Sherburn, "Geometric and mechanical modelling of textiles," University of Nottingham, 2007.
- [36] H. Lin, L. P. Brown, and A. C. Long, "Modelling and simulating textile structures using TexGen," in *Advanced Materials Research*, 2011, vol. 331: Trans Tech Publ, pp. 44-47.
- [37] http://texgen.sourceforge.net/index.php/Main_Page. (2017).
- [38] F. Gommer, L. P. Brown, and R. Brooks, "Quantification of mesoscale variability and geometrical reconstruction of a textile," *Journal of Composite Materials*, vol. 50, no. 23, pp. 3255-3266, 2016, doi: doi:10.1177/0021998315617819.
- [39] J. Hu, *Structure and mechanics of woven fabrics*. CRC Press, 2004.
- [40] J. W. S. Hearle and W. J. Shanahan, "AN ENERGY METHOD FOR CALCULATIONS IN FABRIC MECHANICS PART I: PRINCIPLES OF THE METHOD," *The Journal of The Textile Institute*, vol. 69, no. 4, pp. 81-91, 1978/04/01 1978, doi: 10.1080/00405007808631425.
- [41] J. R. Collier, B. J. Collier, G. O'Toole, and S. Sargand, "Drape prediction by means of finite-element analysis," *Journal of the Textile Institute*, vol. 82, no. 1, pp. 96-107, 1991.
- [42] J. W. Eischen, S. Deng, and T. G. Clapp, "Finite-element modeling and control of flexible fabric parts," *IEEE Computer Graphics and Applications*, vol. 16, no. 5, pp. 71-80, 1996.
- [43] L. Dong, C. Lekakou, and M. Bader, "Processing of composites: simulations of the draping of fabrics with updated material behaviour law," *Journal of composite materials*, vol. 35, no. 2, pp. 138-163, 2001.
- [44] P. De Luca, P. Lefébure, and A. Pickett, "Numerical and experimental investigation of some press forming parameters of two fibre reinforced thermoplastics: APC2-AS4 and PEI-CETEX," *Composites Part A: Applied Science and Manufacturing*, vol. 29, no. 1-2, pp. 101-110, 1998.
- [45] E. De Luycker, F. Morestin, P. Boisse, and D. Marsal, "Simulation of 3D interlock composite preforming," *Composite Structures*, vol. 88, no. 4, pp. 615-623, 2009.

- [46] P. Harrison, W.-R. Yu, and A. C. Long, "Rate dependent modelling of the forming behaviour of viscous textile composites," *Composites Part A: Applied science and manufacturing*, vol. 42, no. 11, pp. 1719-1726, 2011.
- [47] T. Gereke, O. Döbrich, M. Hübner, and C. Cherif, "Experimental and computational composite textile reinforcement forming: A review," *Composites Part A: Applied Science and Manufacturing*, vol. 46, pp. 1-10, 2013.
- [48] J. Pazmino, S. Mathieu, V. Carvelli, P. Boisse, and S. V. Lomov, "Numerical modelling of forming of a non-crimp 3D orthogonal weave E-glass composite reinforcement," *Composites Part A: Applied Science and Manufacturing*, vol. 72, pp. 207-218, 2015.
- [49] M. Hübner, J.-E. Rocher, S. Allaoui, G. Hivet, T. Gereke, and C. Cherif, "Simulation-based investigations on the drape behavior of 3D woven fabrics made of commingled yarns," *International Journal of Material Forming*, vol. 9, no. 5, pp. 591-599, 2016.
- [50] P. Boisse, N. Hamila, and A. Madeo, "The difficulties in modeling the mechanical behavior of textile composite reinforcements with standard continuum mechanics of Cauchy. Some possible remedies," *International Journal of Solids and Structures*, vol. 154, pp. 55-65, 2018/12/01/ 2018, doi: <https://doi.org/10.1016/j.ijsolstr.2016.12.019>.
- [51] S. Gatouillat, A. Bareggi, E. Vidal-Sallé, and P. Boisse, "Meso modelling for composite preform shaping – Simulation of the loss of cohesion of the woven fibre network," *Composites Part A: Applied Science and Manufacturing*, vol. 54, pp. 135-144, 2013/11/01/ 2013, doi: <https://doi.org/10.1016/j.compositesa.2013.07.010>.
- [52] G. Hivet and P. Boisse, "Consistent 3D geometrical model of fabric elementary cell. Application to a meshing preprocessor for 3D finite element analysis," *Finite Elements in Analysis and Design*, vol. 42, no. 1, pp. 25-49, 10// 2005, doi: <http://dx.doi.org/10.1016/j.finel.2005.05.001>.
- [53] G. Hivet and P. Boisse, "Consistent mesoscopic mechanical behaviour model for woven composite reinforcements in biaxial tension," *Composites Part B: Engineering*, vol. 39, no. 2, pp. 345-361, 3// 2008, doi: <http://dx.doi.org/10.1016/j.compositesb.2007.01.011>.
- [54] G. Hivet, A. Wendling, E. Vidal-Salle, B. Laine, and P. Boisse, "Modeling strategies for fabrics unit cell geometry application to permeability simulations," *International Journal of Material Forming*, journal article vol. 3, no. 1, pp. 727-730, 2010, doi: 10.1007/s12289-010-0873-2.
- [55] J. L. Kuhn and P. G. Charalambides, "Modeling of Plain Weave Fabric Composite Geometry," *Journal of Composite Materials*, vol. 33, no. 3, pp. 188-220, 1999, doi: doi:10.1177/002199839903300301.
- [56] S. V. Lomov *et al.*, "Meso-FE modelling of textile composites: Road map, data flow and algorithms," *Composites Science and Technology*, vol. 67, no. 9, pp. 1870-1891, 2007/07/01/ 2007, doi: <https://doi.org/10.1016/j.compscitech.2006.10.017>.
- [57] A. Charmetant, E. Vidal-Sallé, and P. Boisse, "Hyperelastic modelling for mesoscopic analyses of composite reinforcements," *Composites Science and Technology*, vol. 71, no. 14, pp. 1623-1631, 2011.

- [58] A. Charmetant, J. G. Orliac, E. Vidal-Sallé, and P. Boisse, "Hyperelastic model for large deformation analyses of 3D interlock composite preforms," *Composites Science and Technology*, vol. 72, no. 12, pp. 1352-1360, 2012/07/23/ 2012, doi: <https://doi.org/10.1016/j.compscitech.2012.05.006>.
- [59] T. Wehrkamp-Richter, N. V. De Carvalho, and S. T. Pinho, "A meso-scale simulation framework for predicting the mechanical response of triaxial braided composites," *Composites Part A: Applied Science and Manufacturing*, vol. 107, pp. 489-506, 2018.
- [60] A. Iwata, T. Inoue, N. Naouar, P. Boisse, and S. V. Lomov, "Coupled meso-macro simulation of woven fabric local deformation during draping," *Composites Part A: Applied Science and Manufacturing*, vol. 118, pp. 267-280, 2019/03/01/ 2019, doi: <https://doi.org/10.1016/j.compositesa.2019.01.004>.
- [61] L. Huang, Y. Wang, Y. Miao, D. Swenson, Y. Ma, and C.-F. Yen, "Dynamic relaxation approach with periodic boundary conditions in determining the 3-D woven textile micro-geometry," *Composite Structures*, vol. 106, pp. 417-425, 2013.
- [62] Y. Miao, E. Zhou, Y. Wang, and B. A. Cheeseman, "Mechanics of textile composites: Micro-geometry," *Composites Science and Technology*, vol. 68, no. 7-8, pp. 1671-1678, 2008, doi: 10.1016/j.compscitech.2008.02.018.
- [63] Y. Wang and X. Sun, "Digital-element simulation of textile processes," *Composite Science and Technology*, vol. 61, pp. 311-319, 2001.
- [64] G. Zhou, X. Sun, and Y. Wang, "Multi-chain digital element analysis in textile mechanics," *Composites science and Technology*, vol. 64, no. 2, pp. 239-244, 2004.
- [65] D. Durville, "Simulation of the mechanical behaviour of woven fabrics at the scale of fibers," *International Journal of Material Forming*, vol. 3, no. S2, pp. 1241-1251, 2010, doi: 10.1007/s12289-009-0674-7.
- [66] D. Durville, "Contact-friction modeling within elastic beam assemblies: an application to knot tightening," *Computational Mechanics*, vol. 49, no. 6, pp. 687-707, 2012.
- [67] P. Davies, D. Durville, and T. D. Vu, "The influence of torsion on braided rope performance, modelling and tests," *Applied Ocean Research*, vol. 59, pp. 417-423, 2016, doi: 10.1016/j.apor.2016.07.003.
- [68] Y. Mahadik and S. R. Hallett, "Finite element modelling of tow geometry in 3D woven fabrics," *Composites Part A: Applied Science and Manufacturing*, vol. 41, no. 9, pp. 1192-1200, 2010, doi: 10.1016/j.compositesa.2010.05.001.
- [69] S. D. Green, A. C. Long, B. S. F. El Said, and S. R. Hallett, "Numerical modelling of 3D woven preform deformations," *Composite Structures*, vol. 108, pp. 747-756, 2014, doi: 10.1016/j.compstruct.2013.10.015.
- [70] R. Samadi and F. Robitaille, "Particle-based modeling of the compaction of fiber yarns and woven textiles," *Textile Research Journal*, vol. 84, no. 11, pp. 1159-1173, 2014.
- [71] S. Allaoui, G. Hivet, D. Soulat, A. Wendling, P. Ouagne, and S. Chatel, "Experimental preforming of highly double curved shapes with a case corner using an interlock

- reinforcement," *International Journal of Material Forming*, vol. 7, no. 2, pp. 155-165, 2014.
- [72] S. V. Lomov *et al.*, "Textile composites: modelling strategies," *Composites Part A: applied science and manufacturing*, vol. 32, no. 10, pp. 1379-1394, 2001.
- [73] I. Verpoest and S. V. Lomov, "Virtual textile composites software WiseTex: Integration with micro-mechanical, permeability and structural analysis," *Composites Science and Technology*, vol. 65, no. 15, pp. 2563-2574, 2005.
- [74] <http://www.mtm.kuleuven.be/Onderzoek/Composites/software/wisetex>. (2016).
- [75] *Digital Element Approach Fabric and Composite Analyzer (DFCA)*. (2021). [Online]. Available: <http://www.fabricmechanics.com>
- [76] D. Durville, "Numerical simulation of entangled materials mechanical properties," *Journal of Materials Science*, vol. 40, no. 22, pp. 5941-5948, 2005, doi: 10.1007/s10853-005-5061-2.
- [77] D. Durville, "Finite element simulation of textile materials at mesoscopic scale," in *Finite element modelling of textiles and textile composites*, 2007, p. CDROM.
- [78] H. Bajas, D. Durville, D. Ciazynski, and a. A. Devred, "Numerical Simulation of the Mechanical Behavior of ITER Cable-In-Conduit Conductors," *IEEE TRANSACTIONS ON APPLIED SUPERCONDUCTIVITY*, vol. 20, no. 3, 2010.
- [79] C. P. Laurent, D. Durville, D. Mainard, J. F. Ganghoffer, and R. Rahouadj, "A multilayer braided scaffold for Anterior Cruciate Ligament: mechanical modeling at the fiber scale," *Journal of the mechanical behavior of biomedical materials*, vol. 12, pp. 184-96, Aug 2012, doi: 10.1016/j.jmbbm.2012.03.005.
- [80] C. P. Laurent *et al.*, "Mechanical behaviour of a fibrous scaffold for ligament tissue engineering: finite elements analysis vs. X-ray tomography imaging," *Journal of the mechanical behavior of biomedical materials*, vol. 40, pp. 222-33, Dec 2014, doi: 10.1016/j.jmbbm.2014.09.003.
- [81] T. Vu, D. Durville, and P. Davies, "Finite element simulation of the mechanical behavior of synthetic braided ropes and validation on a tensile test," *International Journal of Solids and Structures*, vol. 58, pp. 106-116, 2015.
- [82] N. Metropolis, A. W. Rosenbluth, M. N. Rosenbluth, A. H. Teller, and E. Teller, "Equation of state calculations by fast computing machines," *The journal of chemical physics*, vol. 21, no. 6, pp. 1087-1092, 1953.
- [83] Y. Crama and P. L. Hammer, *Boolean functions: Theory, algorithms, and applications*. Cambridge University Press, 2011.
- [84] M. Ghaedsharaf, J.-E. Brunel, and L. Laberge Lebel, "Fiber-level numerical simulation of biaxial braids for mesoscopic morphology prediction validated by X-ray computed tomography scan," *Composites Part B: Engineering*, vol. 218, p. 108938, 2021, doi: <https://doi.org/10.1016/j.compositesb.2021.108938>.

- [85] M. Ghaedsharaf, J.-E. Brunel, and L. Laberge Lebel, "Multiscale numerical simulation of the forming process of biaxial braids during thermoplastic braid-trusion: Predicting 3D and internal geometry and fiber orientation distribution," *Composites Part A: Applied Science and Manufacturing*, vol. 150, p. 106637, 2021, doi: <https://doi.org/10.1016/j.compositesa.2021.106637>.
- [86] *Concordia Fibers datasheets*, 2018. [Online]. Available: <http://www.concordiafibers.com/thermo-plastic-options.html>.
- [87] J. S. Yu, M. Lim, and D. M. Kalyon, "Development of density distributions in injection molded amorphous engineering plastics. Part I," *Polymer Engineering & Science*, vol. 31, no. 3, pp. 145-152, 1991.
- [88] F. Lapointe and L. Laberge Lebel, "Fiber damage and impregnation during multi-die vacuum assisted pultrusion of carbon/PEEK hybrid yarns," *Polymer Composites*, vol. 40, no. S2, pp. E1015-E1028, 2019.
- [89] D. S. Ivanov, F. Baudry, B. Van Den Broucke, S. V. Lomov, H. Xie, and I. Verpoest, "Failure analysis of triaxial braided composite," *Composites Science and Technology*, vol. 69, no. 9, pp. 1372-1380, 2009/07/01/ 2009, doi: <https://doi.org/10.1016/j.compscitech.2008.09.013>.
- [90] G. W. Melenka and J. P. Carey, "Experimental analysis of diamond and regular tubular braided composites using three-dimensional digital image correlation," *Journal of Composite Materials*, vol. 51, no. 28, pp. 3887-3907, 2017.
- [91] W.-J. Na, H. C. Ahn, S.-Y. Jeon, J. S. Lee, H.-M. Kang, and W.-R. Yu, "Prediction of the braid pattern on arbitrary-shaped mandrels using the minimum path condition," *Composites Science and Technology*, vol. 91, pp. 30-37, 2014/01/31/ 2014, doi: <https://doi.org/10.1016/j.compscitech.2013.11.012>.
- [92] Y. Kyosev, *Braiding technology for textiles: Principles, design and processes*. Elsevier, 2014.
- [93] S. Song, A. M. Waas, K. W. Shahwan, X. Xiao, and O. Faruque, "Braided textile composites under compressive loads: modeling the response, strength and degradation," *Composites Science and Technology*, vol. 67, no. 15-16, pp. 3059-3070, 2007.
- [94] P. Badel, E. Vidal-Sallé, E. Maire, and P. Boisse, "Simulation and tomography analysis of textile composite reinforcement deformation at the mesoscopic scale," *Composites Science and Technology*, vol. 68, no. 12, pp. 2433-2440, 2008.
- [95] Z. Zhao, P. Liu, C. Chen, C. Zhang, and Y. Li, "Modeling the transverse tensile and compressive failure behavior of triaxially braided composites," *Composites Science and Technology*, vol. 172, pp. 96-107, 2019.
- [96] L. Daelemans *et al.*, "Finite element simulation of the woven geometry and mechanical behaviour of a 3D woven dry fabric under tensile and shear loading using the digital element method," *Composites Science and Technology*, vol. 137, pp. 177-187, 2016.

- [97] M. Ghaedsharaf, J.-E. Brunel, and L. Laberge Lebel, "Fiber-level bi-axial braid simulation for braid-trusion," in *10th Canadian-International Conference on Composite Materials*, Ottawa, Canada, 2017.
- [98] Abaqus Analysis User's Guide
- [99] J. Van Ravenhorst and R. Akkerman, "A yarn interaction model for circular braiding," *Composites Part A: Applied Science and Manufacturing*, vol. 81, pp. 254-263, 2016.
- [100] "Tansome carbon fiber catalog," 2020. [Online]. Available: www.hyosungadvancedmaterials.com.
- [101] S. Li, L. Xu, Z. Ding, L. J. Lee, and H. Engelen, "Experimental and theoretical analysis of pulling force in pultrusion and resin injection pultrusion (RIP)—part I: experimental," *Journal of composite materials*, vol. 37, no. 2, pp. 163-189, 2003.
- [102] I. Baran, C. C. Tutum, and J. H. Hattel, "The effect of thermal contact resistance on the thermosetting pultrusion process," *Composites Part B: Engineering*, vol. 45, no. 1, pp. 995-1000, 2013/02/01/ 2013, doi: <https://doi.org/10.1016/j.compositesb.2012.09.049>.
- [103] P. Simacek and S. Advani, "Simulating tape resin infiltration during thermoset pultrusion process," *Composites Part A: Applied Science and Manufacturing*, vol. 72, pp. 115-126, 2015.
- [104] M. Sandberg, O. Yuksel, I. Baran, J. H. Hattel, and J. Spangenberg, "Numerical and experimental analysis of resin-flow, heat-transfer, and cure in a resin-injection pultrusion process," *Composites Part A: Applied Science and Manufacturing*, vol. 143, p. 106231, 2021.
- [105] A. H. Miller, N. Dodds, J. Hale, and A. Gibson, "High speed pultrusion of thermoplastic matrix composites," *Composites Part A: Applied Science and Manufacturing*, vol. 29, no. 7, pp. 773-782, 1998.
- [106] J. Nunes, J. Silva, and P. Novo, "Processing thermoplastic matrix towpregs by pultrusion," *Advances in polymer technology*, vol. 32, no. S1, pp. E306-E312, 2013.
- [107] P. Novo, J. F. Silva, J. Nunes, and A. Marques, "Pultrusion of fibre reinforced thermoplastic pre-impregnated materials," *Composites Part B: Engineering*, vol. 89, pp. 328-339, 2016.
- [108] M. Ueda, N. Ui, and A. Ohtani, "Lightweight and anti-corrosive fiber reinforced thermoplastic rivet," *Composite Structures*, vol. 188, pp. 356-362, 2018.
- [109] H. Hedayati Velis, M. Golzar, and O. Yousefzade, "Composites based on HDPE, jute fiber, wood, and thermoplastic starch in tubular pultrusion die: The correlation between mechanical performance and microstructure," *Advances in Polymer Technology*, vol. 37, no. 8, pp. 3483-3491, 2018.
- [110] M. Volk, S. Arreguin, P. Ermanni, J. Wong, C. Bär, and F. Schmuck, "Pultruded thermoplastic composites for high voltage insulator applications," *IEEE Transactions on Dielectrics and Electrical Insulation*, vol. 27, no. 4, pp. 1280-1287, 2020.
- [111] K. Minchenkov, A. Vedernikov, A. Safonov, and I. Akhatov, "Thermoplastic pultrusion: a review," *Polymers*, vol. 13, no. 2, p. 180, 2021.

- [112] Y. Kyosev, *Advances in braiding technology: Specialized techniques and applications*. Woodhead Publishing, 2016.
- [113] M. Eichenhofer, J. C. Wong, and P. Ermanni, "Exploiting cyclic softening in continuous lattice fabrication for the additive manufacturing of high performance fibre-reinforced thermoplastic composite materials," *Composites Science and Technology*, vol. 164, pp. 248-259, 2018.
- [114] N. Alsinani, M. Ghaedsharaf, and L. Laberge Lebel, "Effect of cooling temperature on deconsolidation and pulling forces in a thermoplastic pultrusion process," *Composites Part B: Engineering*, vol. 219, p. 108889, 2021, doi: <https://doi.org/10.1016/j.compositesb.2021.108889>.
- [115] O. Döbrich, T. Gereke, and C. Cherif, "Modeling the mechanical properties of textile-reinforced composites with a near micro-scale approach," *Composite Structures*, vol. 135, pp. 1-7, 2016.
- [116] C. Liu, J. Xie, Y. Sun, and L. Chen, "Micro-scale modeling of textile composites based on the virtual fiber embedded models," *Composite Structures*, vol. 230, p. 111552, 2019/12/15/ 2019, doi: <https://doi.org/10.1016/j.compstruct.2019.111552>.
- [117] C. Barry, F. Panerai, K. Bergeron, S. Stapleton, and J. Sherwood, "Mesomechanical Modeling of Braided Cords," *Procedia Manufacturing*, vol. 47, pp. 162-168, 2020.
- [118] L. Wu, F. Zhao, J. Xie, X. Wu, Q. Jiang, and J.-H. Lin, "The deformation behaviors and mechanism of weft knitted fabric based on micro-scale virtual fiber model," *International Journal of Mechanical Sciences*, vol. 187, p. 105929, 2020.
- [119] L. Daelemans *et al.*, "Kinematic and mechanical response of dry woven fabrics in through-thickness compression: Virtual fiber modeling with mesh overlay technique and experimental validation," *Composites Science and Technology*, vol. 207, p. 108706, 2021.

APPENDIX A SMOOTH STEP AMPLITUDE CURVE

Figure A.1 shows the smooth amplitude curve assigned to the applied load.

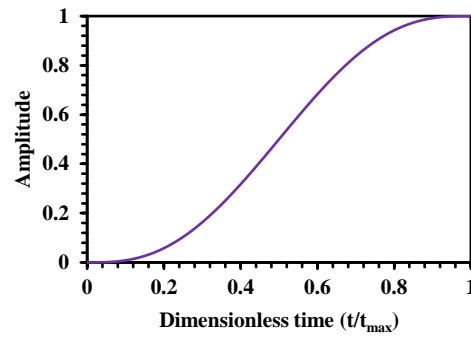


Figure A.1 Smooth step amplitude curve.

APPENDIX B MICRO-CT SCANNING PROCEDURE OF DRY CARBON FIBER BRAIDS

Figure B.1a,b presents the braided diamond and regular carbon fiber. A specimen with a length of 250 mm was cut from both braided pattern. Figure B.1c represents a fixture mechanism designed to hold the braid specimen in the CT scanning machine. It consisted of an acrylic tube with a length of 250 mm and an inner diameter of 8 mm and an outer diameter of 10 mm, two plastic caps, two threaded rods with a length of 25 mm and a thread size of M2×0.4 mm, and two hex nuts. The braid specimen was centered inside the acrylic tube while the clamped ends of the specimen were embedded in threaded rods using epoxy. Screwing the nuts allowed for the application of a small axial tension on the braid specimen to keep it straight during scanning. Only the unimpregnated center region of the braided specimens with a length of 15 mm was selected as an acquisition region. The reconstructed 3D view of a 9.19 mm long diamond braided carbon fiber contained 1,836 slices and the reconstructed 3D view of the regular pattern with a length of 12.99 mm had 2,000 slices normal to the axis of the braid sample.

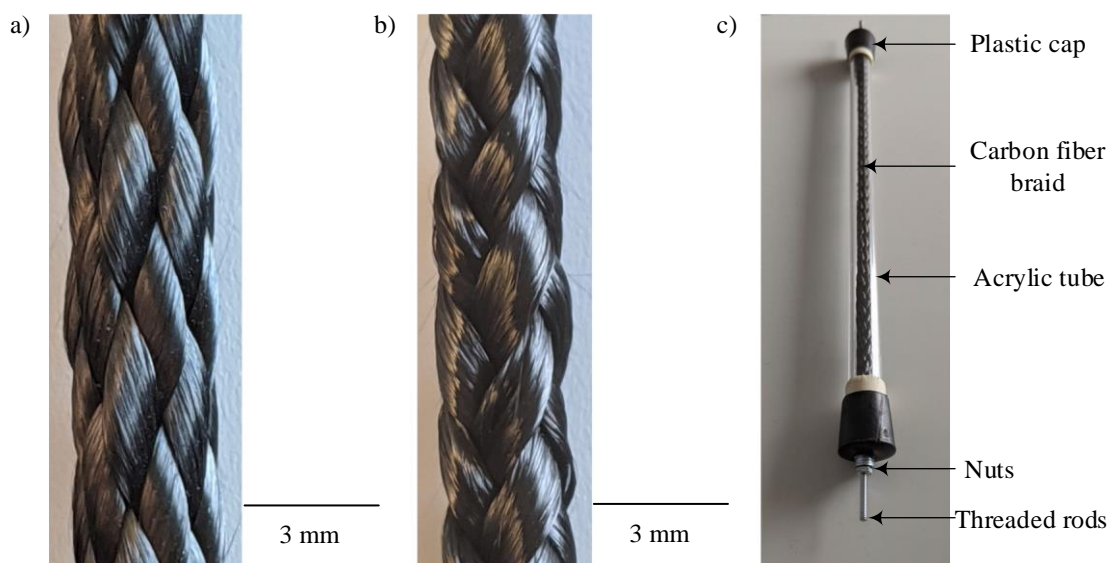


Figure B.1 (a) Diamond braided carbon fiber with 12 yarns. (b) Regular braided carbon fiber with 8 yarns. (c) Fixture mechanism for holding the braid during CT scanning.

APPENDIX C THE LIST OF PUBLICATIONS AND PRESENTATIONS

EXTRACTED FROM THE THESIS

1. M. Ghaedsharaf, J.-E. Brunel, L. Laberge Lebel, "Thermoplastic composite rod manufacturing using biaxial braid-trusion," *Proceedings of ECCM18 - the 18th European conference on composite materials*, Athens, Greece, June 2018.
2. M. Ghaedsharaf, J.-E. Brunel, L. Laberge Lebel, "Fiber-level numerical simulation of biaxial braids for mesoscopic morphology prediction validated by X-ray computed tomography scan," *Composites Part B: Engineering*, vol. 218, 108938, 2021.
3. M. Ghaedsharaf, J.-E. Brunel, L. Laberge Lebel, "Multiscale numerical simulation of the forming process of biaxial braids during thermoplastic braid-trusion: Predicting 3D and internal geometry and fiber orientation distribution," *Composites Part A: Applied Science and Manufacturing*, vol. 150, 106637, 2021.
4. M. Ghaedsharaf, J.-E. Brunel, L. Laberge Lebel, "Fiber-level bi-axial braid simulation for braid-trusion," *Proceedings of CANCOM2017 - the 10th Canadian international conference on composite materials*, Ottawa, Canada, July 2017.
5. M. Ghaedsharaf, L. Laberge Lebel, "The effect of the braid pattern on the pulling force of thermoplastic braid-trusion," *Proceedings of CASI19 - the Canadian Aeronautics and Space Institute's AERO 2019*, Laval, Canada, May 2019.
6. M. Ghaedsharaf, L. Laberge Lebel, "The effect of braid angle on the void content and fiber misorientation of thermoplastic diamond and regular braided rod manufacturing using braid-trusion," *Proceedings of ACM4 - the 4th International Symposium on Automated Composites Manufacturing*, Montreal, Canada, April 2019.